

ISSN: 2220-9506 (Print)
ISSN: 2414-0473 (Online)

ПРИБОРЫ И МЕТОДЫ ИЗМЕРЕНИЙ

DEVICES AND METHODS OF MEASUREMENTS

Том 12

№ 3

Vol. 12

100 ЛЕТ



ХРАНИМ ТРАДИЦИИ, ЖИВЕМ НАСТОЯЩИМ, СОЗДАЕМ БУДУЩЕЕ!

2021

ПРИБОРЫ И МЕТОДЫ ИЗМЕРЕНИЙ

Научно-технический журнал

Основан в 2010 г.

Учредитель

Белорусский национальный технический университет

Выходит 4 раза в год

Журнал включен в базы данных:
Web of Science Core Collection (ESCI),
EBSCO, DOAJ, WorldCat, OpenAIRE, Google Scholar, РИНЦ,
ЭБС «Лань», НЭБ «КиберЛенинка», Соционет

Том 12

№ 3

2021

ГЛАВНЫЙ РЕДАКТОР

Гусев О.К., д.т.н., профессор, проректор Белорусского национального технического университета
(г. Минск, Беларусь)

ЗАМЕСТИТЕЛЬ ГЛАВНОГО РЕДАКТОРА

Маляревич А.М., член-корреспондент НАН Беларуси, д.ф.-м.н., профессор, проректор Белорусского национального технического университета (г. Минск, Беларусь)

РЕДАКЦИОННАЯ КОЛЛЕГИЯ

Алексеев В.А., д.т.н., профессор, ученый секретарь Ижевского государственного технического университета имени М.Т. Калашникова (г. Ижевск, Россия)

Анищик В.М., д.ф.-м.н., профессор, профессор кафедры физики твёрдого тела Белорусского государственного университета (г. Минск, Беларусь)

Бубулис А., д.т.н., профессор, главный научный сотрудник Научного центра мехатроники Каунасского технологического университета (г. Каунас, Литва)

Вайн А.А., д.т.н., профессор Тартуского университета (г. Тарту, Эстония)

Виба Я., д.т.н., профессор, директор Института механики Рижского технического университета (г. Рига, Латвия)

Гуттен М., д.т.н., заведующий кафедрой метрологии и прикладной электротехники Жилинского университета (г. Жилина, Словакия)

Дмитриев С.М., д.т.н., профессор, ректор Нижегородского государственного технического университета имени Р.Е. Алексеева (г. Нижний Новгород, Россия)

Дэнилак С., профессор Производственно-исследовательского центра Технологического института штата Джорджия (г. Атланта, США)

Жарин А.Л., д.т.н., профессор, профессор кафедры «Информационно-измерительная техника и технологии» Белорусского национального технического университета (г. Минск, Беларусь)

Жуковский П., д.т.н., профессор, заведующий кафедрой электрических аппаратов и техники высоких напряжений Люблинского технического университета (г. Люблин, Польша)

Колтунович Т.Н., д.т.н., профессор, Люблинский технический университет (г. Люблин, Польша)

Комаров Ф.Ф., член-корреспондент НАН Беларуси, д.ф.-м.н., профессор, заведующий лабораторией элионики Института прикладных физических проблем имени А.Н. Севченко Белорусского государственного университета (г. Минск, Беларусь)

- Кулешов Н.В.**, д.ф.-м.н., профессор, заведующий кафедрой «Лазерная техника и технология» Белорусского национального технического университета (г. Минск, Беларусь)
- Кучинский П.В.**, д.ф.-м.н., доцент, директор Института прикладных физических проблем имени А.Н. Севченко Белорусского государственного университета (г. Минск, Беларусь)
- Кэмп А.**, профессор Института фотоники Страсклайдского университета (г. Глазго, Великобритания)
- Матеос Х.**, к.ф.-м.н., доцент, университет Ровира и Вирхилий (г. Таррагона, Испания)
- Пилипенко В.А.**, член-корреспондент НАН Беларуси, д.т.н., профессор, заместитель директора ГЦ «Белмикрoанализ» ОАО «ИНТЕГРАЛ» – управляющая компания холдинга «ИНТЕГРАЛ» (г. Минск, Беларусь)
- Плескачевский Ю.М.**, член-корреспондент НАН Беларуси, д.т.н., профессор (г. Минск, Беларусь)
- Погребняк А.Д.**, д.ф.-м.н., профессор, заведующий кафедрой нанoeлектроники Сумского государственного университета (г. Сумы, Украина)
- Распопов В.Я.**, д.т.н., профессор, заведующий кафедрой «Приборы управления» Тульского государственного университета (г. Тула, Россия)
- Тимчик Г.С.**, д.т.н., профессор, декан приборостроительного факультета, Национальный технический университет Украины «Киевский политехнический институт имени Игоря Сикорского» (г. Киев, Украина)
- Це Ли**, заместитель директора Северо-Восточного НИИ техники датчиков (г. Харбин, КНР)
- Чижик С.А.**, академик НАН Беларуси, д.т.н., профессор, Первый заместитель Председателя Президиума НАН Беларуси, заведующий кафедрой «Микро- и нанотехника» Белорусского национального технического университета (г. Минск, Беларусь)
- Шкадаревич А.П.**, академик НАН Беларуси, д.ф.-м.н., профессор, директор НТЦ «ЛЭМТ» Белорусского оптико-механического объединения (г. Минск, Беларусь)
- Юмашев К.В.**, д.ф.-м.н., профессор, заведующий кафедрой «Экспериментальная и теоретическая физика» Белорусского национального технического университета (г. Минск, Беларусь)

**Издание зарегистрировано в Министерстве информации Республики Беларусь 25 июня 2010 г.
Регистрационный номер 1372**

В соответствии с решением ВАК от 8 июля 2011 г. №13/1 журнал включен в Перечень научных изданий для опубликования результатов диссертационных исследований; научное направление: «Средства и методы измерений, контроля, диагностики и оценки качества объектов и процессов» (технические и физико-математические науки)

ISSN 2220-9506

Подписка осуществляется через почтовые отделения связи по «Каталогу газет и журналов Республики Беларусь».

Подписные индексы – 74835; 748352.

Ответственный секретарь редакции: Шахлевич Л.Н.

Редактор: Чабарова О.Л.

Набор и верстка выполнены в редакции журнала «Приборы и методы измерений».

Подписано в печать 08.09.2021. Формат бумаги 60×84 1/8. Бумага мелованная.

Гарнитура Times New Roman. Печать цифровая. Усл. печ. л. 9,65. Уч.-изд. л. 3,77. Тираж 100 экз.

Дата выхода в свет 15.10.2021. Заказ № 589.

Отпечатано в Белорусском национальном техническом университете. ЛП № 02330/74 от 03.03.2014. Пр. Независимости, 65, 220013, г. Минск

АДРЕС РЕДАКЦИИ:

Белорусский национальный технический университет
пр-т Независимости, 65, 220013, г. Минск, Республика Беларусь,
тел.: +375 (17) 293 96 67, факс: +375 (17) 292 67 94
e-mail: pimi@bntu.by
<http://pimi.bntu.by>

DEVICES AND METHODS OF MEASUREMENTS

Scientific and Engineering Journal

Founded in 2010

Founder
Belarusian National Technical University

Issued four times a year

The Journal is included in the following databases:
Web of Science Core Collection (ESCI),
EBSCO, DOAJ, WorldCat, OpenAIRE, Google Scholar,
RISC, Lan, CyberLeninka, Socionet

Volume 12

№ 3

2021

EDITOR-IN-CHIEF

Oleg K. Gusev, *Doctor of Science (Engineering), Professor, Vice-Rector of Belarusian National Technical University (Minsk, Belarus)*

DEPUTY EDITOR-IN-CHIEF

Aliaksandr M. Malyarevich, *Corresponding Member of the National Academy of Sciences of Belarus, Doctor of Science (Physics and Mathematics), Professor, Vice-Rector of Belarusian National Technical University (Minsk, Belarus)*

EDITORIAL BOARD

Vladimir A. Alekseev, *Doctor of Science (Engineering), Professor, Scientific Secretary of M.T. Kalashnikov Izhevsk State Technical University (Izhevsk, Russia)*

Victor M. Anishchik, *Doctor of Science (Physics and Mathematics), Professor, Department of Solid State Physics, Belarusian State University (Minsk, Belarus)*

Algimantas Bubulis, *Doctor of Science (Engineering), Professor, Kaunas University of Technology (Kaunas, Lithuania)*

Arvid A. Vain, *Doctor of Science (Engineering), Professor, University of Tartu (Tartu, Estonia)*

Janis Viba, *Doctor of Science (Engineering), Professor, Director of Institute of Mechanics, Riga Technical University (Riga, Latvia)*

Miroslav Gutten, *Doctor of Science (Engineering), Head of Department of Metrology and Applied Electrical Engineering, University of Žilina (Žilina, Slovakia)*

Sergei M. Dmitriev, *Doctor of Science (Engineering), Professor, Rector of R.E. Alekseev Nizhny Novgorod State Technical University (Nizhny Novgorod, Russia)*

Steven Danyluk, *PhD, Professor, Production and Research Center, Georgia Institute of Technology (Atlanta, USA)*

Anatoly L. Zharin, *Doctor of Science (Engineering), Professor, Information and Measuring Technologies Department, Belarusian National Technical University (Minsk, Belarus)*

Pawel Żukowski, *Doctor of Science (Engineering), Professor, Head of Department of Electrical Devices and High Voltages Technology, Lublin University of Technology (Lublin, Poland)*

Tomasz N. Koltunowicz, *Doctor of Science (Engineering), Professor, Lublin University of Technology (Lublin, Poland)*

Fadey F. Komarov, *Corresponding Member of the National Academy of Sciences of Belarus, Doctor of Science (Physics and Mathematics), Professor, Head of the Elionics Laboratory, A.N. Sevchenko Institute of Applied Physical Problems, Belarusian State University (Minsk, Belarus)*

Nikolay V. Kuleshov, Doctor of Science (Physics and Mathematics), Professor, Head of Laser Equipment and Technology Department, Belarusian National Technical University (Minsk, Belarus)

Petr V. Kuchynski, Doctor of Science (Physics and Mathematics), Director of A.N. Sevchenko Institute of Applied Physical Problems, Belarusian State University (Minsk, Belarus)

Alan Kemp, PhD, Professor, Institute of Photonics, University of Strathclyde (Glasgow, United Kingdom)

Xavier Mateos, PhD, Associate Professor, Rovira i Virgili University (Tarragona, Spain)

Vladimir A. Pilipenko, Corresponding Member of the National Academy of Sciences of Belarus, Doctor of Science (Engineering), Professor, Deputy Director of the State Center «Belmicroanalysis» of JSC «INTEGRAL» – «INTEGRAL» Holding Managing Company (Minsk, Belarus)

Yuriy M. Pleskachevsky, Corresponding Member of the National Academy of Sciences of Belarus, Doctor of Science (Engineering), Professor (Minsk, Belarus)

Alexander D. Pogrebnyak, Doctor of Science (Physics and Mathematics), Professor, Head of Department of Nanoelectronic, Sumy State University (Sumy, Ukraine)

Vladimir Ya. Raspopov, Doctor of Science (Engineering), Professor, Head of Control Devices Department, Tula State University (Tula, Russia)

Gryhoriy S. Tymchyk, Doctor of Science (Engineering), Professor, Dean of the Faculty of Instrumentation Engineering, National Technical University of Ukraine «Igor Sikorsky Kyiv Polytechnic Institute» (Kyiv, Ukraine)

Tse Li, Deputy Director of Northeast Scientific Research Institute of Sensor Technology (Harbin, China)

Sergei A. Chizhik, Academician of National Academy of Sciences of Belarus, Professor, Doctor of Science (Engineering), the First Vice Chairman of the Presidium of the National Academy of Sciences of Belarus, Head of Micro- and Nanotechnics Department, Belarusian National Technical University (Minsk, Belarus)

Alexey P. Shkadarevich, Academician of the National Academy of Sciences of Belarus, Doctor of Science (Physics and Mathematics), Professor, Director of the Scientific and Technical Center «LEMT» of the BelOMO (Minsk, Belarus)

Konstantin V. Yumashev, Doctor of Science (Physics and Mathematics), Professor, Head of Experimental and Theoretical Physics Department, Belarusian National Technical University (Minsk, Belarus)

ADDRESS:

Belarusian National Technical University
Nezavisimosti Ave., 65, Minsk 220013, Belarus
Tel.: +375 (17) 293 96 67, fax: +375 (17) 292 67 94
e-mail: pimi@bntu.by
<http://pimi.bntu.by>

СОДЕРЖАНИЕ

Средства измерений

- В.А. Алексеев, В.Г. Костин, А.В. Усольцева, В.П. Усольцев, С.И. Юран*
Расширение функциональных возможностей фотоабляции эксимерным лазером в офтальмологии (in English)..... 175
- И.А. Коновалов, А.А. Чесноков, А.А. Баринов, С.М. Дмитриев, А.Е. Хробостов, М.А. Макаров*
Применение электроимпедансного метода измерений при исследовании пузырьковых режимов течения двухкомпонентного потока (in English)..... 183
- В.Л. Соломахо, А.А. Багдюн*
Определение погрешности передачи размера единицы длины при измерении диаметра наночастиц с помощью анализатора дифференциальной электрической подвижности частиц (in English)..... 194

Методы измерений, контроля, диагностики

- Н.А. Поклонский, И.И. Анисеев, С.А. Вырко*
Низкочастотный адмиттанс конденсатора с рабочим веществом «изолятор–частично разупорядоченный полупроводник–изолятор» (in English)..... 202
- А.Р. Баев, А.И. Митьковец, М.В. Асадчая, А.Л. Майоров*
Импульсно-лазерное возбуждение и прохождение ультразвуковых волн через наномангнитную жидкость (in English)..... 211
- В.Н. Якимов*
Цифровой спектральный анализ методом усреднённых модифицированных периодограмм с применением бинарно-знакового стохастического квантования сигналов (in English)..... 220
- А.Ю. Кутепов, А.П. Крень, Е.В. Гнутенко*
Оценка точности измерения магнитоотрывного усилия датчиками прибора НТ-800 для раннего выявления дефектов их изготовления (in English)..... 230
- Р.В. Лукашевич, Г.А. Фоков*
Расчёт положения эффективного центра энерговыделения сцинтилляционных детекторов для задач калибровки при малых расстояниях «источник–детектор» (in English)..... 239

CONTENTS

Measuring Instruments

- V.A. Alekseev, V.G. Kostin, A.V. Usoltseva, V.P. Usoltsev, S.I. Yuran*
Expanding of Excimer Laser Photoablation’s Functionality in Ophthalmology..... 175
- I.A. Konovalov, A.A. Chesnokov, A.A. Barinov, S.M. Dmitriev, A.E. Khrobostov, M.A. Makarov*
Application of Electrical Impedance Measurements’ Method for Studies of Bubble Flows..... 183
- V.L. Solomakho, A.A. Bagdun*
Determination of the Error in Transferring of Length Unit’s Size when Measuring the Nano-particles’ Diameter Using an Analyzer of Particles’ Differential Electrical Mobility..... 194

Methods of Measurements, Monitoring, Diagnostics

- N.A. Poklonski, I.I. Anikeev, S.A. Vyrko*
Low-Frequency Admittance of Capacitor with Working Substance “Insulator–Partially Disordered Semiconductor–Insulator”..... 202
- A.R. Baev, A.I. Mitkovets, M.V. Asadchaya, A.L., A.L. Mayorov*
Impulsively-Laser Excitation and Propagation of Ultrasonic Waves through Nanomagnetic Fluid..... 211
- V.N. Yakimov*
Digital Spectral Analysis by means of the Method of Averag Modified Periodograms Using Binary-Sign Stochastic Quantization of Signals..... 220
- A. Kutsepau, A. Kren, Y. Hnutsenka*
Evaluation of the Magnet Breakaway Force Measurement Accuracy of the NT-800 Sensors for Early Detection of Defects of Their Manufacturing..... 230
- R. Lukashevich, G. Fokov*
Calculation of the Effective Energy Release Center’s Position of Inorganic Scintillation Detectors for Calibration at Small “Source–Detector” Distances..... 239

Expanding of Excimer Laser Photoablation's Functionality in Ophthalmology

V.A. Alekseev¹, V.G. Kostin², A.V. Usoltseva¹, V.P. Usoltsev¹, S.I. Yuran³

¹Kalashnikov Izhevsk State Technical University,
Studencheskaya str., 7, Izhevsk 426069, Russia

²The vision correction center "EKSP",
Lenina str., 101, Izhevsk 426000, Russia

³Izhevsk State Agricultural Academy,
Studencheskaya str., 11, Izhevsk 426069, Russia

Received 12.08.2021

Accepted for publication 22.09.2021

Abstract

One of the significant weaknesses of excimer laser-based vision correction devices is the difficulty of achieving a required change in the refractive properties of the cornea to sharply focus the image on the retina with distance from the working area (ablation zone) center to the periphery due to a change in the laser beam incidence angle. The study is aimed at improving the quality of laser action on the eye cornea by introducing an optical corrective system into the existing excimer laser vision correction equipment, ensuring the coincidence of the direction of the laser beam incidence on the corneal surface with the normal.

It has been shown that the greater the reflection coefficient, the lower the absorbed energy, and the shallower the laser radiation penetration and ablation depths, which reduces the laser action opportunities and quality. When using excimer laser vision correction devices, it has been proposed to change the angle of the laser beam incidence on the cornea with a distance from the working area (ablation zone) center to the periphery during the surgery by introducing an optical corrective system based on a lightweight controllable and movable mirror, which allows achieving the coincidence of the direction of the laser beam incidence on the corneal surface with the normal.

The studies have shown that the coincidence of the laser beam incidence on the corneal surface at any point with the normal when using a priori data on the specifics of the patient's eye allows expanding the functional opportunities of excimer laser photoablation, i. e., expand the ablation zone by 30 % and eliminate the possibility of errors caused by the human factor. The technique proposed can be used for excimer laser vision correction according to PRK, LASIK, Femto-LASIK, and other methods. To implement this approach, a patented excimer laser vision correction unit has been proposed with a PC-controlled optical shaping system comprising galvo motor platforms and galvo mirrors installed on them.

Keywords: photoablation, optical correction system, excimer-laser vision correction, angle of incidence of the laser beam on the cornea.

DOI: 10.21122/2220-9506-2021-12-3-175-182

Адрес для переписки:

Юран С.И.
Ижевская государственная сельскохозяйственная академия,
ул. Студенческая, 11, г. Ижевск 426069, Россия
e-mail: yuran-49@yandex.ru

Address for correspondence:

Yuran S.I.
Izhevsk State Agricultural Academy,
Studencheskaya str., 11, Izhevsk 426069, Russia
e-mail: yuran-49@yandex.ru

Для цитирования:

V.A. Alekseev, V.G. Kostin, A.V. Usoltseva, V.P. Usoltsev, S.I. Yuran.
Expanding of Excimer Laser Photoablation's Functionality
in Ophthalmology.

Приборы и методы измерений.
2021. – Т. 12, № 3. – С. 175–182.

DOI: 10.21122/2220-9506-2021-12-3-175-182

For citation:

V.A. Alekseev, V.G. Kostin, A.V. Usoltseva, V.P. Usoltsev, S.I. Yuran.
Expanding of Excimer Laser Photoablation's Functionality
in Ophthalmology.

Devices and Methods of Measurements.
2021, vol. 12, no. 3, pp. 175–182.

DOI: 10.21122/2220-9506-2021-12-3-175-182

Расширение функциональных возможностей фотоабляции эксимерным лазером в офтальмологии

В.А. Алексеев¹, В.Г. Костин², А.В. Усольцева¹, В.П. Усольцев¹, С.И. Юран³

¹Ижевский государственный технический университет имени М.Т. Калашникова,
ул. Студенческая, 7, г. Ижевск 426069, Россия

²Центр коррекции зрения «ЭКСИ»,
ул. Ленина, 101, г. Ижевск 426000, Россия

³Ижевская государственная сельскохозяйственная академия,
ул. Студенческая, 11, г. Ижевск 426069, Россия

Поступила 12.08.2021

Принята к печати 22.09.2021

Одним из существенных недостатков устройств для коррекции зрения на основе эксимерных лазеров является трудность достижения заданного изменения преломляющих свойств роговицы для чёткой фокусировки изображения на сетчатке с удалением от центра рабочей зоны (зоны абляции) к периферии в связи с изменением угла падения лазерного луча. Целью исследования являлось повышение качества лазерного воздействия на роговицу глаза за счёт введения в существующую аппаратуру для эксимер-лазерной коррекции зрения оптической корректирующей системы, обеспечивающей совпадение направления лазерного луча, падающего на поверхность роговицы, с нормалью.

Показано, что чем больше коэффициент отражения, тем меньше поглощённая энергия, тем меньше глубина проникновения лазерного излучения и меньше глубина абляции, что снижает возможности и качество лазерного воздействия. Предложено при использовании устройств для эксимер-лазерной коррекции зрения изменять в процессе операции угол падения лазерного луча на роговицу с удалением от центра рабочей зоны (зоны абляции) к периферии за счёт введения оптической корректирующей системы на основе управляемого, лёгкого подвижного зеркала, что позволяет добиться совпадения направления лазерного луча, падающего на поверхность роговицы, с нормалью.

Проведённые исследования показали, что совпадение лазерного луча, падающего на поверхность роговицы в любой точке с нормалью, при использовании априорной информации об индивидуальных особенностях глаза пациента, позволяет расширить функциональные возможности фотоабляции эксимерным лазером, а именно, увеличить зону абляции на 30 % и исключить вероятности ошибок из-за человеческого фактора. Предложенная методика может быть использована для эксимер-лазерной коррекции зрения по методикам PRK, LASIK, Femto-LASIK и др. Для реализации данного подхода предложена защищённая патентом установка для эксимер-лазерной коррекции зрения с управляемой от компьютера оптической формирующей системы, включающей платформы с гальвоприводом и установленными на них гальвозеркалами.

Ключевые слова: фотоабляция, оптическая корректирующая система, эксимер-лазерная коррекция зрения, угол падения лазерного луча на роговицу.

DOI: 10.21122/2220-9506-2021-12-3-175-182

Адрес для переписки:

Юран С.И.
Ижевская государственная сельскохозяйственная академия,
ул. Студенческая, 11, г. Ижевск 426069, Россия
e-mail: yuran-49@yandex.ru

Address for correspondence:

Yuran S.I.
Izhevsk State Agricultural Academy,
Studencheskaya str., 11, Izhevsk 426069, Russia
e-mail: yuran-49@yandex.ru

Для цитирования:

V.A. Alekseev, V.G. Kostin, A.V. Usoltseva, V.P. Usoltsev, S.I. Yuran.
Expanding of Excimer Laser Photoablation's Functionality
in Ophthalmology.
Приборы и методы измерений.
2021. – Т. 12, № 3. – С. 175–182.
DOI: 10.21122/2220-9506-2021-12-3-175-182

For citation:

V.A. Alekseev, V.G. Kostin, A.V. Usoltseva, V.P. Usoltsev, S.I. Yuran.
Expanding of Excimer Laser Photoablation's Functionality
in Ophthalmology.
Devices and Methods of Measurements.
2021, vol. 12, no. 3, pp. 175–182.
DOI: 10.21122/2220-9506-2021-12-3-175-182

Introduction

Ophthalmology was the first medicine branch to use lasers [1–4]. Various lasers with wavelengths from 193 nm to 10.6 μm are used to treat eye diseases. The nature of laser radiation impact differs for various biomaterials with specific properties. Accordingly, in each case, specific parameters are chosen: wavelength, duration of exposure, power, pulse repetition rate, etc. [5]. The laser radiation wavelength determines the application area of the laser in ophthalmology. Excimer lasers emit energy in the UV range (193–351 nm wavelength). These lasers allow removing specific surface layers of tissue with an accuracy of 500 nm using photoablation (evaporation).

Vision correction technology is based on profiling the cornea's outer surface. Removing tissue in the central area corrects myopia [6], evaporation of the cornea peripheral part allows correcting hyperopia, and dosed removal in different cornea meridians allow eliminating astigmatism [7]. Despite the widespread use of excimer lasers for vision correction, such devices have a significant drawback, i. e., the difficulty of achieving a required change in the refractive cornea properties (upward or downward) to accurately focus the image on the retina with a distance from the working area (ablation zone) center to the periphery due to a change in the laser beam incidence angle. This limits side vision; peripheral, binocular vision deteriorates; in the dark, problems occur, associated with a contrast decay, nocturnal myopia, glare, and halos. Higher-order aberrations are also difficult to correct.

In this regard, the study is aimed at improving the quality of laser action on the eye cornea by introducing an optical corrective system into the existing excimer laser vision correction equipment, ensuring the coincidence of the direction of the laser beam incidence on the corneal surface with the normal.

Approaches used

Like any optical system, the human eye features optical defects – aberrations deteriorating the vision quality by distorting the image on the retina. Aberration is any angular deviation of a narrow parallel light beam from the point of ideal intersection with the retina as it passes through the entire optical system of the eye. In technical

optics, the optical system quality is determined by the aberrations of a plane or spherical front of a light wave passing through this system. Thus, an eye without aberrations has a flat wavefront and ensures the most accurate point source image on the retina (the so-called Airy Disk, the size of which depends only on the pupil diameter). But normally, even with 100 % visual acuity, optical defects of the light-refracting eye surfaces distort the beam path and form an incorrect wavefront distorting the image on the retina. The quantitative characteristics of the image's optical quality are the root-mean-square errors in the real wavefront deviation from the ideal one. German mathematician Zernike suggested using a series of polynomials to describe wavefront aberrations. An optical system is considered good if the Zernike coefficients are close to zero and, therefore, the wavefront root-mean-square error is less than 1/14 of the light wavelength (Marechal criterion). This coefficient allows forecasting visual acuity by simulating the image of any optotypes on the retina.

There are excimer laser-based vision correction devices, using the following laser methods and technologies to correct vision:

- Flying Spot technology. Its distinctive feature is the flying spot system – the excimer laser beam “flies” all over the treatment area surface and polishes the cornea by shooting a large number of laser pulses. The damage is minimal due to splitting the energy into mini-pulses;

- Eye Tracking technology. The vision correction excimer laser is equipped with a control system pointing the laser beam at the area to be treated with micrometer precision. This laser technology compensates for the patient's all involuntary eye movements. Its precision allows using it to treat patients with eye twitching syndrome (nystagmus);

- Topographic Laser Treatment technology. The topographic excimer laser system allows using it, considering the specifics of each eye. This means that only certain cornea areas will be evaporated, while the rest are saved. Topographic technology is especially widely used for postoperative correction (e. g., scars, irregular astigmatism).

All the absorbed laser radiation energy E is spent to heat the biological tissue volume V_0 to the boiling point $T_b - (E_1)$ and evaporate this biological tissue volume (E_2) (with the widespread assumption of identification of biological tissue with water). The E energy is determined by the equation:

$$E = E_1 + E_2 = P_a t = C_p m \Delta T + \chi m = C_p \rho h_0 \Delta T d_0^2 / 4A + \rho \chi d_0^2 / 4A = \rho h_0 (C_p \Delta T + \chi) d_0^2 / 4A, \quad (1)$$

where P_a is the absorbed radiation power, W; t is the time of the biological tissue exposure to laser radiation, s; C_p is the specific heat capacity of biological tissue, kJ/deg·kg; m is the mass of heated and evaporated biological tissue, kg; ρ is the biological tissue density, kg/m³; d_0 is the Gaussian beam diameter, m; h_0 is the radiation penetration depth at the $1/e^2$ level; ΔT is the increment of the biological tissue temperature when heating, °C ($\Delta T = T - 36.6$ °C); χ is the specific energy of water evaporation, kJ/kg.

Considering the calculated value of the coefficient $A = 2.31$, equation (1) will take the form:

$$E = 0.34 \rho d_0^2 h_0 (C_p \Delta T + \chi). \quad (2)$$

According to equation (2), the energy spent on heating and evaporating biological tissue is proportional to the radiation penetration depth h and the temperature T required to achieve any thermal and, hence, surgical effect (ablation temperature $T = 250\text{--}300$ °C).

Ablation (from Late Latin *ablatio* – taking away) is removing material from a solid surface with a stream of hot gas. Laser ablation is removing material from a surface with a laser pulse. At low laser power, materials evaporate or sublime in the form of free molecules, atoms, and ions, forming a weak non-luminous plasma, usually dark, over the irradiated surface. When the laser pulse power density exceeds the ablation regime threshold, a micro explosion occurs, forming a crater on the material surface and a luminous plasma.

The absorbed energy E is less than the incident energy and depends on the reflection coefficient (K_{ref}):

$$E = [1 - (K_{ref} + K_{tr})] P t / S, \quad (3)$$

where P is the radiation power, W; t is the exposure time, s; S is the irradiation area, m²; K_{ref} is the laser beam reflection coefficient; K_{tr} is the transmittance of the irradiated biological tissue.

For wavelengths of 0.63 and 0.89 μm, the biological tissue transmittance is 0.12 and 0.41, respectively.

According to equation (3), the higher the reflection coefficient, the lower the absorbed energy, and the shallower the laser radiation penetration and ablation depths.

Figure 1 plots the dependence of the reflection coefficients for the *TM*-wave (the light polarization state, where the electric vector is perpendicular to the incidence plane) and the *TE*-wave (the polarization state, where the electric vector lies in the polarized light incidence plane) on the incidence angle. For unpolarized light, the curve will pass in the middle.

As the plot shows, with an increase in the incidence angle over 10°, the reflection coefficient starts increasing, and with an angle over 60°, it starts growing sharply.

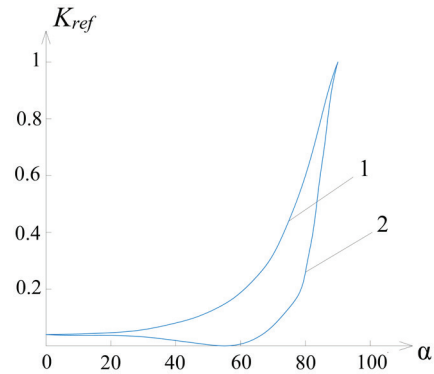


Figure 1 – The dependence of the reflection coefficients K_{ref} for the polarized light *TE*-wave (curve 1) and *TM*-wave (curve 2) on the incidence angle

When the laser beam deviates from the normal, the reflection coefficient increases and can reach unity when the laser beam is fully reflected. Considering that the incidence angle is the angle between the laser beam incident on the cornea surface and the normal to the surface at the incidence point (Figure 2), in the working area center, the laser beam incidence angle OAO is zero, and with a maximum working area diameter of 8.2 mm, depending on the distance from the optical shaping system to the cornea, can reach 60° (OBC angle).

The correction system operating principle and the study results

To reduce the laser beam deviation from the normal and, accordingly, the beam reflection coefficient, an optical corrective system is required. Directing a laser beam OB with a given laser radiation wavelength using this system onto a reflective surface, i. e., a relatively lightweight control-lable movable mirror with a coating capable of reflecting the laser beam at a relatively high speed and located appropriately, the coincidence of the direction of the laser beam incidence on the corneal surface with the normal can be achieved (OCB angle in Figure 3).

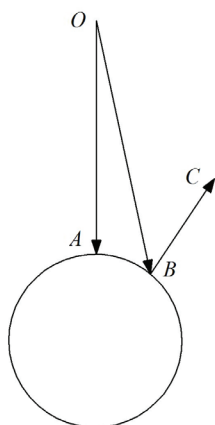


Figure 2 – The angle of the laser beam incidence on the cornea

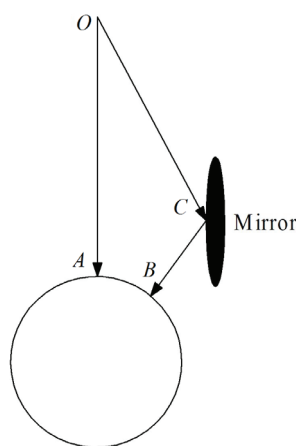


Figure 3 – The angle of the laser beam incidence on the cornea with a mirror

The proposed approach allows expanding the device functionality by changing the laser beam incidence angle on the cornea with distance from the working area (ablation zone) center to the periphery. It also allows changing the laser operating modes directly during the surgery, while eliminating the likelihood of errors caused by the human factor.

The technical result obtained in this case is achieved by introducing an optical correcting system comprising platforms with a galvo drive and galvo mirrors installed on them into the excimer laser vision correction device consisting of an excimer laser, a laser operating mode control unit, an optical shaping system, a computer, and an algorithm controller [8].

The proposed technique can be used for excimer-laser vision correction according to PRK.

The studies have shown that the coincidence of the laser beam incidence on the corneal surface at any point with the normal when using a priori data on the specifics of the patient's eye allows

expanding the functional opportunities of excimer laser photoablation. The technique proposed can be used for excimer laser vision correction according to PRK (Photorefractive Keratectomy), LASIK (Laser Keratomileusis), Femto-LASIK, and LASEK [9–12]).

Along with obtaining a required corneal profile, the corneal surface quality in the ablation zone is of great importance [13–15].

For the stable operation of the complex proposed, the mirror rotation should be controlled until the laser beam coincides with the normal. To do this, the mirrors are made semitransparent, and a reflected light flux sensor is installed in the center of the mirrors. By the reflected light flux energy, the beam coincidence with the cornea normal is controlled. The sensor is installed on the reverse side of the mirror does not interfere with the mirror operation in directing the light flux to a given area of the cornea. The sensor is connected to a digital measuring system transmitting data to a computer, which estimates the beam coincidence with the normal and generates control signals to move (rotate) the mirrors.

The problem of adjusting the mirrors to achieve the laser beam coincidence with the normal is reduced to that of finding an extremum on the reflected radiation energy curve. Adjustment takes a certain time and is performed under the condition of the minimum laser beam energy not affecting the cornea. After the adjustment, with the chosen mirror positions, a therapeutic or surgical procedure can start with an increase in the laser energy.

However, there is an issue with the cornea surface irregularity. If the beam aperture is less than the corneal surface irregularities, then the beam tuning will be complicated since the beam reflection will depend on the shape and size of the surface irregularities.

When the laser beam probes the cornea, the reflection of the beam from the surface, associated with the corneal irregularity, will depend on the corneal surface irregularity (Figure 4), where d_1 is the expanded beam aperture, d_2 is the beam aperture less than the irregularity element size h . In this case, if the beam aperture is less than the irregularity size ($d_2 \leq h$), then the beam reflection will depend on the irregularity element geometry. If the beam aperture is much more than all the irregularities ($d_1 \gg h$), then the maximum reflection will be achieved when the beam coincides with the normal. It is also known that according to Rayleigh law, the irregularity size

should be less than the probing radiation wavelength to talk about the corneal surface smoothness.

Therefore, the beam tuning aperture should be several times larger than the size of irregularities.

In this case, there are two approaches to choosing the aperture:

1. The tuning aperture is the same as that the treatment one.
2. The tuning aperture is larger than the treatment one.

To compare different approaches, statistics on the nature (irregularities) of the cornea in different patients should be obtained.

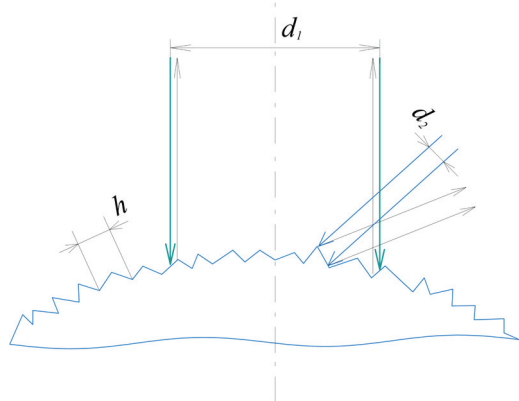


Figure 4 – The laser beam reflection from the cornea surface

A different laser radiation wavelength can be used for tuning, which may improve the tuning accuracy, but in this case, the optical transmission scheme should coincide with that of the main laser. To do this, fiber-optic lines and schemes for converting radiation from two lasers to a common one for probing the cornea can be used.

The created complex has two operating modes:

- 1 – adjusting the complex on a patient at low radiation energy with an enlarged aperture using one or two lasers.
- 2 – a working situation when the main laser beam aperture reduces with an increase in the radiation energy to that required for the specific treatment.

To check the correctness of using the proposed technique to set the laser radiation exposure modes, a step wedge has been reproduced¹ when changing the direction of the laser beam incidence on the material (plexiglass). For the experiment, PMMA acrylic glass has been used to adjust and set the Laser Scan unit modes from zero to 30°. To measure micro

¹ GOST 24930–81. Facsimile Equipment Gray Scale. Moscow: Publishing House of Standards, 1981, 7 p.

irregularities on the sample outer surface, an MII-4 interference microscope was used².

According to the scientific and technical requirements for the surface roughness, the arithmetic mean deviation of the profile and the height of the profile irregularities taken at 10 points at the same step have been determined and calculated. The random value of the profile irregularities x_i has a discrete random distribution; then the arithmetic mean profile deviation is determined by the formula:

$$M(x) = \frac{\sum_{i=1}^N x_i}{N}, \quad (4)$$

where N is the number of surface micro irregularity measurements for one wedge step.

The results of the calculation by equation (4) are shown in Figure 5.

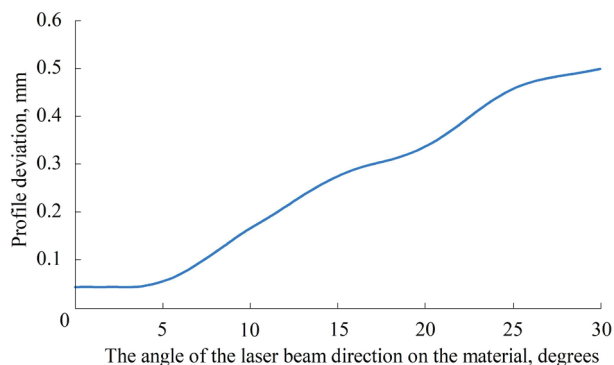


Figure 5 – The arithmetic mean deviation of the surface micro irregularities

The central limit theorem allows asserting that whenever a random variable is a result of adding a large number of independent random variables, the variances of which are small compared to that of the sum, this random variable distribution law turns out to be virtually a normal law. Since random variables are always generated by an infinite number of reasons, and most often none of them has a variance comparable to that of the random variable itself, then most of the random variables occurring in practice are subject to the normal distribution law. The literature data do not contradict this. According to the law of large numbers, the random micro irregularity mean values have a normal distribution. Therefore, according to the three-sigma rule (3σ), almost

² Interference Microscope MII – 4 [Electronic resource]. Microscopes and Accessories [Site]. URL: <http://www.mbs10.ru/mii-4.html> (date of access: 03.17.2021).

all values of a normally distributed random variable lie within the interval $(M(x) - 3\sigma; M(x) + 3\sigma)$ with a probability of 0.997, where $M(x)$ is the mathematical expectation. For clarity of data presentation, the variance has been calculated. The calculation results are shown in Figure 6.

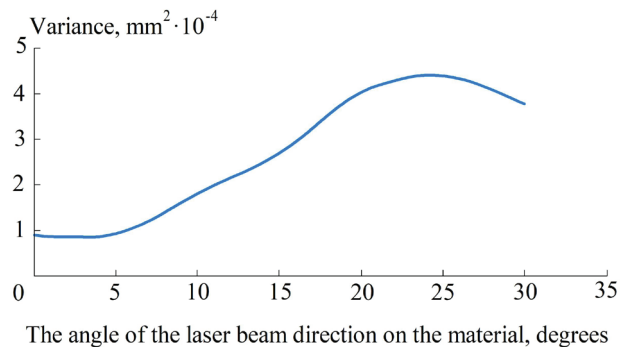


Figure 6 – Dispersion of the surface profile deviation

From a visual point of view, dispersion is an indicator of the plexiglass surface micro irregularity. Dispersion is a measure characterizing the spread of values of a random micro irregularity variable x_i relative to its mathematical expectation $M(x)$. If the variance is small, then the random variable values x_i are close to each other. If it is large, the values x_i are far from each other. The random variable x_i variance is calculated by the following formula:

$$D(x) = \frac{1}{n-1} \sum_{i=1}^n (x_i - M(x))^2,$$

where n is the random variable x_i measurement number.

Conclusion

The analysis of the optical corrective system characteristics has shown that changing the laser operating modes directly during the surgery is promising for expanding its functionality by changing the laser beam incidence angle on the cornea with distance from the working area (ablation zone) center to the periphery, thereby eliminating errors caused by the human factor.

The changes to the system design allow controlling the beam aperture and radiation energy. Depending on the algorithm chosen, two operating modes are possible: tuning and treatment. Thereat, in the tuning mode, a laser with a different radiation wavelength can be additionally used. These procedures can be controlled by a

computer. Improving the system functionality allows for an effective treatment. The calculation and experimental results show that the ablation zone can be increased by 30 %.

The scientific and technical solutions provided herein can be used in both creating new treatment complexes in ophthalmology and improving existing ones.

References

1. Balashevich L.I. [Surgical correction of refractive anomalies and accommodation]. *Hirurgicheskaya korrakciya anomalij refrakcii i akkomodacii*. SPb.: CHelovek Publ., 2009, 296 p.
2. Vestergaard A.H. Past and present of corneal refractive surgery: a retrospective study of long-term results after photorefractive keratectomy and a prospective study of refractive lenticule extraction. *Acta Ophthalmol*, 2014, vol. 92, pp. 1–21. DOI: 10.1111/aos.12385
3. Kornilovskij I.M. [New technologies of excimer laser surgery of the cornea]. *Sovremennye tekhnologii v oftal'mologii* [Modern technologies in ophthalmology], 2020, no. 4 (35), pp. 94 (in Russian). DOI: 10.25276/2312-4911-2020-4-70-71
4. Kanski Dzh. [Clinical ophthalmology. A systematic approach]. *Klinicheskaya oftal'mologiya. Sistematizirovannyj podhod*. Moscow: Logosfera, Elsevier Urban & Partner Publ., 2009, 944 p.
5. Hampton F.R. *Refrakcionnaya hirurgiya (Hirurgicheskie tekhniki v oftal'mologii)* [Refractive Surgery (Surgical techniques in ophthalmology)]: (eds. S.E. Avetisova, V.P. Elicheva, I.A. Bubnovoj). Moscow: Logosfera Publ., 2016, 248 p.
6. Ehlke Germano Leal, Krueger Ronald R. Laser Vision Correction in Treating Myopia. *Asia Pac J. Ophthalmol (Phila)*, 2016, Nov/Dec. 5(6), pp. 434–437. DOI: 10.1097/APO.0000000000000237
7. Cionni R.J., Hamilton R., Stonecipher K.G. Toric IOLs for irregular astigmatism. *Cataract Refract. Surg. Today*, 2014, vol. 9, pp. 40–42.
8. Alekseev V.A., Kostin V.G., Usoltseva A.V., Usoltsev V.P. *Ustrojstvo dlya eksimer-lazernoj korrakcii zreniya* [Device for excimer laser vision correction]. Patent RF, no. 201585, 2020 (in Russian).
9. Artola A., Gala A., Belda J.I., Pérez-Santonja J.J., Rodríguez-Prats J.L., Ruiz-Moreno J.M., Alió J.L. LASIK in myopic patients with dermatological keloids. *J. Refract. Surg.*, 2006, vol. 22 (5), pp. 505–508.
10. Barequet I.S., Hirsh A., Levinger S. Femtosecond thin-flap LASIK for the correction of ametropia after penetrating keratoplasty. *J. Refract. Surg.*, 2010, vol. 26, no. 3, pp. 191–196.

11. Munoz G., Albarran–Diego C., Sakla H., Pérez-Santonja J.J., Alió J.L. Femtosecond laser in situ keratomileusis after radial keratotomy. *J. Cataract Refract. Surg.*, 2006, vol. 32, no. 8, pp. 1270–1275.

DOI: 10.1016/j.jcrs.2006.02.061

12. Buratto L., Brint S. LASIK Surgical Techniques and Compilations. Thorofare, NJ: SLACK, 2000, 624 p.

13. Kachalina G.F., Tahchidi N.H. [Investigation of the smoothness of the ablation surface and thermal processes in the rabbit cornea during the operation of excimer laser installations “MicroScan-Visum” and “MicroScan-CFP”]. *Issledovanie gladkosti ablyacionnoj poverhnosti i*

termicheskikh processov v rogovice krolika pri rabote ekzimer-lazernykh ustanovok “MikroSkan-Vizum” i “MikroSkan-CFP”. *Vestnik RGMU*, 2016, no. 2, pp. 50–53 (in Russian).

14. Verma Sh., Hesser Ju., Arba-Mosquera S. Optimum Laser Beam Characteristics for Achieving Smoother Ablations in Laser Vision Correction. *Invest Ophthalmol Vis Sci.*, 2017, Apr. 1, 58(4), pp. 2021–2037.

DOI:10.1167/iovs.16-21025

15. Argento C., Valenzuela G., Huck H., Cremona G., Cosentino M.J, Gale M.F. Smoothness of ablation on acrylic by four different excimer lasers. *J. Refract Surg.*, 2001, no. 17 (1), pp. 43–45.

Application of Electrical Impedance Measurements' Method for Studies of Bubble Flows

I.A. Konovalov, A.A. Chesnokov, A.A. Barinov, S.M. Dmitriev, A.E. Khrobostov,
M.A. Makarov

Nizhny Novgorod State Technical University n.a. R.E. Alekseev,
Minin str., 24, Nizhny Novgorod 603950, Russia

Received 28.09.2021

Accepted for publication 06.10.2021

Abstract

One of the important tasks in carrying out a computational justification of the reliability and safety of equipment that is part of the projected nuclear power plants today is the modeling of the bubbly regime of the coolant flow. In this regard the aim of this work is the use of extended methods of using matrix conductometric systems which are widespread in research practice for study of gas-liquid flows.

The work uses a method of primary processing of experimental data aimed at eliminating of excess conductivity in the cells of the developed wire mesh sensor which makes it possible to obtain the values of the true volumetric gas content in the investigated area.

Subsequent analysis of the possibilities to estimate the volumes of registered gas bubbles by the gradient method as well as the size of the interface in the sensor cells which plays a key role in modeling the interfacial heat and mass transfer.

Comparison of readings values with the control instruments cues showed a good agreement. The presented work is an adaptation of the use of a conductometric measuring system for the study of multicomponent flows with the aim of further application for the study of two-component flows in the channels of the core simulator using wire mesh sensors.

Keywords: wire mesh sensor, two-layer wire mesh sensor, bubble flow.

DOI: 10.21122/2220-9506-2021-12-3-183-193

Адрес для переписки:

Коновалов И.А.
Нижегородский государственный технический университет,
ул. Минина, 24, г. Нижний Новгород 603950, Россия
e-mail: iliakonowaloff@yandex.ru

Address for correspondence:

Konovalov I.A.
Nizhny Novgorod State Technical University,
Minin str., 24, Nizhny Novgorod 603950, Russia
e-mail: iliakonowaloff@yandex.ru

Для цитирования:

I.A. Konovalov, A.A. Chesnokov, A.A. Barinov, S.M. Dmitriev,
A.E. Khrobostov, M.A. Makarov.

Application of Electrical Impedance Measurements' Method
for Studies of Bubble Flows.

Приборы и методы измерений.

2021. – Т. 12, № 3. – С. 183–193.

DOI: 10.21122/2220-9506-2021-12-3-183-193

For citation:

I.A. Konovalov, A.A. Chesnokov, A.A. Barinov, S.M. Dmitriev,
A.E. Khrobostov, M.A. Makarov.

Application of Electrical Impedance Measurements' Method
for Studies of Bubble Flows.

Devices and Methods of Measurements.

2021, vol. 12, no. 3, pp. 183–193.

DOI: 10.21122/2220-9506-2021-12-3-183-193

Применение электроимпедансного метода измерений при исследовании пузырьковых режимов течения двухкомпонентного потока

И.А. Коновалов, А.А. Чесноков, А.А. Баринов, С.М. Дмитриев, А.Е. Хробостов, М.А. Макаров

*Нижегородский государственный технический университет имени Р.Е. Алексеева,
ул. Минина, 24, г. Нижний Новгород 603950, Россия*

Поступила 28.09.2021

Принята к печати 08.10.2021

Одной из важных задач при проведении расчётного обоснования надёжности и безопасности оборудования, входящего в состав проектируемых ядерных энергетических установок, на сегодня является моделирование пузырькового режима течения теплоносителя. В связи с этим, целью данной работы являлось изучение особенностей движения газового пузыря в жидкой среде, а также отработка и расширение методических особенностей применения матричных кондуктометрических систем, получивших широкое распространение в исследовательской практике, для исследования газожидкостных потоков.

В работе изложен способ первичной обработки экспериментальных данных, направленный на устранение избыточной проводимости в ячейках разработанного сетчатого датчика, что позволило получить значения истинного объёмного газосодержания в исследуемой области.

Последующий анализ позволил оценить объёмы регистрируемых газовых пузырей градиентным методом, а также величину плотности межфазной поверхности в ячейках датчика, которая играет ключевую роль при моделировании межфазного тепло- и массообмена.

Сравнение полученных величин с показаниями контрольно-измерительных приборов экспериментальной установки показало хорошую степень соответствия. Представленная работа является адаптацией применения кондуктометрической измерительной системы для исследования многокомпонентных потоков с целью дальнейшего применения для исследования двухкомпонентных потоков в каналах имитатора активной зоны при помощи сетчатых кондуктометрических датчиков.

Ключевые слова: сетчатый кондуктометрический датчик, двухслойный датчик, пузырьковое течение.

DOI: 10.21122/2220-9506-2021-12-3-183-193

Адрес для переписки:

Коновалов И.А.
Нижегородский государственный технический университет,
ул. Минина, 24, г. Нижний Новгород 603950, Россия
e-mail: iliakonowaloff@yandex.ru

Address for correspondence:

Konovalov I.A.
Nizhny Novgorod State Technical University,
Minin str., 24, Nizhny Novgorod 603950, Russia
e-mail: iliakonowaloff@yandex.ru

Для цитирования:

I.A. Konovalov, A.A. Chesnokov, A.A. Barinov, S.M. Dmitriev,
A.E. Khrobostov, M.A. Makarov.

Application of Electrical Impedance Measurements' Method
for Studies of Bubble Flows.

Приборы и методы измерений.

2021. – Т. 12, № 3. – С. 183–193.

DOI: 10.21122/2220-9506-2021-12-3-183-193

For citation:

I.A. Konovalov, A.A. Chesnokov, A.A. Barinov, S.M. Dmitriev,
A.E. Khrobostov, M.A. Makarov.

Application of Electrical Impedance Measurements' Method
for Studies of Bubble Flows.

Devices and Methods of Measurements.

2021, vol. 12, no. 3, pp. 183–193.

DOI: 10.21122/2220-9506-2021-12-3-183-193

Introduction

Justification of the reliability, safety and efficiency of nuclear power plant circuits is an important task for developers. The success is directly related to the introduction of new technical solutions which in turn require a preliminary numerical simulations.

The operating modes of power equipment are determined by a set of hydrodynamic processes often accompanied by the presence of a two-component flow. For example some Russian projects of low and medium power NPPs use gas pressurizers which causes the dissolution of N_2 in the primary coolant. During normal operation of the system, the concentration of dissolved gas in the pressurizer and the primary coolant comes to a certain stationary distribution, however power variation and a change in the primary coolant temperature in a number of modes causes the release of a gas phase as well as a change in the conditions of gas solubility in the coolant, which can lead to a violation in the operation of the primary circuit equipment:

- loss of head, deviation from the nominal characteristics during the operation of the circulation pumps;

- deterioration of heat transfer, entailing wall boiling on the fuel element cladding, which leads to an increase in temperature and the risk of local burnout with subsequent corrosion;

- disturbances in the operation of control and measuring devices.

In addition there is a problem of studying the structure of a gas-liquid flow, since two-component flows play a major role in such processes as cavitation, bubbling and many others. In particular, the hydrodynamics of gas-liquid flows determines the operability of some passive safety systems for promising nuclear power plants of low and medium power.

These phenomena require the solution of an extensive number of computational problems aimed at substantiating the reliability and safety of nuclear power plants, taking into account the presence of two-component flows in their elements. The solution of these problems with the use of computational fluid dynamics (CFD) programs requires the determination of the interphase surface necessary for calculating the mass and energy fluxes across the interface [1, 2]. At the same time, the need to test the predictive ability of the mathematical models requires the development

of experimental methods for measurements in two-phase flows.

In research practice to study the hydrodynamic characteristics of flows in the elements of power plants, the method of matrix conductometry is widely used. The measuring system built on its basis is used, in particular, as part of several validation test facilities [3, 4].

Thus the purpose of this work was to study the features of the movement of a gas bubble in a liquid medium as well as to develop and expand the conductometric methodology for gas-liquid flows investigations.

Test facility

To track the motion of a single bubble, the method of matrix conductometry [5] was used in this work which is based on the measurement of the conductivity of the medium at the sensor points. Conductometric measuring system consists of the impedance measurement system LAD-36 [6] and 2-layer wire mesh sensor (WMS) depicted at the Figure 1.

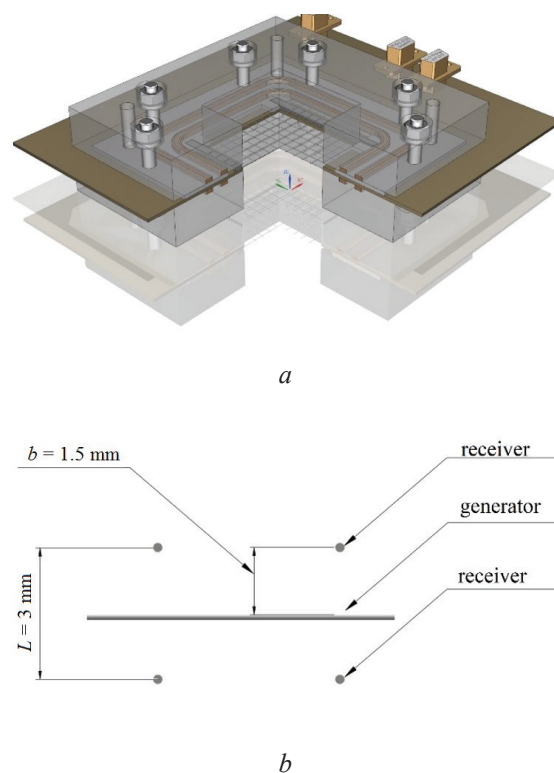


Figure 1 – Schematic representation of a two-layer sensor: *a* – general view of a two-layer wire mesh sensor; *b* – spatial arrangement of the wire mesh sensor electrodes

The use of two layers of cells formed by the three layers of wire electrodes makes it possible to place two measuring planes in one housing with a small axial distance which allows to estimate the velocity of single bubbles [7]. It should be noted that within the framework of the investigations the application of the conductometry method was used

for determining the presence or absence of electrical impedance in the considered measurement region.

The experimental section included a square channel with a two-layer mesh conductometric sensor a bubble injection system, LED illumination and external video camera. The experimental setup is shown schematically at the Figure 2.

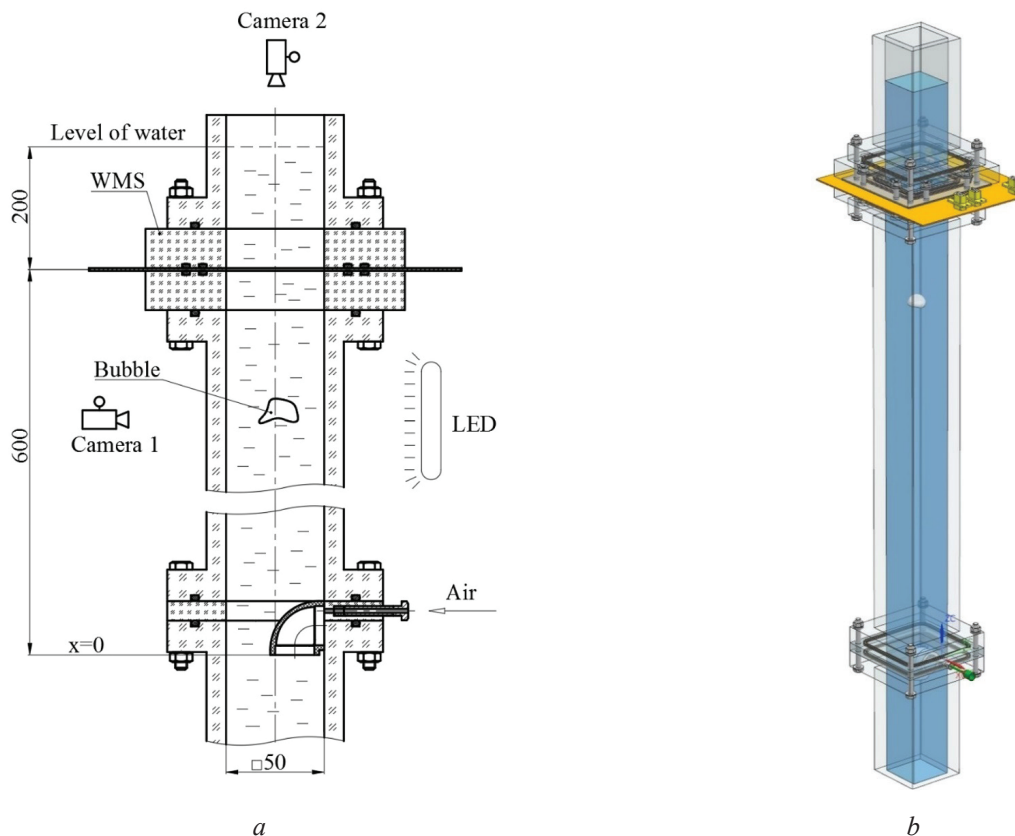


Figure 2 – Experimental setup: *a* – sketch of the test section; *b* – general view of the test model

The mesh sensor was installed 600 mm above the injection section. The arrangement and numbering of the WMS cells are shown at the Figure 3.

One of the main tasks in a similar experimental setup is the creation of sufficiently large gas bubbles that can be accurately identified by a mesh sensor with a given resolution. In this work injection facility was made as a bend with 20-mm diameter directed downward (Figure 4). When gas is supplied to the injection tube the surface tension forces of the water hold the bubble at the bend’s outlet until it becomes large enough for the buoyancy force to prevail over the surface tension forces. This mechanism ensures the creation of bubbles of approximately the same size having a diameter of about 3–4 WMS cells in the cross section of the channel.

Figure 5 shows a the growth of a gas bubble in the injection section before separation and subsequent emergence.

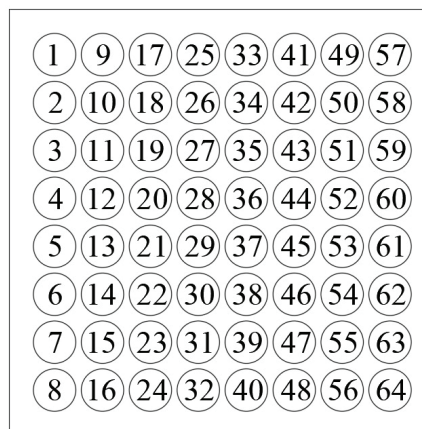


Figure 3 – Accepted cell numbering of the measuring area of the wire mesh sensor

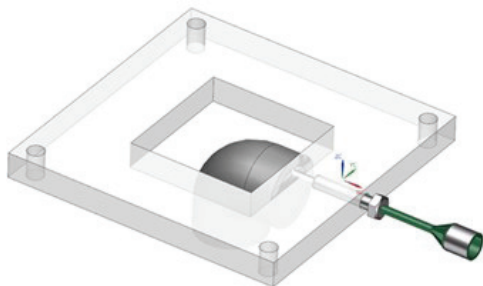


Figure 4 – General view of the injection section



Figure 5 – Growth of a gas bubble before separation and subsequent

Video record was carried out at a frequency of 60 frames per second. The LED backlight was used to increase the contrast of the image.

Setting up an experiment

A series of experimental studies carried out at this work were aimed primarily at the testing of the WMS and measurement system to track the 2-phase flows. In this regard the experimental modes were organized in two ways:

- detection of the passage of single bubbles through the mesh sensor was used to debug the algorithm for the primary processing of experimental data;

- detection of the passage of a series of bubbles through the WMS with a known amount of gas injected into the model during the experiment. This tests were used to debug the algorithms for identifying the time intervals for the implementation of the conductivity corresponding to the passage of the bubble through the WMS, as well as for the direct assessment of the bubble volume.

The test model was filled with a tap water (conductivity $\approx 800 \mu\text{S}/\text{cm}$) with the level maintained at 200 mm above the WMS. Atmospheric air was used as a gas phase due to its low solubility at room temperature. As a result the interfacial mass transfer was neglected in the experiments.

The test parameters are summarized in Table 1.

Table 1

Parameters of the tests

No	Number of bubbles larger than 5 mm	Total volume of injected gas, ml	Temperature, °C	Duration, s
1	5	9.0	28.3	30
2	5	9.0	27.9	30
3	5	9.0	27.5	30

Method of experimental data processing

The primary data are the values of the absolute conductivity of the medium $G_{i,j,z,k}$ [μS], obtained by the LAD-36 system and software package FT40-WMS. Here i is the number of the generator electrode (by X axis), j is the number of the receiver electrode (by Y direction), z is the number of the WMS layer (by Z axis), k is the number of the measurement sample.

In the ideal case the value $G_{i,j,z,k}$ will be determined only by the intrinsic resistance of the medium in the measuring cell of the sensor however in practice the recorded conductivity also includes components depending on the resistance of the WMS electrode material uneven distances between the electrodes of receivers and generators over the cross section as well as the presence of various deposits on the surface of the electrodes.

In order to exclude the influence of these values on the experimental data, a preliminary calibration of the WMS was carried out. Due to the fact that conductivity of the air can be neglected, the calibration procedure takes the form:

$$g_{i,j,z,k} = \frac{G_{i,j,z,k}}{G_{i,j,z}^{cal}}, \quad (1)$$

where $\overline{G_{i,j,z}^{cal}}$ is the averaged value of the fluid conductivity in the cell $\{i, j, z\}$ during calibration, μS .

For the assessment $\overline{G_{i,j,z}^{cal}}$ a calibration measurement of the absolute steady state conductivity $G_{i,j,z,k}^{cal}$ of the liquid was used:

$$\overline{G_{i,j,z}^{cal}} = \frac{1}{N_{cal}} \sum_{k=1}^{N_{cal}} G_{i,j,z,k}^{cal}, \quad (2)$$

where N_{cal} is the number of the calibration counts.

Duration of the calibration measurements was 30 s.

Subsequent analysis of the experimental data showed the presence of a local increase in conductivity exceeding the conductivity of the liquid phase when the gas bubble approaches the measuring plane of the WMS – hereinafter referred to as “overshoots” of conductivity. A similar phenomenon was observed in [8]. An example of test data with conductivity overshoots is shown in Figure 6.

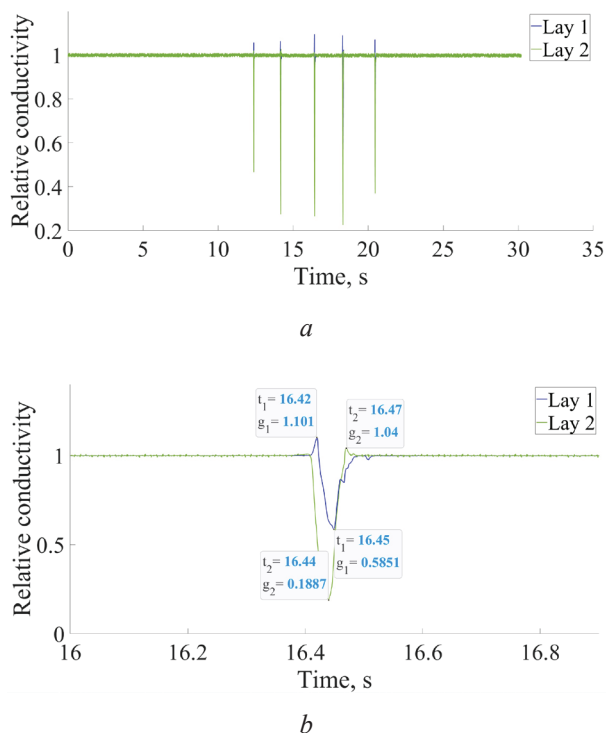


Figure 6 – Typical signal with conductivity overshoots (cell 27) in experiment N1: *a* – general view of the signal realization; *b* – detail view of peak of conductivity corresponding to 3rd bubble passing through wire mesh sensor

The nature of overshoots can be explained by the violation of the symmetry of the measuring cell. In other words the presence in the neighboring cell of a certain amount of gas not large enough to come into contact with both the generating and receiving electrodes and as a consequence of this a sharp increase in its resistance will cause an increase in the current through the cell under consideration which in turn will cause a local increase in the measured conductivity.

In most works aimed at studying gas-liquid flows, such conductivity overshoots are eliminated by methods one way or another based on the “linear

cut” method [9] in which the local instantaneous gas content is calculated as:

$$\varepsilon_{i,j,z,k} = \begin{cases} 1, & g_{i,j,z,k} > 1; \\ 1 - g_{i,j,z,k}, & 0 \leq g_{i,j,z,k} \leq 1; \\ 0, & g_{i,j,z,k} < 0. \end{cases} \quad (3)$$

However from the point of physics this procedure is not fully justified since it leads to a violation of the of conductivity balance at the WMS plane. In addition in [10] it was shown that the elimination of conductivity overshoots by the linear cut method leads to an overestimation of the value of the instantaneous local gas content when using mesh sensors.

In this work it is proposed to use the method of rebalancing conductivities [8] modified by taking into account the features of the used measuring system. Let's consider it in more detail.

In accordance with the above reasons for the occurrence of overshoots it seems logical to redistribute the excess conductivity in the cell under consideration (donor cell) over the neighboring cells in which the conductivity $g_{rec} < 1$ (receptor cells). In [8] it was also noted that the occurrence of an overshoot in the donor cell may be due to the cumulative effect of several cells which gives space for the development of more advanced rebalancing models. In this work it was assumed that the occurrence of excess conductivity in a cell is influenced by only 26 neighboring cells forming so-called “cubic Moore neighborhood” (Figure 7).

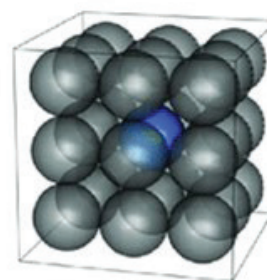


Figure 7 – Graphic representation of the Moore neighborhood for the selected point (highlighted in blue)

Rebalancing of conductivities is carried out as follows:

$$g_{rec,cor} = \begin{cases} g_{rec} + g_{don} - (1 + 0.5 \cdot \sigma), & g_{rec} + g_{don} \leq 2 + \sigma; \\ 1, & g_{rec} + g_{don} > 2 + \sigma; \end{cases} \quad (4)$$

$$g_{don,cor} + 0.5 \cdot \sigma = \begin{cases} 1, g_{rec} + g_{don} \leq 2 + \sigma; \\ g_{don} + g_{rec} - (1 + 0.5 \cdot \sigma), g_{rec} + g_{don} > 2 + \sigma, \end{cases} \quad (5)$$

where σ – a parameter characterizing the intrinsic noise of the measuring system, which makes an additional contribution to the conduction overshoot (i. e., is added to g_{don}).

The value σ is determined from the calibration measurements:

$$\sigma_{i,j,z} = \frac{\max(G_{i,j,z}^{cal})}{G_{i,j,z}^{cal}} - 1. \quad (6)$$

The procedure for rebalancing conductivities (4) and (5) is performed as long as the excess conductivity exists in the donor cell. At each iteration the Moore space cell with the lowest conductivity is selected as the receptor cell.

It can be shown that the total conductivity of the receptor and donor cells in this case will not change, for this we sum up equations (4) and (5):

$$g_{don,cor} + g_{rec,cor} = \begin{cases} g_{rec} + g_{don} \cdot g_{rec} + g_{don} \leq 2; \\ g_{don} + g_{rec} \cdot g_{rec} + g_{don} > 2. \end{cases} \quad (7)$$

Nevertheless, situations are possible in which the assumption about the influence of only neighboring cells is incorrect (due to the geometry of the measuring region, etc.). In this case the conductivity overshoot cannot be completely eliminated by the rebalancing method, as a result of which it is advisable to use a threshold filter with a width $K_t \cdot \sigma$ (along the ordinate), where K_t is the tuning coefficient determined during calibration; for the considered experiments $K_t = 1.02$. An example of realizations of conductivity before (overshoots of conductivity greater than 1 are visible) and after the rebalancing procedure is shown at the Figure 8. The designated points form the Moore neighborhood for a point with conductivity $g = 1.05$.

The values of the relative local conductivity obtained after filtration $g_{i,j,z,k}^{cor,flt}$ can be used to determine the instantaneous volumetric gas content according to Maxwell's rule:

$$\varepsilon_{i,j,z,k} = \frac{1 - g_{i,j,z,k}^{cor,flt}}{1 + 0.5 \cdot g_{i,j,z,k}^{cor,flt}}. \quad (8)$$

In Figure 9, an example of the gas bubble passage is depicted.

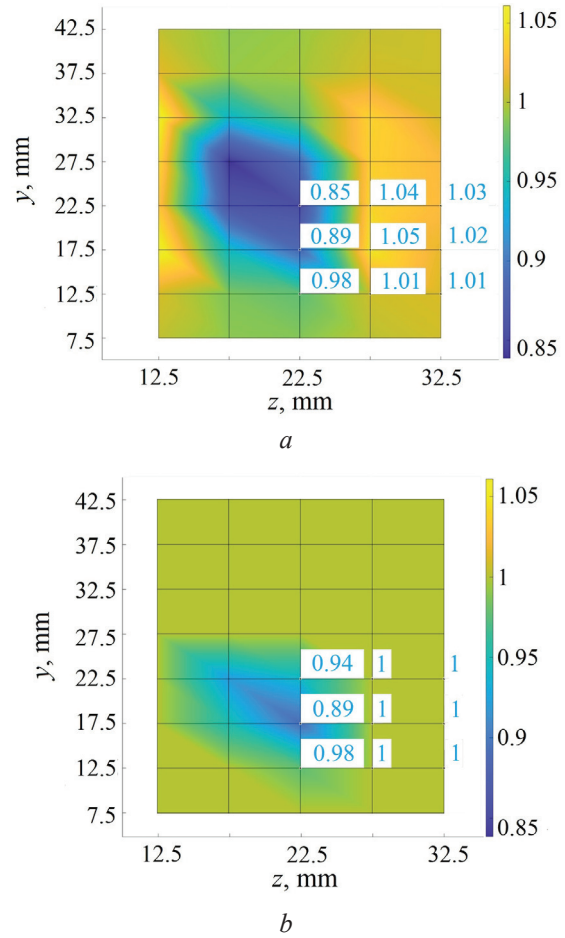


Figure 8 – Measured conductivity field before and after rebalancing and filtration (cell 27) in experiment N1: *a* – signal before rebalancing and filtering; *b* – signal after rebalancing and filtering

As mentioned above one of the practical applications of studying bubble flows is to determine the density of the interphase surface which is used in calculations to determine the interfacial heat and mass transfer.

Knowing the distribution of some scalar quantity $\phi(x, y, z, t)$, depending on the phase state of the medium, it's gradient magnitude will be written in the form:

$$a(x, y, z, t) = |\nabla\phi(x, y, z, t)| = \sqrt{\left(\frac{\partial\phi}{\partial x}\right)^2 + \left(\frac{\partial\phi}{\partial y}\right)^2 + \left(\frac{\partial\phi}{\partial z}\right)^2}. \quad (9)$$

Thus, the value is different from 0 along the interfacial surface, thereby its physical meaning can be interpreted as the "amount" of an interfacial surface area contained in a unit volume – the density of the interfacial surface. In this case, it's dimension

$$\text{is } \frac{m^2}{m^3} = \left[\frac{1}{L} \right].$$

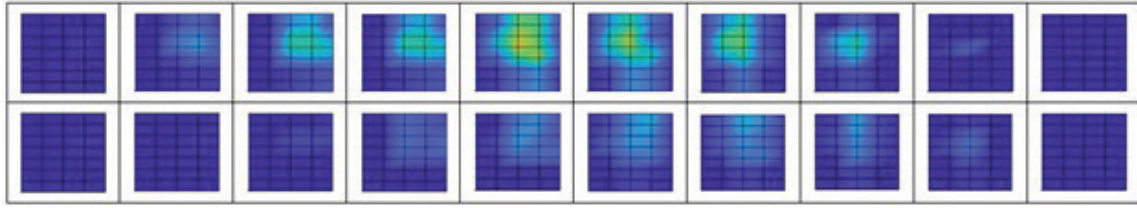


Figure 9 – Gas bubble passage: top row – layer 1; bottom row – layer 2 in experiment N1 (interval 8.2 ms). The vertical lines are generators wires, the horizontal – the receiver electrodes

Replacing ϕ the relative electrical conductivity of the medium g also depends on the phase state of the medium for the volumetric gas content conductometric sensor and can be written as:

$$\varepsilon_{i,j,z,k} = \frac{1}{\Delta x \Delta y \Delta z \Delta t} \int_x^{x+\Delta x} \int_y^{y+\Delta y} \int_z^{z+\Delta z} \int_t^{t+\Delta t} g(x, y, z, t) dx dy dz dt, \quad (10)$$

$$\lim_{\substack{\Delta x \rightarrow 0 \\ \Delta y \rightarrow 0 \\ \Delta z \rightarrow 0 \\ \Delta t \rightarrow 0}} \left| \nabla \varepsilon_{i,j,z,k}^{ideal} \right| = \lim_{\substack{\Delta x \rightarrow 0 \\ \Delta y \rightarrow 0 \\ \Delta z \rightarrow 0 \\ \Delta t \rightarrow 0}} \left| \nabla \frac{1}{\Delta x \Delta y \Delta z \Delta t} \int_x^{x+\Delta x} \int_y^{y+\Delta y} \int_z^{z+\Delta z} \int_t^{t+\Delta t} g(x, y, z, t) dx dy dz dt \right| = |\nabla g(x, y, z, t)| = a(x, y, z, t). \quad (11)$$

In turn, for a real WMS with spatial and temporal sampling of indications, expressions (9) and (11) are converted to the form:

$$a_{i,j,k} = \sqrt{\left(\frac{\Delta \varepsilon_{i,j,z,k}}{\Delta x} \right)^2 + \left(\frac{\Delta \varepsilon_{i,j,z,k}}{\Delta y} \right)^2 + \left(\frac{\Delta \varepsilon_{i,j,z,k}}{\Delta z} \right)^2}. \quad (12)$$

The derivatives of the gas content $\frac{\Delta \varepsilon_{i,j,z,k}}{\Delta x}$,

used in expression (12) were calculated using finite difference schemes [11]:

$$\frac{\Delta \varepsilon_i}{\Delta x} = \frac{\varepsilon_{i+1} - \varepsilon_i}{\Delta x}, \quad (13)$$

$$\frac{\Delta \varepsilon_i}{\Delta x} = \frac{\varepsilon_{i+1} - \varepsilon_{i-1}}{2\Delta x}, \quad (14)$$

$$\frac{\Delta \varepsilon_i}{\Delta x} = \frac{-\varepsilon_{i+1} + 8\varepsilon_{i+1} - 8\varepsilon_{i-1} + \varepsilon_{i-2}}{12\Delta x}, \quad (15)$$

where x is direction along the considered coordinate axis.

Scheme (13) was used to calculate the derivatives in the extreme cells of the WMS in X and Y as well as in the axial flow direction (along Z) since the design of the used two-layer WMS assumes the presence of only two measuring planes in the Z direction. Scheme (14) was used to calculate the derivatives

where Δx , Δy , Δz are the distance between the measuring cell in the directions of X , Y and Z respectively, m; Δt is time step, s.

Now, using expression (10) we express a through the distribution ε . For an ideal conductometric sensor (no space-time sampling):

with respect to X and Y in the cells preceding the boundary cells. Scheme (15) for calculating the derivatives with respect to X and Y in the central cells.

The experiments showed that when calculating $a_{i,j,k}$ according to expression (12), it is more expedient to use the values of the volumetric gas content $\varepsilon_{i,j,z,k}$, calculated from the first layer of measuring cells (z equal to the position of the first layer), since when the bubble collides with the electrodes, it deforms and breaks (Figure 10), which introduces a certain error in the values $\varepsilon_{i,j,z,k}$, recorded by the second layer of cells.

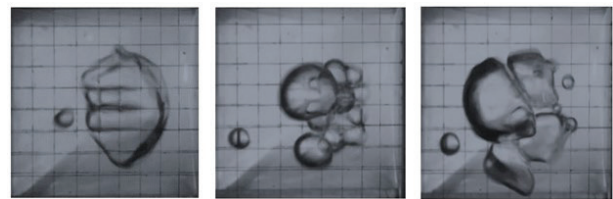


Figure 10 – Crushing and reorganization of a gas bubble passing through the wire mesh sensor

In verification practice, it is more convenient to link density interfacial surface with the observed parameters. Since a has a dimension $\left[\frac{1}{L} \right]$ it is possible to express the area of the bubble surface equivalent to the gas content in the cell:

$$A_{i,j,k} = a_{i,j,z,k} \cdot \Delta x \Delta y [w_{bub} \cdot \Delta t], \quad (16)$$

where w_{bub} – the velocity of bubbles, m/s.

Then the total bubble surface area will be equal to the sum of the areas determined for each sensor cell during the bubble passage:

$$A_{bub} = \sum_{i,j,k} a_{i,j,z,k} \cdot \Delta x \Delta y [w_{bub} \cdot \Delta t]. \quad (17)$$

In expressions (16) and (17) the distance $[w_{bub} \cdot \Delta t]$ is used instead of the cell height Δz . This is due to the fact that the unit volume occupied by the bubble at a given time is not equal to the total volume of the cell $\Delta x \Delta y \Delta z$. The velocity of a single bubble was determined from the time difference between the positions of the gas content maxima determined from the first and second layers of the WMS:

$$w_{bub} = \frac{\Delta z}{\left| k_1^{\max(\varepsilon)} - k_2^{\max(\varepsilon)} \right| \cdot \Delta t}, \quad (18)$$

where k is the number of the reference of the temporary implementation.

In the general case in the process of bubble emerging a sufficiently large bubbles undergo deformation caused by the presence of frontal resistance as well as by the formation of a vortex street behind it. The formation of a vortex wake during the movement of a gas bubble is illustrated in Figure 11.



Figure 11 – The velocity field of a bubble with a diameter of 5 mm [12]

However, the volume of the bubble V_{bub} can be expressed in terms of the radius of the equivalent spherical bubble:

$$V_{bub} = \frac{4}{3} \pi \left(R_{bub}^{eq} \right)^3. \quad (19)$$

Expressing R_{bub}^{eq} through A_{bub} and substituting in (19), we get:

$$V_{bub} = \frac{4}{3} \pi \left(\sqrt{\frac{A_{bub}}{4\pi}} \right)^3. \quad (20)$$

The summation of the obtained bubble volumes over all the bubbles recorded during the measurement period makes it possible to compare the gas volume determined from the WMS readings with the total gas volume introduced into the model (obtained from the readings of the injection system instrumentation).

Analysis of the obtained results

As a result of the experimental data analyses estimates of the velocities volumes and equivalent radii of gas bubbles were obtained. For convenience the data obtained are summarized in Table 2.

The design of the mesh sensor does not allow to record the immediate moment of the bubble passing through the measuring plane – in experiments, the area of the video camera is located up to the mesh sensor. As a result the bubble velocity was estimated as the average value over all injected bubbles. A storyboard for filming a single bubble ascent is shown in Figure 12.

The velocities obtained using expression (18) are consistent with the data of the video camera. Deviations about 17 % can be explained by the uncertainty in the measurement of a wire axial distance.

Table 2

Summary table of experimental research results

No	Average ascent rate of a single bubble (WMS), m/s	Average ascent rate of a single bubble (chamber), m/s	Average volume of a single bubble by (20), ml	Average volume of a single bubble according to instrumentation, ml	Total volume of injected gas (WMS), ml
1	0.31	0.27	1.51	1.80	7.575
2	0.33	0.27	1.50	1.80	7.482
3	0.33	0.29	1.45	1.80	7.251

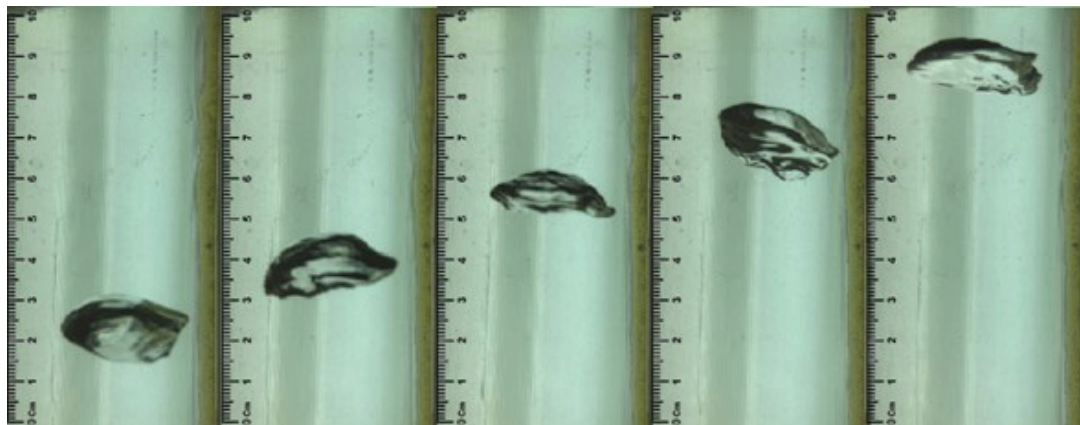


Figure 12 – The emergence of a single bubble (interval 0.05 s)

At the same time the values of the total gas volume passed through the WMS, are 15–20 % lower than the values for the instrumentation. In general an underestimation of the gas volume indicates an underestimation of the gas content in the section of the WMS. An analysis of the frame samples based on the WMS data shows that in most cases large gas bubbles when passing through the mesh sensor touch the area near the channel wall where the registration of the conductivity is not carried out (due to the construction of the WMS) which can also be the reason for underestimating of the total gas volume.

In addition low spatial resolution of the WMS (in those cases when the ratio R_{bub}/Δ , $\Delta = \Delta x = \Delta y$, where R_{bub} – the radius of the bubble in the cross section is less than a certain value which is a criteria for the given task) increases imprecision in the determination of the derivatives gas content (13)–(15) which affects by the value of the density of the interface (12).

Conclusion

Analysis of the experimental data made it possible to reveal the formation of the excess conductivity during the passage of a gas bubble caused by a violation of the symmetry of the electromagnetic field of the measuring cell due to a significant difference in the conductivity of the liquid and gas phases at the moment when the gas bubble does not completely occupy the cell. The method of conductivity rebalancing used in the analysis of experimental data made it possible to reduce the influence of this phenomenon on the calculated values of the gas content. In view of the

fact that the formation of the conductivity overshoot is actually caused by the influence of a complex set of sensor cells the improvement of methods aimed at eliminating these overshoots is an urgent task for further research in this area and can be associated, in particular with the use of approximation algorithms based on convolutional neural networks well adapted to work with data in matrix form.

As a result of applying the method of rebalancing conductivities to the experimental data, the values of the true volumetric gas content in the measuring cells of a two-layer mesh sensor were obtained. In addition the velocity of single bubble was estimated from the wire mesh sensor data and video camera recording.

The obtained values were used to determine the values of the interfacial areas, as well as the volumes of single bubbles by the gradient method, which made it possible to compare the balance values of the gas flow rate according to the readings of mesh sensors and test facility instrumentation.

References

1. Kataoka I., Ishii M., Serizawa A. Local formulation and measurements of interfacial area concentration in two-phase flow. *International Journal of Multiphase Flow*, 1986, vol. 12, pp. 505–529. DOI: 10.1016/0301-9322(86)90057-1
2. Hibiki T., Ishii M. Two-group interfacial area transport equations at bubbly-to-slug flow transition. *Nuclear Engineering and Design*, 2000, vol. 202, pp. 39–76. DOI: 10.1016/S0029-5493(00)00286-7
3. Dmitriev S.M., Barinov A.A., Dobrov A.A., Doronkov D.V., Pronin A.N., Ryazanov A.V., Solncev D.N., Sorokin V.D., Khrobostov A.E. [Experimental Studies of Turbulent Coolant Mixing in the Main

Equipment of Nuclear Units]. *VANT. Seriya: Yaderno-reaktornie konstanti* [VANT. Series: Nuclear reactor constants], 2018, no. 3, pp. 3–11 (in Russian).

4. Prasser H.M., Kleim S. Coolant mixing experiments in the upper plenum of the ROCOM test facility. *Nuclear Engineering and Design*, 2014, vol. 276, pp. 30–42. **DOI:** 10.1016/j.nucengdes.2014.05.016

5. Prasser H.M., Bottger A., Zschau J. A new electrode-mesh tomograph for gas-liquid flows. *Flow Measurement and Instrumentation*, 1998, vol. 9, pp. 111–119. **DOI:** 10.1016/S0955-5986(98)00015-6

6. Khrobostov A.E., Legchanov M.A., Solncev D.N., Barinov A.A., Konovalov I.A., Chesnokov A.A., Makarov M.A. [Research of Hydrodynamics of Stratified Turbulent Flows for Validation of Designated Approaches to Modeling Thermal Processes in Equipment of Nuclear Power Plants]. *Trudi NGTU im. R.E. Alekseeva* [Transactions of NNSTU n.a. R.E. Alekseev], 2019, vol. 126, no. 3, pp. 111–119 (in Russian).

7. Waite B.M., Prasser H.M., Podowski M.Z. Computational and Experimental Analysis of Gas/Liquid Two-Phase Flow in Rod Bundles with Mixing-Vane Spacer Grids. *Nuclear Engineering and Design*, 2020, vol. 360, pp. 1–42. **DOI:** 10.1016/j.nucengdes.2019.110499

8. Prasser H.M., Matthias B., Dirk L. Improvement of Topflow Void Fraction Data Using Potential Field Simulation of the Wire-Mesh Sensor. *Specialists Workshop on Advanced Instrumentation and Measurement Techniques for Experiments related to Nuclear Reactor Thermal Hydraulics and Severe Accidents*, 2019, vol. 35, pp. 1–16.

9. Beyer M., Lucas D., Kussin J. Quality check of wire-mesh sensor measurements in a vertical air/water flow. *Flow Measurement and Instrumentation*, 2010, vol. 21, pp. 511–520.

DOI: 10.1016/j.flowmeasinst.2010.09.001

10. Tompkins C., Prasser H.M., Corradini M. Wire-mesh sensors: A review of methods and uncertainty in multiphase flows relative to other measurement techniques. *Nuclear Engineering and Design*, 2018, vol. 337, pp. 205–220. **DOI:** 10.1016/j.nucengdes.2018.06.005

11. Prasser H.M., Stucki S., Betschart T., Eisenberg J. Interfacial area density measurement using a three-layer wire-mesh sensor. *NURETH-16*, 2015, pp. 403–418.

12. Clift R., Grace J.R., Weber M.E. *Bubbles, drops and particles*. London: *Academic Press*, 1978, vol. 94, 380 p.

Determination of the Error in Transferring of Length Unit's Size when Measuring the Nanoparticles' Diameter Using an Analyzer of Particles' Differential Electrical Mobility

V.L. Solomakho¹, A.A. Bagdun²

¹Belarusian National Technical University,
Nezavisimosti Ave., 65, Minsk 220013, Belarus

²Belarusian State Institute of Metrology,
Starovilensky trakt, 93, Minsk 220053, Belarus

Received 09.07.2021

Accepted for publication 01.09.2021

Abstract

The quality of nanomaterials and nanotechnologies is largely determined by the stability of the applied technologies, which, to a large extent, depend on the constancy of particle sizes. In this regard, metrological problems arise that are associated both with measuring the dimensions of the microstructure of aerosols, suspensions and powders, and with ensuring the uniformity of measurements when transferring a unit of a physical quantity from a standard to working measuring instruments. The purpose of this work was to determine and calculate the error in transferring the size of a unit of length when measuring the diameter of nanoparticles.

An analyzer of differential electric mobility of particles was determined as a reference measuring instrument for which the calculation was made. It allows the separation of aerosol particles based on the dependence of their electrical mobility on the particle size. In combination with a condensation particle counter, it allows you to scan an aerosol and build a particle size distribution function. This measurement method is the most accurate in the field of measuring the diameters of particles in aerosols, therefore, the error in the transmission of particle size must be set as for a standard.

The paper describes the physical principles of measurement by this method and presents an equation for determining the diameter of nanoparticles. Based on this equation, the sources of non-excluded systematic error were identified. Also, an experimental method was used to determine the random component of the measurement error of nanoparticles and to calculate the error in transferring the size of a unit of length when measuring the diameter of nanoparticles.

The obtained results will be used for metrological support of standard samples of particle size, ensuring traceability of measurements of aerosol particle counters and for aerosol research.

Keywords: nanoparticles, electrical mobility, traceability of measurements, diameter of nanoparticles.

DOI: 10.21122/2220-9506-2021-12-3-194-201

Адрес для переписки:

Багдюн А.А.
Белорусский государственный институт метрологии,
Старовиленский тракт, 93, г. Минск 220053, Беларусь
e-mail: bagdun.ne@gmail.com

Address for correspondence:

Bagdun A.A.
Belarusian State Institute of Metrology,
Starovilensky trakt, 93, Minsk 220053, Belarus
e-mail: bagdun.ne@gmail.com

Для цитирования:

V.L. Solomakho, A.A. Bagdun.
Determination of the Error in Transferring of Length Unit's Size when Measuring the Nanoparticles' Diameter Using an Analyzer of Particles' Differential Electrical Mobility.
Приборы и методы измерений.
2021. – Т. 12, № 3. – С. 194–201.
DOI: 10.21122/2220-9506-2021-12-3-194-201

For citation:

V.L. Solomakho, A.A. Bagdun.
Determination of the Error in Transferring of Length Unit's Size when Measuring the Nanoparticles' Diameter Using an Analyzer of Particles' Differential Electrical Mobility.
Devices and Methods of Measurements.
2021, vol. 12, no. 3, pp. 194–201.
DOI: 10.21122/2220-9506-2021-12-3-194-201

Определение погрешности передачи размера единицы длины при измерении диаметра наночастиц с помощью анализатора дифференциальной электрической подвижности частиц

В.Л. Соломахо¹, А.А. Багдюн²

¹Белорусский национальный технический университет,
пр-т Независимости, 65, г. Минск 220013, Беларусь

²Белорусский государственный институт метрологии
Старовиленский тракт, 93, г. Минск 220053, Беларусь

Поступила 09.07.2021

Принята к печати 01.09.2021

Качество наноматериалов и нанотехнологий во многом определяется стабильностью применяемых технологий, которые в значительной степени зависят от постоянства размеров частиц. В связи с этим возникают метрологические задачи, связанные как собственно с измерением размеров микроструктуры аэрозолей, суспензий и порошков, так и с обеспечением единства измерений при передаче единицы физической величины от эталонного к рабочим средствам измерений. Целью данной работы являлось определение и расчёт погрешности передачи размера единицы длины при измерении диаметра наночастиц.

В качестве эталонного средства измерения, для которого производился расчёт, был определён анализатор дифференциальной электрической подвижности частиц. Он позволяет разделять частицы аэрозоля на основе зависимости их электрической подвижности от размера частиц. В комбинации с конденсационным счётчиком частиц позволяет сканировать аэрозоль и строить функцию распределения частиц по размерам. Данный метод измерения является самым точным в области измерения диаметров частиц в аэрозолях, поэтому погрешность передачи размера частиц необходимо установить как для эталона.

В работе описаны физические принципы измерения данным методом и представлено уравнение для определения диаметра наночастиц. На основании данного уравнения были определены источники неисключённой систематической погрешности. Также экспериментальным методом определена случайная составляющая погрешности измерения наночастиц и рассчитана погрешность передачи размера единицы длины при измерении диаметра наночастиц.

Полученные результаты будут использованы для метрологического обеспечения стандартных образцов размера частиц, обеспечения прослеживаемости измерений счётчиков аэрозольных частиц и для исследований аэрозолей.

Ключевые слова: наночастицы, электрическая подвижность, прослеживаемость измерений, диаметр наночастиц.

DOI: 10.21122/2220-9506-2021-12-3-194-201

Адрес для переписки:

Багдюн А.А.
Белорусский государственный институт метрологии,
Старовиленский тракт, 93, г. Минск 220053, Беларусь
e-mail: bagdun.ne@gmail.com

Address for correspondence:

Bagdun A.A.
Belarusian State Institute of Metrology,
Starovilensky trakt, 93, Minsk 220053, Belarus
e-mail: bagdun.ne@gmail.com

Для цитирования:

V.L. Solomakho, A.A. Bagdun.
Determination of the Error in Transferring of Length Unit's Size when Measuring the Nanoparticles' Diameter Using an Analyzer of Particles' Differential Electrical Mobility.
Приборы и методы измерений.
2021. – Т. 12, № 3. – С. 194–201.
DOI: 10.21122/2220-9506-2021-12-3-194-201

For citation:

V.L. Solomakho, A.A. Bagdun.
Determination of the Error in Transferring of Length Unit's Size when Measuring the Nanoparticles' Diameter Using an Analyzer of Particles' Differential Electrical Mobility.
Devices and Methods of Measurements.
2021, vol. 12, no. 3, pp. 194–201.
DOI: 10.21122/2220-9506-2021-12-3-194-201

Introduction

Nanoparticles and nanotechnology are one of the most promising areas of scientific development at the present stage, creating preconditions for solving various applied technological problems. All over the world, a huge number of “nanoproducts” are being developed, based on the use of nanoparticles, which make it possible to obtain new quality products and technologies [1].

Nanostructured (nanophase, nanocrystalline, subpre-molecular) materials traditionally include materials with microstructure sizes from 1 to 100 μm . This definition of dimensional boundaries is not accidental. The lower limit is associated with the loss of some symmetry elements in crystals of nanocrystalline materials as their size decreases. The value of the upper limit is due to the fact that noticeable “useful”, from a technical point of view, changes in the physicomechanical, chemical, electrical, optical, tribological and other properties of materials sharply decrease with a further increase in the particle size [2, 3].

Currently, the priority interest in the development of nanomaterials and nanotechnology is due to [4, 5]:

- using the unique properties of materials in a nanostructured state;
- development of technologies for obtaining nanoclusters and nanostructures;
- the need to develop and implement new materials with qualitatively new properties;
- the desire for miniaturization of products;
- the practical implementation of modern methods and means of control, including nano-objects and nanomaterials, etc.

The quality of products is determined by the stability of technologies, which, in relation to nanotechnology, largely depend on the constancy of particle sizes. Among the characteristics defined by the Organization for Economic Cooperation and Development, the determination of particle size is determined by the most important element in the study of the properties of nanoparticles.

Therefore, the harmonization of methods for measuring the size of nanoparticles is extremely demanded, firstly, to ensure the continuous development of nanotechnology and support trade in nanoproducts, and secondly, to assess the potential danger of their impact on the environment, health and safety of human life [6]. Under these conditions, it is very important to ensure the metrological

traceability of measurements of nanoparticles, including the creation of the necessary reference means of changes.

There are various methods for measuring linear quantities in this size range. In particular, the standard ISO/AWI 15900 “Determination of particle size distribution. Differential analysis of the electrical mobility of particles in aerosols” provides that the measurement of particle sizes in the analysis of the disperse composition of gaseous media is carried out using a differential particle mobility analyzer (DMA).

Physical principles of measuring particle diameters by electrical mobility

This method is based on the physical principle of differential electrical mobility analysis, which separates aerosol particles based on the dependence of their electrical mobility on particle size. The electric mobility of a particle Z is equal to the velocity U of a charged particle divided by the strength of the electric fields E :

$$Z = \frac{U}{E}. \quad (1)$$

Electric mobility is calculated from the balance of electric forces arising from the charge on the particle and the resistance force determined by Stokes' law:

$$neE = \frac{3\pi\mu UD_p}{C(D_p)}, \quad (2)$$

where n is the number of charges; e is the electron charge; μ is the viscosity of the gas; D_p is the particle diameter; $C(D_p)$ is Cunningham slip correction.

The charge distribution on particles depending on their size is based on a theoretical model arising from the theory of diffusion for particles of the submicron range, based on the Fuchs approximation.

Figure 1 shows curves calculated according to Fuchs theory, where $f_N(d)$ is the particle charge; d is the particle size.

The size distribution of particles carrying zero, one or two elementary charges at an equilibrium charge is expressed by the equation derived from the Fuchs model:

$$f_N(d) = 10^{\sum a_i(N)(\log d)^i}, \quad (3)$$

where the particle size d is expressed in nm, the values of the coefficient $a_i(N)$ were determined using least squares analysis and are indicated in Table 1 [7].

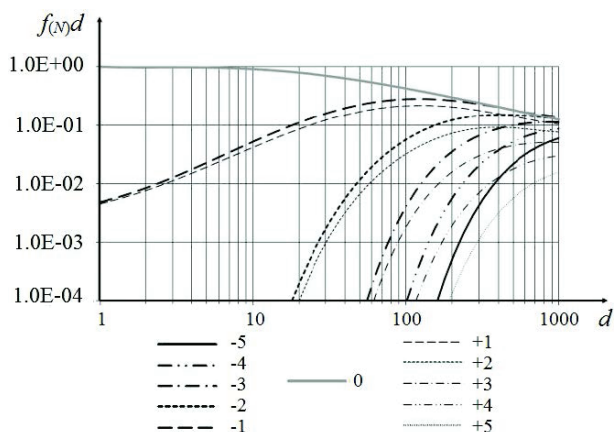


Figure 1 – Charge distribution function for particles in the size range between 1 and 1000 nm, where the numbers denoting the curve are the number of elementary charges carried by the particle

Table 1

Coefficients $a_i(N)$ for formula (3) for a bipolar charge conditioner with a 9.5 kV X-ray ion source

i	$a_i(N)$				
	$N = -2$	$N = -1$	$N = 0$	$N = 1$	$N = 2$
0	-30.616	-2.335	0.002	-2.359	-27.253
1	46.339	0.436	-0.114	0.452	38.480
2	-31.182	1.087	0.334	0.998	-24.271
3	11.391	-0.557	-0.357	-0.482	8.442
4	-2.220	0.050	0.108	0.026	-1.606
5	0.179	0.006	-0.011	0.008	0.129

Equation (3) is valid for a range of particle sizes:
 $1 \text{ nm} \leq d \leq 1000 \text{ nm}$ for $N = (-1; 0; 1)$;
 $20 \text{ nm} \leq d \leq 1000 \text{ nm}$ for $N = (-2; 2)$.

The size distribution of particles carrying three or more elementary charges is calculated by the formula:

$$f_N(d) = \frac{e}{\sqrt{4\pi\epsilon_0 dkT}} \exp \left\{ \frac{-[N - (2\pi dkT)/e^2]}{2[(2\pi dkT)/e^2]} \ln(Z_{+i}/Z_{-i}) \right\},$$

where ϵ_0 is the dielectric constant of the gas (for air $\epsilon_0 = 1.602 \cdot 10^{-12} \text{ F/m}$); k is the Boltzmann constant; T is the gas temperature; Z_{+i}/Z_{-i} is ratio of ion mobility.

Coefficient $C(D_p)$ tends to unity for a particle whose diameter is greater than its mean free path in gas, and increases with decreasing particle diameter. In the case of singly charged particles, $n = 1$. Then the following expression for the electric mobility is derived from equations (1) and (2):

$$Z = \frac{eC(D_p)}{3\pi\mu D_p}.$$

Electrostatic classifier device

The electrostatic classifier, which includes the DMA, is structured as follows (Figure 2).

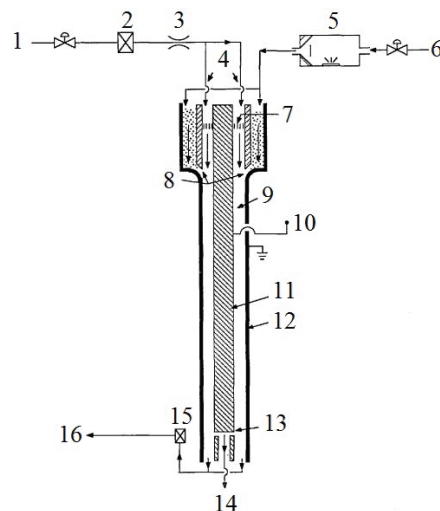


Figure 2 – Schematic representation of the cylindrical classifier: 1 – blowing air supply channel (q_{sh}); 2 – high efficiency particulate air filter; 3 – flow meter; 4 – channel of clean air; 5 – aerosol neutralizer; 6 – channel for supplying polydisperse aerosol; 7 – flow straightener; 8 – aerosol inlet; 9 – classification area; 10 – high voltage source; 11 – central rod (r_1), which is supplied with high voltage (V); 12 – outer cylinder (r_2); 13 – exit slit of monodisperse aerosol; 14 – channel for the exit of monodisperse aerosol; 15 – filter; 16 – channel for the exit of polydisperse aerosol

This device allows you to separate aerosol particles based on their electrical mobility and, accordingly, create a stream of monodisperse particles at the outlet.

The classifier contains a bipolar charger (aerosol neutralizer). Here, the particles collide with bipolar ions, which leads to an equilibrium charge distribution that depends on the particle size. For example, according to diffusion theory for submicron particles, 100 nm particles will definitely exit the bipolar charger with 42.6 % uncharged particles; 24.1 % with +1 charge; 24.1 % with a charge of -1; and the remaining particles are multiply charged.

After passing through the bipolar charger, the aerosol enters the DMA, also located inside the classifier. The DMA is a long cylindrical chamber with a radius of 1.958 cm. Inside the chamber there is a rod with a radius of 0.937 cm, concentric with the walls of the chamber, so that an annular space is formed between the rod and the walls of the chamber.

The aerosol stream enters the upper part of the chamber and is combined with a stream of clean blowing air. The combined flow flows into the gap between the coaxially located central rod and the outer cylinder. The voltage on the rod can be adjusted from 0 to 10.000 V. The outer cylindrical chamber is supported by ground potential, which allows the electric field to spread evenly in the annular space to the bottom of the chamber. Along the way, charged particles move to the central rod due to the voltage potential difference.

By changing the voltage on the central rod, thereby scanning the electric field strength, and by measuring the numerical concentration of the aerosol coming out of the slit, the distribution of the electric mobility of the particles is determined.

The small radial clearance and high uniformity of the electric field create the necessary conditions for high-resolution electrical mobility measurements.

A small gap in the rod allows you to classify particles with electrical mobility Z , calculated using the following formula:

$$Z = \frac{q_{sh}}{2\pi VL} \ln\left(\frac{r_2}{r_1}\right), \quad (5)$$

where q_{sh} is the blowing air flow rate in the shell; V is the voltage on the rod; L is the length from the aerosol inlet to the slot; r_1 and r_2 are the inner and outer radii of the annular space, respectively.

By adjusting the voltage, particles with a narrow range of mobility are selected. The yield of nearly monosized particles is achieved by selecting particles based on their mobility. A stream of monosized particles passes through the rod hole and exits the classifier, then to the condensation particle counter, where the number of particles is counted. The rest of the stream leaves the classifier through an excess stream outlet and enters the recirculation system. The recirculation system pumps casing air through the classifier, draws out excess air and then conditions it before returning it as a casing air stream.

From equations (4) and (5), the particle diameter is equal to:

$$D_p = \frac{eC(D_p)2VL}{q_{sh}3\mu \ln\left(\frac{r_2}{r_1}\right)}. \quad (6)$$

Determination of sources of non-excluded systematic error

Based on equation (6), a model was built for calculating the main sources of non-excluded

systematic errors when measuring the diameter of particles in air using DMA:

$$\theta_L = f(\delta e, \delta \mu, \delta C(D_p), \delta(L, r_1, r_2), \delta V, \delta q_{sh}),$$

where δe is the error due to the determination of the magnitude of the electron charge; $\delta \mu$ is the error due to the determination of the value of the gas viscosity; $\delta C(D_p)$ error due to the determination of the Cunningham correction factor; $\delta(L, r_1, r_2)$ the error caused by the measurement of the geometric parameters of the DMA; δV is the error due to the voltage measurement on the central rod of the DMA; δq_{sh} is the error due to the measurement of the blowing air flow rate in the DMA casing.

Quantification of the main sources of non-excluded systematic measurement error

The error due to the determination of the magnitude of the electron charge

The magnitude of the electron charge and its standard deviation (1σ) are equal to $(1.6021892 \pm 0.0000046) \cdot 10^{-19}$ C. The relative error is about $3 \cdot 10^{-4}$ % and is negligible when estimating the boundaries of the non-excluded systematic error.

Error due to the determination of the gas viscosity

R.T. Birge established a weighted average of the viscosity of dry air at 23.00 °C equal to $\mu_0 = (1.83245 \pm 0.00069) \cdot 10^{-5}$ kg m⁻¹ s⁻¹, corrected for temperature using the Sutherland equation. After determining the reference viscosity at 23.00 °C, the viscosity for other temperatures can be obtained using the Sutherland formula:

$$\mu = \mu_0 \left(\frac{T}{T_0}\right)^{1.5} \left(\frac{T_0 + 110.4K}{T + 110.4K}\right),$$

where T_0 is the absolute reference temperature (296.15 K); T is the absolute temperature.

The viscosity of dry air at 23.00 °C has a relative error of 0.038 %. The air flowing through the DMA has an estimated relative humidity of 7 %. The reduction in viscosity due to the addition of water is estimated at 0.08 % based on the viscosity of the water and its air volume fraction. This value of 0.08 % is taken as the relative error in determining the viscosity of air due to the presence of water vapor. Calculating the relative error in determining

the viscosity of a gas as a root of the sum of squares, we get a value of 0.089 %.

Error due to the determination of the Cunningham correction factor (slip correction)

The slip correction extends the calculation based on the Stokes law of the retarding force acting on a spherical particle moving with a low Reynolds number in a gas medium to particles of the order of a nanometer.

The Cunningham slip correction factor, which describes the behavior of a gas in an inhomogeneous medium when small particles move, is determined by the expression:

$$C(D_p) = 1 + K_n \left[A_1 + A_2 \exp\left(-\frac{A_3}{K_n}\right) \right] = 1 + K_n A,$$

where K_n is the Knudsen number, namely, the doubled free path of particles in air divided by the particle diameter ($K_n = 2\lambda/D_p$); A_1, A_2, A_3 dimensionless constants; A is slip correction parameter. The error due to the determination of the Cunningham correction factor is taken to be 0.1 %, which corresponds to the type A uncertainty from the study [8].

Error due to geometric parameters measurement of the DMA

The error caused by the measurement of the geometric parameters of the DMA includes the errors in measuring the length from the aerosol inlet to the slit (analyzer length L), the inner and outer radii of the annular space (r_1, r_2). The listed errors are 0.5 %, 0.1 % and 0.6 %, respectively [9]. Calculating the error due to the measurement of the geometric parameters of the DMA as the root of the sum of squares, we get a value of 0.7 %.

Error due to voltage measurement on the center rod of the DMA

The error due to voltage measurement on the central rod of the DMA is indicated in the calibration certificate for the electrostatic classifier and is 0.3 %.

The error due to the measurement of the blowing air flow rate in the sheath of the DMA

The error due to the measurement of the blowing air flow rate in the DMA casing is specified in the calibration certificate for the electrostatic classifier and is 2.0 %.

The main sources of non-excluded systematic errors and their values are shown in Table 2.

Table 2

Sources of non-excluded systematic errors

Error name	Source of non-excluded systematic errors	Error value θ_i , %
δe	Error due to the determination of the magnitude of the electron charge e	0.0003
$\delta \mu$	Error due to the determination of the value of the viscosity of the gas μ	0.089
$\delta C(D_p)$	Error due to the determination of the Cunningham correction factor $C(D_p)$	0.1
$\delta(L, r_1, r_2)$	Error due to the measurement of the geometric parameters of the DMA (L, r_1, r_2)	0.79
δV	Error due to measuring voltage V at the center rod of the DMA	0.3
δq_{sh}	Error due to the measurement of the air flow velocity q_{sh} in the DMA shell	2.0
Non-excluded systematic error θ_L		
$\theta_L = K \sqrt{\sum \theta_i^2}$		1.1 × 2.18
Note: a confidence interval $P = 0.95$; $K = 1.1$		
Non-excluded systematic error θ_L		2.4

Determination of the standard deviation of the random component of the analyzer error when measuring the size of nanoparticles in air

The standard deviation of the random component of the analyzer error in measuring the particle size in air was determined from standard samples of PSL particle size with a nominal value of 100 nm. This particle size is typical and is used to represent the accuracy characteristics of nanoparticle measuring instruments.

The standard deviation of the random error component S_L , %, is calculated by the formula:

$$S_L = \frac{\sqrt{\frac{\sum (L_i - \bar{L})^2}{n(n-1)}}}{\bar{L}} \cdot 100\%,$$

where L_i is the result of the i -th observation, nm; \bar{L} is arithmetic mean of observation results, nm; n is the number of observations.

The number of observations at each investigated point of the measurement range n is determined by the formula:

$$n = \frac{2}{1-p}, \quad (7)$$

where p is the confidence level (at $p = 0.95$, $n = 40$).

Since the random component of the error is taken into account, and there is no variation, the number of observations calculated by formula (7) can be reduced to $n = 10$.

Example of protocol of measurement results obtained in the *Aerosol Instrument Manager* software is shown in Figure 3.

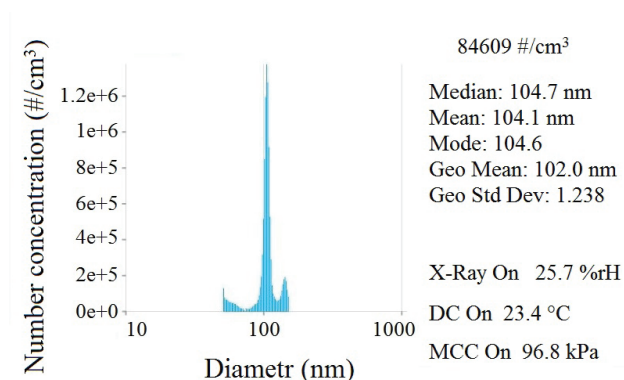


Figure 3 – Example of protocol for the measurement results of nanoparticles with a nominal diameter of 100 nm

The protocol displays the particle size distribution function in the range from 50 to 150 nm. The median, mode, arithmetic mean, geometric mean and standard deviation of the geometric mean of the distribution function were also calculated.

We take the geometric mean value for the observation result.

The standard deviation of the random component of the error S_L is 0.33 %.

Determination of the error in transferring the size of a unit of length when measuring the size of nanoparticles in air

The error in transferring the size of a unit of

$$S_{\Sigma} = \sqrt{S_L^2 + \theta_L^2}.$$

length when measuring the size of nanoparticles in air S_{Σ} , nm, is determined by the formula:

It is 2.42 % with a confidence level of $P = 0.95$; $K = 1.1$.

Conclusion

The error in transferring the size of a unit of length when measuring the size of nanoparticles in air was 2.42 % with a confidence level of $P = 0.95$; $K = 1.1$. This value of the error makes it possible to calibrate the counters of aerosol particles without resorting to purchasing standard samples of monodisperse latexes. Moreover, based on the results obtained, certification of standard samples of particle size in aerosols will be carried out. Also, the fact that the value of the error in transferring the size of a unit of length when measuring the diameter of nanoparticles was established by this method, and not using a comparison standard, allows us to assert that the analyzer of differential mobility of particles not only stores and transmits a unit of size, but also reproduces it.

References

1. Lux Research. Sizing Nanotechnology's Value Chain, 2004.
2. Gleiter H. Nanostructured materials: basic concepts and microstructure. *Actamater*, 2000, vol. 48, pp. 1–29. DOI: 10.1016/S1359-6454(99)00285-2
3. Alymov M.I. Mechanical properties of nanocrystalline materials. Moscow: MIFI Publ., 2004, 32 p. DOI: 10.17277/amt.2017.02pp.010-018

4. Glezer A.M. Amorphous and nanocrystalline structures: similarities, differences, mutual transitions. *Russian Chemical Journal*, 2002, vol. XLVI, no. 5, pp. 57–63. **DOI:** 10.1134/S1087659612010038

5. Poole Ch., Owens F. Nanotechnology. Publishing house 5th. Moscow: Tekhnosfera Publ., 2010, 336 p.

6. NNI (National Nanotechnology Initiative) 2011, Environmental, Health, and Safety Strategy.

7. Tigges L., Wiedensohler A., Weinhold K., Gandhi J., Schmid H.-J. Bipolar charge distribution of a soft X-ray diffusion charger. *J. Aerosol Sci.*, 2015, vol. 90,

pp. 77–86.

DOI: 10.1016/J.JAEROSCI.2015.07.002

8. Kim J.H., Mulholland G.W., Kukuck S.R., Pui D.Y.H. Slip Correction Measurements of Certified PSL Nanoparticles Using a Nanometer Differential Mobility Analyzer (Nano-DMA) for Knudsen Number From 0.5 to 83. *J. Res. Natl. Inst. Stand. Technol.*, 2005, vol. 110, pp. 31–54. **DOI:** 10.6028/jres.110.005

9. ISO 15900:2020 Determination of particle size distribution – Differential electrical mobility analysis for aerosol particles.

Low-Frequency Admittance of Capacitor with Working Substance “Insulator–Partially Disordered Semiconductor–Insulator”

N.A. Poklonski, I.I. Anikeev, S.A. Vyrko

Belarusian State University,
Nezavisimosti Ave., 4, Minsk 220030, Belarus

Received 07.07.2021

Accepted for publication 03.09.2021

Abstract

The study of the electrophysical characteristics of crystalline semiconductors with structural defects is of practical interest in the development of radiation-resistant varactors. The capacitance-voltage characteristics of a disordered semiconductor can be used to determine the concentration of point defects in its crystal matrix. The purpose of this work is to calculate the low-frequency admittance of a capacitor with the working substance “insulator–crystalline semiconductor with point t -defects in charge states (–1), (0) and (+1)–insulator”.

A layer of a partially disordered semiconductor with a thickness of 150 μm is separated from the metal plates of the capacitor by insulating layers of polyimide with a thickness of 3 μm . The partially disordered semiconductor of the working substance of the capacitor can be, for example, a highly defective crystalline silicon containing point t -defects randomly (Poissonian) distributed over the crystal in charge states (–1), (0), and (+1), between which single electrons migrate in a hopping manner. It is assumed that the electron hops occur only from t -defects in the charge state (–1) to t -defects in the charge state (0) and from t -defects in the charge state (0) to t -defects in the charge state (+1).

In this work, for the first time, the averaging of the hopping diffusion coefficients over all probable electron hopping lengths via t -defects in the charge states (–1), (0) and (0), (+1) in the covalent crystal matrix was carried out. For such an element, the low-frequency admittance and phase shift angle between current and voltage as the functions on the voltage applied to the capacitor electrodes were calculated at the t -defect concentration of $3 \cdot 10^{19} \text{ cm}^{-3}$ for temperatures of 250, 300, and 350 K and at temperature of 300 K for the t -defect concentrations of $1 \cdot 10^{19}$, $3 \cdot 10^{19}$, and $1 \cdot 10^{20} \text{ cm}^{-3}$.

Keywords: partially disordered semiconductor, low-frequency admittance of capacitor, triple-charged intrinsic point defects.

DOI: 10.21122/2220-9506-2021-12-3-202-210

Адрес для переписки:

Поклонский Н.А.
Белорусский государственный университет,
пр-т Независимости, 4, г. Минск 220030, Беларусь
e-mail: poklonski@bsu.by; poklonski@tut.by

Address for correspondence:

Poklonski N.A.
Belarusian State University,
Nezavisimosti Ave., 4, Minsk 220030, Belarus
e-mail: poklonski@bsu.by; poklonski@tut.by

Для цитирования:

N.A. Poklonski, I.I. Anikeev, S.A. Vyrko.
Low-Frequency Admittance of Capacitor with Working Substance
“Insulator–Partially Disordered Semiconductor–Insulator”.
Приборы и методы измерений.
2021. – Т. 12, № 3. – С. 202–210.
DOI: 10.21122/2220-9506-2021-12-3-202-210

For citation:

N.A. Poklonski, I.I. Anikeev, S.A. Vyrko.
Low-Frequency Admittance of Capacitor with Working Substance
“Insulator–Partially Disordered Semiconductor–Insulator”.
Devices and Methods of Measurements.
2021, vol. 12, no. 3, pp. 202–210.
DOI: 10.21122/2220-9506-2021-12-3-202-210

Низкочастотный адмиттанс конденсатора с рабочим веществом «изолятор – частично разупорядоченный полупроводник – изолятор»

Н.А. Поклонский, И.И. Анисеев, С.А. Вырко

Белорусский государственный университет,
пр-т Независимости, 4, г. Минск 220030, Беларусь

Поступила 07.07.2021

Принята к печати 03.09.2021

Исследование электрофизических характеристик кристаллических полупроводников с дефектами структуры представляет практический интерес при создании радиационно-стойких варакторов. По вольт-фарадным характеристикам разупорядоченного полупроводника можно определять концентрацию точечных дефектов в его кристаллической матрице. Цель работы – рассчитать низкочастотный адмиттанс конденсатора с рабочим веществом «изолятор – кристаллический полупроводник с точечными t -дефектами в зарядовых состояниях (-1) , (0) и $(+1)$ – изолятор».

Слой частично разупорядоченного полупроводника толщиной 150 мкм отделен от металлических обкладок конденсатора диэлектрическими прослойками из полиимида толщиной 3 мкм. Частично разупорядоченный полупроводник рабочего вещества конденсатора представляет собой, например, сильнодефектный кристаллический кремний, содержащий точечные t -дефекты, случайно (пуассоновски) распределенные по кристаллу, в зарядовых состояниях (-1) , (0) и $(+1)$ между которыми прыжковым образом мигрируют одиночные электроны. Считается, что прыжки электронов происходят только с t -дефектов в зарядовом состоянии (-1) на t -дефекты в зарядовом состоянии (0) и с t -дефектов в зарядовом состоянии (0) на t -дефекты в зарядовом состоянии $(+1)$.

В работе впервые проведено усреднение коэффициентов прыжковой диффузии по всем вероятным длинам прыжка электрона между t -дефектами в зарядовых состояниях (-1) , (0) и (0) , $(+1)$ в ковалентной кристаллической матрице. Для такого элемента рассчитаны низкочастотный адмиттанс и угол сдвига фаз между током и напряжением в зависимости от приложенного на электроды конденсатора напряжения при концентрации t -дефектов $3 \cdot 10^{19} \text{ см}^{-3}$ для температур 250, 300 и 350 К и при температуре 300 К для концентраций t -дефектов $1 \cdot 10^{19}$, $3 \cdot 10^{19}$ и $1 \cdot 10^{20} \text{ см}^{-3}$.

Ключевые слова: частично разупорядоченный полупроводник, низкочастотный адмиттанс конденсатора, трехзарядные собственные точечные дефекты.

DOI: 10.21122/2220-9506-2021-12-3-202-210

Адрес для переписки:

Поклонский Н.А.
Белорусский государственный университет,
пр-т Независимости, 4, г. Минск 220030, Беларусь
e-mail: poklonski@bsu.by; poklonski@tut.by

Address for correspondence:

Poklonski N.A.
Belarusian State University,
Nezavisimosti Ave., 4, Minsk 220030, Belarus
e-mail: poklonski@bsu.by; poklonski@tut.by

Для цитирования:

N.A. Poklonski, I.I. Aniseev, S.A. Vyrko.
Low-Frequency Admittance of Capacitor with Working Substance
“Insulator–Partially Disordered Semiconductor–Insulator”.
Приборы и методы измерений.
2021. – Т. 12, № 3. – С. 202–210.
DOI: 10.21122/2220-9506-2021-12-3-202-210

For citation:

N.A. Poklonski, I.I. Aniseev, S.A. Vyrko.
Low-Frequency Admittance of Capacitor with Working Substance
“Insulator–Partially Disordered Semiconductor–Insulator”.
Devices and Methods of Measurements.
2021, vol. 12, no. 3, pp. 202–210.
DOI: 10.21122/2220-9506-2021-12-3-202-210

Introduction

In the works [1, 2], for the first time, a variant of controlling the hopping electrical conductivity via hydrogen-like donors along a semiconductor film using an external electrostatic field $E(x) = -d\phi/dx$ perpendicular to the film surface, which does not lead to the appearance of a current and does not violate the electrical neutrality of the film as a whole, was theoretically considered. However, the hopping electrical conductivity longitudinal to the direction of the controlling external electric field was not considered in [1, 2]. The field effect was studied and the quasi-frequency (low-frequency) capacitance and conductivity of silicon crystals with hopping electron migration via point two-level defects with positive and negative correlation energies in three charge states (–1), (0), and (+1) were calculated [3, 4]. However, the electrical capacity and conductivity of the “insulator–partially disordered semiconductor–insulator” structure were not investigated in [3, 4]. For the first time, the static capacitance–voltage characteristics of a ζ -diode made of crystalline silicon, in which current was carried only by electron hopping via t -defects, were calculated [5]. However, in the diode model constructed in [5], there was no averaging of diffusion coefficients over all probable electron hopping lengths via t -defects in three charge states (–1), (0), and (+1). Taking into account electron hopping via point defects, the temperature and frequency dependences of the dielectric permittivity of silicon irradiated with a large dose of neutrons were studied [6]. The low-frequency electrical capacitance as well as the electric field and potential distribution for the “metal–insulator–intrinsic semiconductor–insulator–metal” structure were calculated [7–9]. However, the capacitance–voltage characteristics for the structure with a disordered semiconductor layer were not calculated in [7–9]. The results of an experiment on measuring the capacitance of a thin-film capacitor (structure Al–Al₂O₃–Al) were interpreted [10] taking into account quantum effects. A method was described [11, 12] for determining, from the temperature dependences of capacitance and conductivity, the ionization energy and concentration of deep centers in an overcompensated semiconductor placed between insulator plates (40–100 μm thick polyethylene terephthalate), to which a sinusoidal voltage was applied through copper contacts. However, in [11, 12] the experimental data on the conductivity and capacitance of the studied structure were not compared with theory.

The purpose of this work is to calculate the low-frequency admittance of a capacitor with the working substance “insulator–crystalline semiconductor with point t -defects in charge states (–1), (0) and (+1) with hopping migration of electrons between them–insulator”.

Model of capacitor with working substance “insulator–partially disordered semiconductor–insulator”

Let a wafer of highly defective crystalline silicon (hd -Si) with a thickness of d_s and a surface area A be in the middle between the metal plates of a flat capacitor and separated from them by the layers of insulator (e.g., polyimide) with a thickness of d_i (Figure 1a). The capacitor is connected to a constant electrical voltage source. The x coordinate axis is perpendicular to the surface of the semiconductor wafer occupying space $-d_s/2 < x < d_s/2$, the y and z coordinate axes are parallel to the wafer surface.

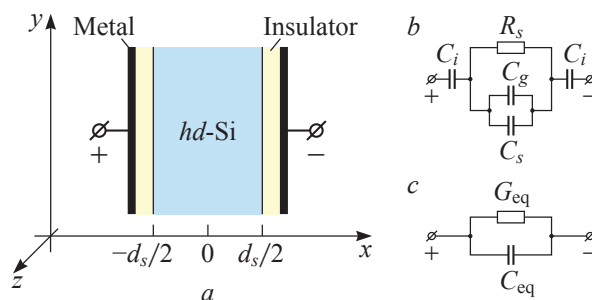


Figure 1 – Cross-section of capacitor with a wafer of highly defective crystalline silicon (hd -Si) of thickness d_s separated from the metal capacitor plates by the insulator layers of thickness d_i . Across the semiconductor wafer an electric potential difference is created by two metal electrodes parallel to the plane yz (a). Equivalent scheme of capacitor with the working substance “insulator–partially disordered semiconductor–insulator” (b). Simplified equivalent scheme of the system (c)

Let us assume that in one part the field potential on the wafer surface is positive $\phi(x = -d_s/2) = \phi_s$, and in the other it is negative $\phi(x = d_s/2) = -\phi_s$, then the potential difference applied to the semiconductor is $U_s = \phi(x = -d_s/2) - \phi(x = d_s/2) = 2\phi_s$. We will consider electrodes located parallel to the yz plane (so that the field distribution in the wafer along the y and z coordinates will be symmetric). The screening of the external electrostatic field is caused by the redistribution of electrons hopping via defects in the charge states (0, –1, and +1; in units of elementary charge e against the background of a silicon matrix),

i.e. by the migration of charge states of immobile defects to a distance much greater than the average distance between them.

The capacitor with the working substance “insulator–partially disordered semiconductor–insulator” contains series-connected capacitances of insulating layers C_i and a parallel $R_s(C_s + C_g)$ -circuit of the semiconductor wafer (see Figure 1b). Here $C_i = \varepsilon_i A/d_i$ and $C_g = \varepsilon_s A/d_s$ are the geometric capacitances of insulator and semiconductor with static dielectric permittivities $\varepsilon_i = \varepsilon_{r,i}\varepsilon_0$ and $\varepsilon_s = \varepsilon_{r,s}\varepsilon_0$ (we assume that radiation defects do not contribute to the static dielectric constant of Si crystals), $\varepsilon_{r,i} = 3.5$ and $\varepsilon_{r,s} = 11.5$ are the relative permittivities of the polyimide and the silicon crystal lattice, $\varepsilon_0 = 8.85$ pF/m is the electric constant, $R_s = R_s(U)$ is the semiconductor resistance, $C_s = C_s(U)$ is the differential capacitance of the semiconductor, U is the voltage created by the metal plates of the capacitor.

The real part $C_{\text{eq}} = C_{\text{eq}}(U)$ of the complex electrical capacitance and the active component of the conductivity $G_{\text{eq}} = G_{\text{eq}}(U)$ of the structure in the equivalent circuit (see Figure 1c) is [11, 13]:

$$C_{\text{eq}} = \frac{C_i}{2} \frac{1 + \omega^2 R_s^2 (C_g + C_s)(C_g + C_s + C_i/2)}{1 + [\omega R_s (C_g + C_s + C_i/2)]^2}, \quad (1)$$

$$G_{\text{eq}} = \frac{\omega^2 R_s (C_i/2)^2}{1 + [\omega R_s (C_g + C_s + C_i/2)]^2}, \quad (2)$$

where $U (= U_{\text{dc}})$ is the constant voltage across the capacitor plates, ω is the angular frequency of the variable component of the measuring signal with the amplitude $|U_{\text{ac}}| \ll |U|$.

From Eqs. (1) and (2) we find the total conduction (admittance) $Y = Y(U)$ and the phase shift $\theta = \theta(U)$ between current and voltage of the capacitor with the working substance “insulator–partially disordered semiconductor–insulator”:

$$Y = [G_{\text{eq}}^2 + (\omega C_{\text{eq}})^2]^{1/2} = \frac{\omega C_i}{2} \left(\frac{1 + [\omega R_s (C_g + C_s)]^2}{1 + [\omega R_s (C_g + C_s + C_i/2)]^2} \right)^{1/2}, \quad (3)$$

$$\theta = \arctan(-\omega C_{\text{eq}}/G_{\text{eq}}) = \arctan \left(-\frac{1 + \omega^2 R_s^2 (C_g + C_s)(C_g + C_s + C_i/2)}{\omega R_s C_i/2} \right), \quad (4)$$

where $R_s = R_s(U)$ and $C_s = C_s(U)$. Note that the total resistance (impedance) $Z = Z(U)$ is related to the admittance Y as follows: $Z = Y^{-1}$.

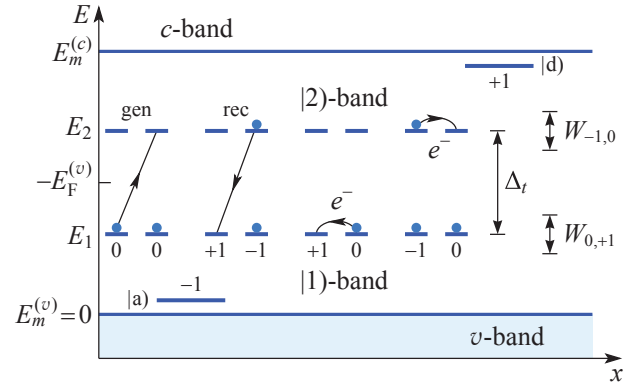


Figure 2 – Single-electron energy E as function of x coordinate in semiconductor with point two-level (triple-charged) defects of t -type in equilibrium (at $U = 0$): $E_m^{(c)}$ is the mobility edge of conduction band electrons, $E_F^{(v)} < 0$ is the Fermi level in the band gap, counted from the hole mobility edge ($E_m^{(v)} = 0$), $\Delta_t = E_2 - E_1$ is the width of energy gap between |1)- and |2)-bands, $W_{0,+1}$ and $W_{-1,0}$ are widths of |1)- and |2)-bands. Arrows show hops of single electrons e^- via |1)- and |2)-bands as well as generation [gen: $2(0) \rightarrow (-1) + (+1)$] and recombination [rec: $(-1) + (+1) \rightarrow 2(0)$] electron transitions between them; |d) and |a) are states of shallow hydrogen-like donors and acceptors in the charge states (+1) and (-1), respectively

For $R_s \gg 1/\omega C_s$ from Eq. (1), the inverse equivalent capacity of the entire structure is $1/C_{\text{eq}} = 2/C_i + 1/(C_s + C_g)$. Since the capacitances of insulator layers C_i and semiconductor $C_s + C_g$ are connected in series, the charge on each of them is equal to Q . Thus, the voltage drops across insulators $U_i = Q/C_i$ and across semiconductor $U_s = Q/(C_s + C_g)$ are related to the voltage across the capacitor $U = Q/C_{\text{eq}}$ as follows: $U = 2U_i + U_s$. By substituting the charge Q on the capacitor, expressed in terms of U_s and $C_s + C_g$, into U we obtain the voltage across the capacitor U_s , for which the voltage drop across the semiconductor is equal to U_s :

$$U = U_s \frac{C_s + C_g}{C_{\text{eq}}} = U_s \frac{2(C_s + C_g) + C_i}{C_i}. \quad (5)$$

A highly defective silicon crystal (hd -Si) contains point two-level t -type defects in a concentration sufficient to stabilize the Fermi level E_F in the energy gap. Defects of t -type in the charge states (+1) and (0) form a |1)-band with the energy levels E_1 , and the ones in the charge states (0) and (-1) form a |2)-band in the band gap (energy levels E_2), located closer to the c -band than |1)-band (Figure 2). Examples of t -defects are amphoteric impurities (Au, Cu).

Let us consider silicon under conditions of only hopping electron migration via immobile radiation

defects (of t -type) in the charge states (-1) and (0) , as well as in the charge states (0) and $(+1)$. The total concentration of defects in the charge states (0) , (-1) , and $(+1)$ is $N_t = N_0 + N_{-1} + N_{+1}$.

We assume that $|d\rangle$ - and $|a\rangle$ -centers are completely ionized and their concentrations N_d and N_a satisfy the conditions: $N_d/N_t \ll 1$ and $N_a/N_t \ll 1$. Thus, the condition of electrical neutrality of the partially disordered semiconductor has the form:

$$N_{+1} = N_{-1}, \quad (6)$$

where $N_{+1} = N_{t,+1}$ and $N_{-1} = N_{t,-1}$.

The concentrations of ionized and neutral defects can be written as [14]:

$$N_Z = N_t f_Z, \quad (7)$$

where f_Z is the probability that the defect is in one of three possible charge states $Z = -1, 0, +1$.

If we neglect the excited states of radiation defects, then the inverse distribution functions $1/f_Z$ of defects in $|1\rangle$ - and $|2\rangle$ -bands over charge states are [3, 4]:

$$\begin{aligned} \frac{1}{f_{-1}} &= 1 + \beta_2 \exp\left(\frac{E_F^{(v)} + E_2}{k_B T}\right) + \frac{\beta_2}{\beta_1} \exp\left(\frac{E_1 + E_2 + 2E_F^{(v)}}{k_B T}\right), \\ \frac{1}{f_0} &= 1 + \frac{1}{\beta_1} \exp\left(\frac{E_F^{(v)} + E_1}{k_B T}\right) + \frac{1}{\beta_2} \exp\left(\frac{-(E_F^{(v)} + E_2)}{k_B T}\right), \\ \frac{1}{f_{+1}} &= 1 + \beta_1 \exp\left(\frac{-(E_F^{(v)} + E_1)}{k_B T}\right) + \\ &+ \frac{\beta_1}{\beta_2} \exp\left(\frac{-(E_1 + E_2 + 2E_F^{(v)})}{k_B T}\right), \end{aligned} \quad (8)$$

where $E_F^{(v)} = E_v - E_F$ is the Fermi level (chemical potential) E_F , counted from the v -band hole mobility edge ($E_m^{(v)} = 0$) of an undoped crystal [15, 16]; $E_F^{(v)} < 0$ for the Fermi level in the band gap; $E_1 = E_0 - E_{+1} > 0$, $E_2 = E_{-1} - E_0 > 0$; $k_B T$ is the thermal energy. For dominant radiation defects in silicon (mainly divacancies), following the experimental data from [17–19], we assume: $E_1 = 225$ meV, $E_2 = 575$ meV, i.e. $\Delta_t = E_2 - E_1 = 350$ meV, $\beta_1 = \beta_0/\beta_{+1} = 1$, $\beta_2 = \beta_0/\beta_{-1} = 1$, where β_Z is the number of quantum states of the defect in the charge state Z with energy E_Z .

With the total concentration of charged radiation defects $N_{ch} = N_{-1} + N_{+1}$ with charge $\pm e$ randomly (Poissonian) distributed over the crystal, we have equal rms fluctuations $W = W_{-1,0} = W_{0,+1}$ of the electrostatic energy, i.e. the widths of $|2\rangle$ - and $|1\rangle$ -bands are [20, 21]:

$$W_{-1,0} = W_{0,+1} = 1.637 \frac{e^2}{4\pi\epsilon_s} \left(\frac{4\pi}{3}(N_{ch})_{eq}\right)_{\phi_s=0}^{1/3}, \quad (9)$$

where the Coulomb interaction of each charged defect only with its nearest charged defect (ion) is taken into account; e is the elementary charge; $(N_{ch})_{eq} = N_t/2$ is determined from the condition of maximum effective concentrations $N_{-1,0} = N_{0,+1} = N_{-1}N_0/N_t = N_0N_{+1}/N_t$ of single electrons hopping via t -defects in the charge states (-1) , (0) and in charge states (0) , $(+1)$. Then we obtain $(N_{-1})_{max} = (N_{+1})_{max} = N_t/4$, $(N_0)_{max} = N_t/2$ and $(N_{-1,0})_{max} = (N_{0,+1})_{max} = N_t/8$ [22]. Note that $3W > \Delta_t$.

For a semiconductor with uniformly distributed point defects of the crystal lattice, the values of the function $f_Z(\varphi)$ depend on the coordinate x only through the potential $\varphi(x)$ and are obtained from f_Z by replacing $E_F^{(v)} < 0$ in Eq. (8) by

$$E_F^{(v)}(\varphi(x)) = E_F^{(v)} - e\varphi(x), \quad (10)$$

that is for $\varphi(x) < 0$ the Fermi level $E_F^{(v)}(\varphi)$ shifts to the top of the v -band and for $\varphi(x) > 0$ it shifts to the band gap.

The change in the concentration of charge states $Z = -1, 0, +1$ of $N_Z(\varphi) - N_Z$ defects in the electric field with the potential $\varphi(x)$ is determined by Eq. (7) taking into account Eqs. (10) and (8). In this case, it is assumed that the energy gap Δ_t between $|1\rangle$ - and $|2\rangle$ -bands, as well as the width of each band W , do not depend on the potential.

Due to the symmetry of the problem with respect to reflection $x \rightarrow -x$, we consider only the region $-d_s/2 \leq x \leq 0$. The electrostatic potential $\varphi(x)$ inside the semiconductor at a point with coordinate x satisfies the Poisson equation [23, 24]:

$$\frac{d^2\varphi}{dx^2} = \frac{1}{2} \frac{d}{d\varphi} \left(\frac{d\varphi}{dx}\right)^2 = -\frac{\rho(\varphi)}{\epsilon_s}, \quad (11)$$

where $\rho(\varphi(x)) = e[N_{+1}(\varphi(x)) - N_{-1}(\varphi(x))]$ is the volume density of the induced charge; $N_{-1} = N_{+1}$ is the electrical neutrality condition of the semiconductor wafer at $\varphi_s = 0$.

By integrating Eq. (11) over φ , we obtain the electric field strength:

$$\frac{d\varphi}{dx} = \pm \left(-\frac{2}{\epsilon_s} \int_0^{\varphi_s} \rho(\varphi) d\varphi\right)^{1/2}, \quad (12)$$

where for $\varphi_s > 0$ the “ $-$ ” sign should be taken, while for $\varphi_s < 0$ the “ $+$ ” sign should be taken.

From Eq. (11), taking into account Eq. (12), we

obtain the charge Q_s induced by the external electric field per unit area A of the flat surface of the silicon wafer:

$$\begin{aligned} \frac{Q_s}{A} &= \int_{-d_s/2}^0 \rho(x) dx = \varepsilon_s \left. \frac{d\varphi}{dx} \right|_{x=-d_s/2} = \\ &= \pm \left(-2\varepsilon_s \int_0^{\varphi_s} \rho(\varphi) d\varphi \right)^{1/2}, \end{aligned} \quad (13)$$

where for $\varphi_s > 0$ the “–” sign should be taken, while for $\varphi_s < 0$ the “+” sign should be taken.

The differential electrical capacitance per unit silicon surface area A , taking into account Eq. (13), is

$$\begin{aligned} \frac{C_s}{A} &= - \frac{dQ_s}{A d\varphi_s} = \frac{\rho(\varphi_s)}{d\varphi/dx|_{x=-d_s/2}} = \\ &= \frac{eN_t [f_{+1}(\varphi_s) - f_{-1}(\varphi_s)]}{\pm \left(-(2/\varepsilon_s) \int_0^{\varphi_s} \rho(\varphi) d\varphi \right)^{1/2}}. \end{aligned} \quad (14)$$

The change under the action of the field effect of the hopping electrical conductivity [caused by the migration of single electrons across the wafer thickness via immobile radiation t -defects in the charge states (–1) and (0), as well as in the charge states (0) and (+1)] is

$$\begin{aligned} \delta\sigma(\varphi_s) &= \frac{e}{d_s} \int_{\varphi_s}^0 \frac{N_{-1,0}(\varphi)M_{-1,0} + N_{0,+1}(\varphi)M_{0,+1}}{d\varphi/dx} d\varphi - \\ &- \frac{e}{d_s} \int_{\varphi_s}^0 \frac{N_{-1,0}(0)M_{-1,0} + N_{0,+1}(0)M_{0,+1}}{d\varphi/dx} d\varphi + \\ &+ \frac{e}{d_s} \int_{-\varphi_s}^0 \frac{N_{-1,0}(\varphi)M_{-1,0} + N_{0,+1}(\varphi)M_{0,+1}}{d\varphi/dx} d\varphi - \\ &- \frac{e}{d_s} \int_{-\varphi_s}^0 \frac{N_{-1,0}(0)M_{-1,0} + N_{0,+1}(0)M_{0,+1}}{d\varphi/dx} d\varphi, \end{aligned} \quad (15)$$

where $N_{-1,0}(\varphi) = N_{-1}(\varphi)N_0(\varphi)/N_t$ and $N_{0,+1}(\varphi) = N_0(\varphi) \times N_{+1}(\varphi)/N_t$ are the effective concentrations of single electrons hopping via t -defects in the charge states (–1), (0) and in the charge states (0), (+1); $M_{-1,0}$ and $M_{0,+1}$ are the drift mobilities of electrons hopping via t -defects in the charge states (–1), (0) and in the charge states (0), (+1).

The relationship between the hopping diffusion coefficients $D_{-1,0}$ and $D_{0,+1}$ and the drift hopping mo-

bilities $M_{-1,0}$ and $M_{0,+1}$ of electrons hopping via point t -defects of the crystal matrix is established by the Nernst–Einstein–Smoluchowski relation (see, e.g., [3, 25]):

$$\frac{D_{-1,0}}{M_{-1,0}} = \xi_{-1,0} \frac{k_B T}{e}, \quad \frac{D_{0,+1}}{M_{0,+1}} = \xi_{0,+1} \frac{k_B T}{e}, \quad (16)$$

where $\xi_{-1,0} \geq 1$, $\xi_{0,+1} \geq 1$ are the dimensionless parameters, which are determined by the ratio of the fluctuation spread of t -defect levels (with average values of E_1 and E_2) to the thermal energy $k_B T$; further we assume $\xi_{-1,0} = \xi_{0,+1} = 1$.

The diffusion coefficients $D_{-1,0}$ and $D_{0,+1}$ of electrons hopping via t -defects in a covalent crystal matrix (see Eq. (16)) can be estimated by averaging over all probable hopping lengths r (cf. [22–27]):

$$D_{-1,0} = \frac{1}{6} \langle \Gamma_{-1,0}(r, T) r^2 \rangle, \quad D_{0,+1} = \frac{1}{6} \langle \Gamma_{0,+1}(r, T) r^2 \rangle, \quad (17)$$

where $\Gamma_{-1,0}(r, T) = \nu_{lt} \exp[-(2r/a_{-1} + W_{-1,0}/k_B T)]$ and $\Gamma_{0,+1}(r, T) = \nu_{lt} \exp[-(2r/a_0 + W_{0,+1}/k_B T)]$ are frequencies of electron hopping via t -defects in charge states (–1), (0) and (0), (+1) [28]; $\nu_{lt} \approx 10$ THz is the characteristic frequency of crystal matrix phonons; $a_{-1} = \hbar/(2m_0 E_2)^{1/2}$ and $a_0 = \hbar/(2m_0 E_1)^{1/2}$ are the radii of localization of an electron at the t -defect in the charge state (–1) and (0), respectively, m_0 is the electron mass in vacuum.

From Eq. (17), taking into account the distribution of distances r between t -defects [21], we get:

$$\begin{aligned} D_{-1,0} &= \frac{2\pi\nu_{lt}N_{eq}}{3} \exp\left(\frac{W_{-1,0}}{k_B T}\right) \times \\ &\times \int_0^\infty r^4 \exp\left[-\left(\frac{2r}{a_{-1}} + \frac{4\pi r^3}{3} N_{eq}\right)\right] dr, \\ D_{0,+1} &= \frac{2\pi\nu_{lt}N_{eq}}{3} \exp\left(\frac{W_{0,+1}}{k_B T}\right) \times \\ &\times \int_0^\infty r^4 \exp\left[-\left(\frac{2r}{a_0} + \frac{4\pi r^3}{3} N_{eq}\right)\right] dr, \end{aligned} \quad (18)$$

where $N_{eq} = (N_{-1,0})_{max} = (N_{0,+1})_{max} = N_t/8$.

From Eq. (15), taking into account Eqs. (16)–(18), we obtain the resistance of a highly defective crystalline silicon (hd -Si) wafer due to the hopping of single electrons via t -defects along its thickness:

$$R_s = R_s(U(\varphi_s)) = \frac{d_s}{A\sigma}, \quad (19)$$

where d_s and A are the thickness and the surface area of the hd -Si wafer, $\sigma = \sigma(\varphi_s) = \sigma(0) + \delta\sigma(\varphi_s)$ is the electrical conductivity, and $\sigma(0) = e[N_{-1,0}(0)M_{-1,0} + N_{0,+1}(0)M_{0,+1}]$ is the conductivity at $\varphi_s = 0$. For the considered low frequencies, the electrical conductivity σ is frequency-independent [29, 30].

Note that Eqs. (14) and (19) were obtained under the assumption of quasi-stationary filling of energy levels according to Eq. (8) taking into account Eq. (10), therefore C_s and R_s are the quasi-static (low-frequency) capacitance and resistance of semiconductor. The quasi-stationarity condition is satisfied at $\omega/2\pi \ll \Gamma_{-1,0}(r, T)$ and $\omega/2\pi \ll \Gamma_{0,+1}(r, T)$. In other words, this can be expressed by the inequality $\omega/2\pi \ll \sigma/\varepsilon_s$, where ε_s/σ is the Maxwell relaxation time for hopping conduction.

Calculation results and discussion

The calculations were carried out for the following parameter values: semiconductor thickness $d_s = 150 \mu\text{m}$, insulator thickness $d_i = 3 \mu\text{m}$, relative permittivities of semiconductor (hd -Si) $\varepsilon_{r,s} = 11.5$ and insulator (polyimide) $\varepsilon_{r,i} = 3.5$, frequency of alternating electric field $\omega/2\pi = 1 \text{ kHz}$.

Figure 3a shows the results of calculating the ratio of the low-frequency admittance $Y(U)$ to $\omega C_i/2$ according to Eq. (3) at various values of the voltage U created by metal electrodes on the surface of insulator interlayers, for $N_t = 3 \cdot 10^{19} \text{ cm}^{-3}$ at temperatures $T = 250, 300, 350 \text{ K}$. The values of U are related to U_s by Eq. (5) and $U_s = 2\varphi_s$ was chosen so that the inequality $eU_s \leq \Delta_t$ is fulfilled. It is seen that for $U = 0$ (flat-band mode) the admittance of the capacitor with the working substance “insulator–partially disordered semiconductor–insulator” increases with temperature.

Figure 3b shows the results of calculating the ratio of the low-frequency admittance $Y(U)$ to $\omega C_i/2$ according to Eq. (3) at different values of voltage U created by metal electrodes on the surface of insulator interlayers for temperature $T = 300 \text{ K}$ at concentrations of t -defects in disordered silicon $N_t = 1 \cdot 10^{19}, 3 \cdot 10^{19}, 1 \cdot 10^{20} \text{ cm}^{-3}$. It is seen that the admittance increases with the concentration of t -defects.

Figure 4a shows the results of calculating the phase shift angle $\theta(U)$ between current and voltage according to Eq. (4) at various values of voltage U created by metal electrodes on the surface of insulator interlayers, for $N_t = 3 \cdot 10^{19} \text{ cm}^{-3}$ at temperatures $T = 250, 300, 350 \text{ K}$. It is seen that the absolute value of the phase shift angle decreases with temperature.

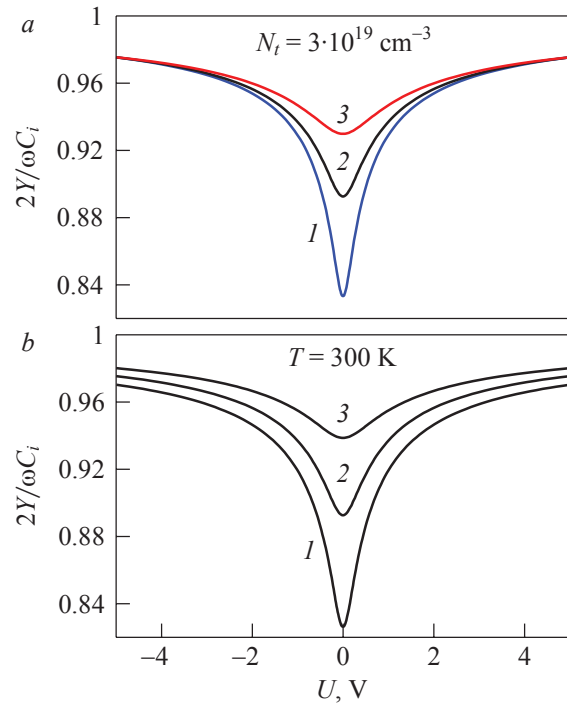


Figure 3 – Dependence of admittance $2Y/\omega C_i$ on electrode voltage U , calculated by Eq. (3): *a*) for $N_t = 3 \cdot 10^{19} \text{ cm}^{-3}$ at temperatures T (K): 250 (curve 1), 300 (2), and 350 (3); *b*) for $T = 300 \text{ K}$ at t -defect concentrations N_t (cm^{-3}): $1 \cdot 10^{19}$ (1), $3 \cdot 10^{19}$ (2), and $1 \cdot 10^{20}$ (3)

Figure 4b shows the results of calculating the phase shift angle $\theta(U)$ according to Eq. (4) at various values of the voltage U created by metal electrodes for temperature $T = 300 \text{ K}$ at the concentration of t -defects in disordered silicon $N_t = 1 \cdot 10^{19}, 3 \cdot 10^{19}, 1 \cdot 10^{20} \text{ cm}^{-3}$. It is seen that in the flat-band mode (at $U = 0$), all other conditions being equal, the phase shift angle modulus is minimum for the concentration of t -defects $N_t = 3 \cdot 10^{19} \text{ cm}^{-3}$ and is maximum for $N_t = 1 \cdot 10^{20} \text{ cm}^{-3}$.

Note that the value of the Fermi level energy $E_F^{(v)} = 400 \text{ meV}$, obtained from the electrical neutrality condition $N_{+1} = N_{-1}$, does not depend on the temperature, since $E_F^{(v)}$ is in the middle between |1)- and |2)-band. This practically coincides with the experimental value of $E_F^{(v)}$ in silicon [17–19], which contains a high concentration of radiation defects.

Note that the capacitor with the working substance “insulator–partially disordered semiconductor–insulator” is radiation-resistant, because radiation defects are already present in the semiconductor in large numbers. This suggests that this element is promising for use as a varactor. Also, the dependences of the electrophysical characteristics (Eqs. (1)–(4)) on the potential at the electrodes make it pos-

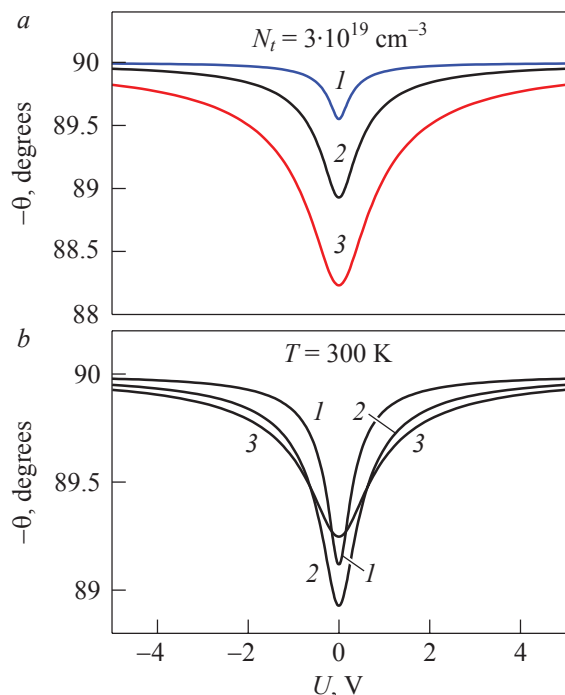


Figure 4 – Dependence of phase shift angle θ on electrode voltage U , calculated by Eq. (4): *a*) for $N_t = 3 \cdot 10^{19} \text{ cm}^{-3}$ at temperatures T (K): 250 (curve 1), 300 (2), and 350 (3); *b*) for $T = 300 \text{ K}$ at t -defect concentrations N_t (cm^{-3}): $1 \cdot 10^{19}$ (1), $3 \cdot 10^{19}$ (2), and $1 \cdot 10^{20}$ (3)

sible to determine the concentration of t -defects in the disordered semiconductor separated by insulator interlayers from the capacitor plates [11].

Conclusion

The structure “insulator–partially disordered semiconductor–insulator” is proposed as a working substance of a capacitor. The semiconductor layer with a thickness of $150 \mu\text{m}$ is separated from the metal electrodes of the capacitor by insulating layers of polyimide with a thickness of $3 \mu\text{m}$. The semiconductor layer is a highly defective silicon crystal containing radiation point two-level t -defects in three charge states (-1), (0), and ($+1$) with hopping migration of single electrons via them, i.e. defects form $|1\rangle$ - and $|2\rangle$ -bands in the band gap.

The calculation gives a nonmonotonic dependence of the low-frequency admittance and the phase angle between current and voltage on the electric potential at the metal plates. At the concentration of t -type radiation defects equal to $3 \cdot 10^{19} \text{ cm}^{-3}$, with an increase in temperature from 250 to 350 K, the admittance increases by about 12%. With an increase in the concentration of t -defects from $1 \cdot 10^{19}$ to $1 \cdot 10^{20} \text{ cm}^{-3}$ at temperature of 300 K, the admittance

of the capacitor increases by about 13%. In the calculations, for the first time, the diffusion coefficients were averaged over all probable electron hopping lengths via t -defects in the charge states (-1), (0) and (0), ($+1$) in the covalent crystal matrix. Note that the considered element is radiation-resistant, since the semiconductor layer already contains radiation point defects in a high concentration.

Acknowledgments

The work was supported by the Belarusian National Research Program “Materials Science, New Materials and Technologies” and by the European Union Framework Programme for Research and Innovation Horizon 2020 (grant No. H2020-MSCA-RISE-2019-871284 SSHARE).

References

1. Zvyagin I.P. Controlling the jump-over conductivity of compensated semiconductors with the aid of an electrical field. *Sov. Phys. Dokl.*, 1977, vol. 22, no. 11, pp. 647–648.
2. Poklonskii N.A., Vyrko S.A. Screening of an electric field and the quasi-static capacitance of an induced charge in semiconductors with hopping conductivity. *Russ. Phys. J.*, 2002, vol. 45, no. 10, pp. 1001–1007. DOI: 10.1023/A:1022867001332
3. Poklonski N.A., Vyrko S.A., Zabrodskii A.G. Calculation of capacitance of self-compensated semiconductors with intercenter hops of one and two electrons (by the example of silicon with radiation defects). *Semiconductors*, 2008, vol. 42, no. 12, pp. 1388–1394. DOI: 10.1134/S1063782608120038
4. Poklonski N.A., Vyrko S.A., Zabrodskii A.G. Field effect and capacitance of silicon crystals with hopping conductivity over point radiation defects pinning the Fermi level. *Semiconductors*, 2007, vol. 41, no. 11, pp. 1300–1306. DOI: 10.1134/S1063782607110048
5. Poklonski N.A., Kovalev A.I., Vyrko S.A. [Low-frequency electrical capacitance of semiconductor diode with hopping conductivity via triple-charged defects]. *Doklady Natsional'noi akademii nauk Belarusi* [Doklady of the National Academy of Sciences of Belarus], 2017, vol. 61, no. 4, pp. 52–59 (in Russian).
6. Żukowski P.W., Kantorow S.B., Kiszczak K., Mączka D., Rodzik A., Stelmakh V.F., Czarnicka-Such E. Study of the dielectric function of silicon irradiated with a large dose of neutrons. *Phys. Status Solidi A*, 1991, vol. 128, № 2, pp. K117–K121. DOI: 10.1002/pssa.2211280243
7. Djurić Z., Smiljanić M. Static characteristics of metal–insulator–semiconductor–insulator–metal (MISIM)

structures—I. Electric field and potential distributions. *Solid-State Electron.*, 1975, vol. 18, no. 10, pp. 817–825. DOI: 10.1016/0038-1101(75)90001-5

8. Djurić Z., Smiljanić M., Tjapkin D. Static characteristics of the metal–insulator–semiconductor–insulator–metal (MISIM) structure—II. Low frequency capacitance. *Solid-State Electron.*, 1975, vol. 18, no. 10, pp. 827–831. DOI: 10.1016/0038-1101(75)90002-7

9. Ng K.K. Complete Guide to Semiconductor Devices. New-York, Wiley–IEEE Press, 2002, xxiv+740 p. DOI: 10.1002/9781118014769

10. Krupski J. Interfacial capacitance. *Phys. Status Solidi B*, 1990, vol. 157, no. 1, pp. 199–207. DOI: 10.1002/pssb.2221570119

11. Berman L.S., Klinger P.M., Fistul' V.I. Determination of the parameters of deep centers in an overcompensated semiconductor from the temperature dependence of the capacitance and active conductance. *Sov. Phys. Semicond.*, 1989, vol. 23, no. 11, p. 1206–1208.

12. Elfimov L.B., Ivanov P.A. Surface capacitance of a semiconductor with a deep dopant (in the example of *p*-6H-SiC). *Semiconductors*, 1994, vol. 28, no. 1, pp. 97–100.

13. Poklonski N.A., Gorbachuk N.I. [Fundamentals of impedance spectroscopy of composites]. Minsk, BSU, 2005, 130 p. (in Russian).

14. Poklonskii N.A., Stelmakh V.F., Tkachev V.D., Voitikov S.V. Screening of electrostatic fields in semiconductors by multicharged defects. *Phys. Status Solidi B*, 1978, vol. 88, no. 2, pp. K165–K168. DOI: 10.1002/pssb.2220880266

15. Mott N. Impurity bands in silicon and germanium. *Disordered Semiconductors*, ed. by M.A. Kastner, G.A. Thomas, S.R. Ovshinsky. New York, Plenum Press, 1987, pp. 3–10. DOI: 10.1007/978-1-4613-1841-5_2

16. Mott N. The mobility edge since 1967. *J. Phys. C: Solid St. Phys.*, 1987, vol. 20, no. 21, pp. 3075–3102. DOI: 10.1088/0022-3719/20/21/008

17. Lugakov P.F., Lukashevich T.A., Shusha V.V. Nature of the defect determining the Fermi level stabilization in irradiated silicon. *Phys. Status Solidi A*, 1982, vol. 74, no. 2, pp. 445–452. DOI: 10.1002/pssa.2210740209

18. Kuznetsov N.V., Soloviev G.G. [Radiation resistance of silicon]. Moscow, Energoatomizdat Publ., 1989, 96 p. (in Russian).

19. Brudnyi V.N. Charge neutrality in semiconductors: defects, interfaces, surface. *Russ. Phys. J.*, 2013,

vol. 56, no. 7, pp. 754–756.

DOI: 10.1007/s11182-013-0095-4.

20. Poklonski N.A., Vyrko S.A., Poklonskaya O.N., Zabrodskii A.G. Transition temperature from band to hopping direct current conduction in crystalline semiconductors with hydrogen-like impurities: Heat versus Coulomb attraction. *J. Appl. Phys.*, 2011, vol. 110, no. 12, pp. 123702 (1–7). DOI: 10.1063/1.3667287

21. Poklonski N.A., Vyrko S.A., Poklonskaya O.N., Zabrodskii A.G. Role of electrostatic fluctuations in doped semiconductors upon the transition from band to hopping conduction (by the example of *p*-Ge:Ga). *Semiconductors*, 2016, vol. 50, no. 6, pp. 722–734. DOI: 10.1134/S1063782616060191

22. Poklonskii N.A., Lopatin S.Yu. Stationary hopping photoconduction among multiply charged impurity atoms in crystals. *Phys. Solid State*, 1998, vol. 40, no. 10, pp. 1636–1640. DOI: 10.1134/1.1130623

23. Grundmann M. The Physics of Semiconductors. An Introduction Including Nanophysics and Applications. Berlin, Springer, 2021, xxxvii+889 p. DOI: 10.1007/978-3-030-51569-0

24. Poklonski N.A., Vyrko S.A., Podenok S.L. [Statistical physics of semiconductors]. Moscow, KomKniga Publ., 2005, 264 p. (in Russian).

25. Poklonski N.A., Vyrko S.A., Kovalev A.I., Dzeraviahia A.N. Drift-diffusion model of hole migration in diamond crystals via states of valence and acceptor bands. *J. Phys. Commun.*, 2018, vol. 2, no. 1, pp. 015013 (1–14). DOI: 10.1088/2399-6528/aa8e26

26. Baranovskii S., Rubel O. Chapter 9. Charge transport in disordered materials. *Springer Handbook of Electronic and Photonic Materials*, eds. S. Kasap, P. Capper. Berlin, Springer, 2017, pp. 193–218. DOI: 10.1007/978-3-319-48933-9_9

27. Shklovskii B.I., Efros A.L. Electronic Properties of Doped Semiconductors. Berlin, Springer, 1984, xii+388 p.

28. Klimkovich B.V., Poklonskii N.A., Stelmakh V.F. Alternating-current hopping electrical-conductivity of covalent semiconductors with deep-level defects. *Sov. Phys. Semicond.*, 1985, vol. 19, no. 5, pp. 522–524

29. Dyre J.C., Schröder T.B. Universality of ac conduction in disordered solids. *Rev. Mod. Phys.*, 2000, vol. 72, no. 3, pp. 873–892. DOI: 10.1103/RevModPhys.72.873

30. Long A.R. Frequency-dependent loss in amorphous semiconductors. *Adv. Phys.*, 1982, vol. 31, no. 5, pp. 553–637. DOI: 10.1080/00018738200101418

Impulsively-Laser Excitation and Propagation of Ultrasonic Waves through Nanomagnetic Fluid

A.R. Baev¹, A.I. Mitkovets², M.V. Asadchaya¹, A.L. Mayorov¹

¹*Institute of Applied Physics National Academy of Sciences of Belarus,
Akademicheskaya str., 16, Minsk 220072, Belarus*

²*Institute of Physics of the National Academy of Science of Belarus,
Nezavisimosti Ave., 68, Minsk 220072, Belarus*

Received 17.08.2021

Accepted for publication 08.10.2021

Abstract

Magnetic fluids belong to the class of nanomaterials with a high gain of light absorption, aggregative and sedimentation stability as well as controllability by external fields, which is of interest to use in the field of optoacoustics. The purpose of the work was to experimentally study the effect of the optoacoustic transformation in a magnetic fluid, depending on the concentration of magnetic colloidal particles, boundary conditions, intensity of the laser as well as to identify the possibilities of using the magnetic fluid as an element of the optoacoustic transformation in a number of applications.

A brief analysis of the optoacoustic transformation mechanism in a magnetic fluid was carried out and a technique and an installation that implements the shadow measurement variant developed. A Lotis type laser was used as a source of ultrasonic pulse-laser excitation in magnetic fluids. A quartz and air were used as a material transmitting the energy of laser radiation in a magnetic fluid. Receiving of ultrasound signals was made by a piezoelectric probe at a working frequency of 5 MHz. In the measurement process, the concentration of the dispersed phase in magnetic fluid was varied from zero to 8 % and the energy in the impulse – from zero to 10 mJ.

For the first time, it was established that: a) an amplitude of the function of the optoacoustic transformation in a magnetic fluid, depending on the concentration of the dispersed phase, has a maximum determined by the fluid physical properties and boundary conditions; b) for all samples within the measurement error, a quasilinear dependence of the specified amplitude of energy in the laser pulse in the range of 0–8 MJ has been established.

A number ways of the optoacoustic effects in magnetic fluids to use in ultrasonic testing, measuring the intensity of the laser radiation had been suggested.

Keywords: optoacoustic transformation, magnetic fluid, ultrasound.

DOI: 10.21122/2220-9506-2021-12-3-211-219

Адрес для переписки:

Баев А.Р.
Ин-т прикладной физики Национальной академии наук Беларуси,
ул. Академическая, 16, г. Минск 220072, Беларусь
e-mail: baev@iaph.bas-net.by

Address for correspondence:

Baev A.R.
Institute of Applied Physics of the National Academy
of Science of Belarus,
Akademicheskaya str., 16, Minsk 220072, Belarus
e-mail: baev@iaph.bas-net.by

Для цитирования:

A.R. Baev, A.I. Mitkovets, M.V. Asadchaya, A.L. Mayorov.
Impulsively-Laser Excitation and Propagation of Ultrasonic
Waves through Nanomagnetic Fluid.
Приборы и методы измерений.
2021. – Т. 12, № 3. – С. 211–219.
DOI: 10.21122/2220-9506-2021-12-3-211-219

For citation:

A.R. Baev, A.I. Mitkovets, M.V. Asadchaya, A.L. Mayorov.
Impulsively-Laser Excitation and Propagation of Ultrasonic
Waves through Nanomagnetic Fluid.
Devices and Methods of Measurements.
2021, vol. 12, no. 3, pp. 211–219.
DOI: 10.21122/2220-9506-2021-12-3-211-219

Импульсно-лазерное возбуждение и прохождение ультразвуковых волн через наномагнитную жидкость

А.Р. Баев¹, А.И. Митьковец², М.В. Асадчая¹, А.Л. Майоров¹

¹Институт прикладной физики НАН Беларуси,
ул. Академическая, 16, г. Минск 220072, Беларусь

²Институт физики НАН Беларуси,
пр-т Независимости, 68, г. Минск 220072, Беларусь

Поступила 17.08.2021

Принята к печати 08.10.2021

Магнитные жидкости относятся к классу наноматериалов, обладающих высоким коэффициентом поглощения света, агрегативной и седиментационной устойчивостью, а также управляемостью внешними полями, что представляет интерес для использования в области оптоакустики. Цель работы состояла в экспериментальном исследовании эффекта оптоакустического преобразования в магнитной жидкости в зависимости от концентрации дисперсной фазы и способа воздействия на неё лазерного излучения, а также выявления возможностей использования магнитной жидкости в качестве элемента оптоакустического преобразования в ряде приложений.

Проведён краткий анализ механизма оптоакустического преобразования в магнитной жидкости и разработана методика и установка, реализующая теневой вариант измерений, где в качестве источника импульсно-лазерного воздействия на магнитную жидкость использован лазер типа Lotis. В качестве материала световода, передающего энергию лазерного излучения в магнитной жидкости, использованы кварц и воздух. Приём ультразвуковых сигналов производился пьезопреобразователем на рабочей частоте 5 МГц. В процессе измерений варьировалась концентрация дисперсной фазы в магнитной жидкости (0–8 %) и энергия в импульсе (0–10 мДж).

Впервые установлено, что: а) амплитуда функции оптоакустического преобразования в магнитной жидкости в зависимости от концентрации дисперсной фазы, имеет максимум, величина и положение которого на оси концентраций определяется свойствами световода; б) для всех образцов в пределах погрешности измерений установлена квазилинейная зависимость указанной амплитуды от энергии в импульсе в диапазоне 0–8 мДж.

Предложен ряд схемных решений использования эффекта оптоакустического преобразования в магнитной жидкости для ввода сигнала в исследуемые объекты – применительно к их дефектоскопии и структуроскопии, а также для решения обратной задачи – измерения интенсивности лазерного излучения.

Ключевые слова: оптоакустическое преобразование, магнитная жидкость, ультразвуковые волны.

DOI: 10.21122/2220-9506-2021-12-3-211-219

Адрес для переписки:

Баев А.Р.
Ин-т прикладной физики Национальной академии наук Беларуси,
ул. Академическая, 16, г. Минск 220072, Беларусь
e-mail: baev@iaph.bas-net.by

Address for correspondence:

Baev A.R.
Institute of Applied Physics of the National Academy
of Science of Belarus,
Akademicheskaya str., 16, Minsk 220072, Belarus
e-mail: baev@iaph.bas-net.by

Для цитирования:

A.R. Baev, A.I. Mitkovets, M.V. Asadchaya, A.L. Mayorov.
Impulsively-Laser Excitation and Propagation of Ultrasonic
Waves through Nanomagnetic Fluid.
Приборы и методы измерений.
2021. – Т. 12, № 3. – С. 211–219.
DOI: 10.21122/2220-9506-2021-12-3-211-219

For citation:

A.R. Baev, A.I. Mitkovets, M.V. Asadchaya, A.L. Mayorov.
Impulsively-Laser Excitation and Propagation of Ultrasonic
Waves through Nanomagnetic Fluid.
Devices and Methods of Measurements.
2021, vol. 12, no. 3, pp. 211–219.
DOI: 10.21122/2220-9506-2021-12-3-211-219

Introduction

The development of methods of laser acoustic diagnostics and control of object in different phase states with structural inhomogeneity in hard-to-reach places requires the application of original approaches, new tools and materials [1]. Particularly, this concerns the combined methods of measurements where excitation of ultrasonic waves (UW) is performed by impulse-laser radiation and receiving by contact or non-contact transducers, for example [2–6]. This allows solving a number of important tasks on widening the possibilities of high-frequency acoustic probing of objects with powerful pulses by essentially increasing method sensitivity and simplifying the problems of information signal receiving.

Recently magnetic fluids (MF) related to the class of nanomaterials [7] are of essential interest for the use in acoustic measurement technique (and optoacoustics). Magnetic fluids are colloidal solutions possessing aggregative and sedimentary stability relatively magnetic suspended particles under the influence of external fields, including magnetic, electric and others while maintaining fluidity. Earlier it was proposed to use unique properties of MF in a number of acoustic applications including creation of acoustic contact, sound excitation by a variable magnetic field, directional control of acoustic fields and others [8].

Taking into account high stability of MF structure in magnetic fields, fluidity of the medium, and also the data on MF optical properties obtained before, it is of interest to consider the possibility of using MF as a distinctive matching managed optoacoustic (OA) element in a number of applications. Particularly, MF can be used as an OA converter or in ultrasound fluctuations that simultaneously combine the function of a controlled sound line, which creates a contact with the object of research, to form a focus and excitation of various elastic modes in materials with a minimum noise background; clearing the possibility of MF using to measure the intensity of laser radiation.

It is also necessary to pay attention to a number of works [9–12], in which magnetic field acts on birefringence, the rotation of the polarization plane, the change in the intensity of the light radiation passing through the MF films, and etc. Interesting

from the point of view of the using MF as an element of OA transducer is the data obtained in [13, 14], where it is shown that in the vicinity of the boundaries of the media there is an inhomogeneity of the concentration of the dispersed phase. It is also necessary to pay attention to a number of works, for example [9–12], in which the effects of the magnetic field influence on birefringence, the rotation of the polarization plane, and the laser light passing through the MF films, etc.

In the case of using MF as an element of OA converter and controlled by the magnetic field of the sound line [8], it is possible to excite in various media acoustic pulses of high intensity and low duration up to $\sim 1\text{--}10$ nS.

In the formation of the acoustic field in the test object to test it is necessary to take into account the fact that the laser radiation energy with an OA conversion to medium having characteristic thermo-physical (TP), acoustic (AC) and optical (OP) properties are transmitted to MF, followed by transformation according to the scheme: light – heat – ultrasonic waves (UW). And then the UW propagate into the object under study, which amplitude according to [2] can be represented as:

$$\tilde{A} \sim J_0(t, \Gamma_i) \tilde{K}_{OA}(\omega, TP, AC, OP) \tilde{F}[\omega, AC] D_{MF, O}, \quad (1)$$

where $J_0(t, \Gamma_i)$ is a flow of laser radiation, falling on the boundary light guide-MF; \tilde{K}_{OA} and \tilde{F} – integral (spectral) functions characterizing the passage of the radiation flow through the boundary of the light MF guide with the subsequent transformation into longitudinal waves, as well as the propagation of the latter through the MF sound line correspondingly; D_{MF} – the sound transmission coefficient of the boundary MF-object; ω – circular frequency.

It is interesting that there are the data obtained in [13, 14], where it is shown that in the vicinity of the boundaries of media there is an inhomogeneity of the concentration of the dispersed phase. It should be noted that the UW pulses arising from the OA transformation give us information about the space-time characteristics of the heat absorbed and the features of the heat transformation mechanism into acoustic energy. At the same time, it was shown in [13, 14], that the absorption coefficient of laser radiation in the vicinity of the boundaries of the media partition normally coefficient of the light attenuation is $\alpha_l = \alpha_l(z)$.

Those, it is varying in the surface layer according to normal to its boundary, which is due to the peculiarities of the technology of stabilization of the colloid system [7].

Using the results of research [2], the velocity of the laser excited UW and transmitted through rigid (*r*) or free boundary (*f*) into object to study can be presented as:

$$V_{r,f} = \frac{\beta I_0}{\rho_0 A_p} \int_{-\infty}^{\infty} \tilde{F}(\omega) \exp(-i\omega\tau) \int_0^{\infty} Y_{r,f} g(\alpha_l, \xi) d\xi, \quad (2)$$

where I_0 is a laser light intensity incident on the former, boundary, $g(\xi)$ describes the space distribution of the UW sources,

$$Y_r = \cos\left(\frac{\omega}{c_0} \xi\right); Y_f = \sin\left(\frac{\omega}{c_0} \xi\right),$$

β – is a temperature coefficient of MF compressibility, c_0 , ρ_0 and α_l are velocity, density and coefficient of the light extinction in MF respectively.

We assume that the diameter size of the light beam $\lambda_T \ll d \gg \alpha_l^{-1}$ where length of the excited heat $\lambda_T = \frac{(\chi_T / \omega c_p)^{1/2}}{2\pi}$, wave where χ is the heat capacity and thermal conductivity of the MF.

As shown by formulas (1) and (2), there is a direct link between the spectral and amplitude characteristics of the OA conversion and physical properties of MF, depending on the volume content Q of the colloid and the degree of structuring as well as from the dispersion base. According to the previously research [13], the amplitude of the OA transformation function $\tilde{A}(Q)$ measured in echo way, has a characteristic maximum as a result of concurrence of the thermophysical and acoustic properties of the MF samples and the boundary materials.

Interesting is the fact that with the characteristic concentration of the colloid $Q \geq Q_H \approx 2-3\%$ the spectrum of an excited in MF acoustic pulse is almost identical to the spectrum of the laser pulse. That is, the “long pulse” mode is implemented. If $Q = Q_L < 0.5\%$ and the emitting mode of a “short pulse is realized”.

The purpose of the work was to investigate experimentally the effect of OA transformation in MF depending on the concentration of disperse phase and the method of influence of laser radiation on the surface and also to detect the possibilities of

using MF as an element of OA transformation in a number of applications.

Experimental research technique and scheme

An experimental scheme of investigation is given in Figure 1 where a Lotis laser was used as LR source for research. The setup comprises an optical quantum generator with an electromagnetic radiation wavelength of 1.06 μm , consisting of an electrical pulse generator, an optical tube with a quantotrone, an optical system for correcting LR intensity, which provides its given value and uniformity on the front. LR pulse width at e^{-1} level is $\approx 8 \mu\text{s}$. After OA transformation on the boundary of the light-guide-MF, passing through MF and the protector, USO goes to the receiver from which a signal is received successively on the amplifier and then on the oscillograph BORDO 200, which is connected to the computer for processing the measurement results. The quantum generator and oscilloscope are started synchronously.

The cell has a cylindrical cavity filled with MF, ensuring a drop of LR with a diameter of $d \approx 5 \text{ mm}$ to the boundary of the light-guide-MF, where as a material of the light-guide air and quartz are used, which differ substantially on acoustic and thermal-physical properties. Moreover, in the first case a free boundary for OSU excited in MF surface layer was realized, and in the second case it was rigid in relation to the normal wave component. USO is received by a piezoelectric converter (PEC) with an operating frequency of 5 MHz and an oscillation period in a pulse almost 60 times less than the effective LR duration. The surface of PEC piezoplate is in contact with the solid-state acoustic line-protector, and its other side is in contact with the damper, as shown in Figure 1b and 1c. MF samples are made on the basis of mineral oil with a volume content of dispersion phase $Q = 0.3-8\%$.

The intensity of the laser pulse and duration of measurements are regulated so that in the result of thermal absorption non-linear effects will not appear and the temperature change of MF samples during measurement shall not exceed 1°C. Stability of the energy flow emitted by LR generator is $\approx 5-7\%$. By changing the intensity of LR source and measuring it with the PE-25SH device, a normalized dependence of the fixed electric radiation on the power of laser radiation J in mJ was constructed.

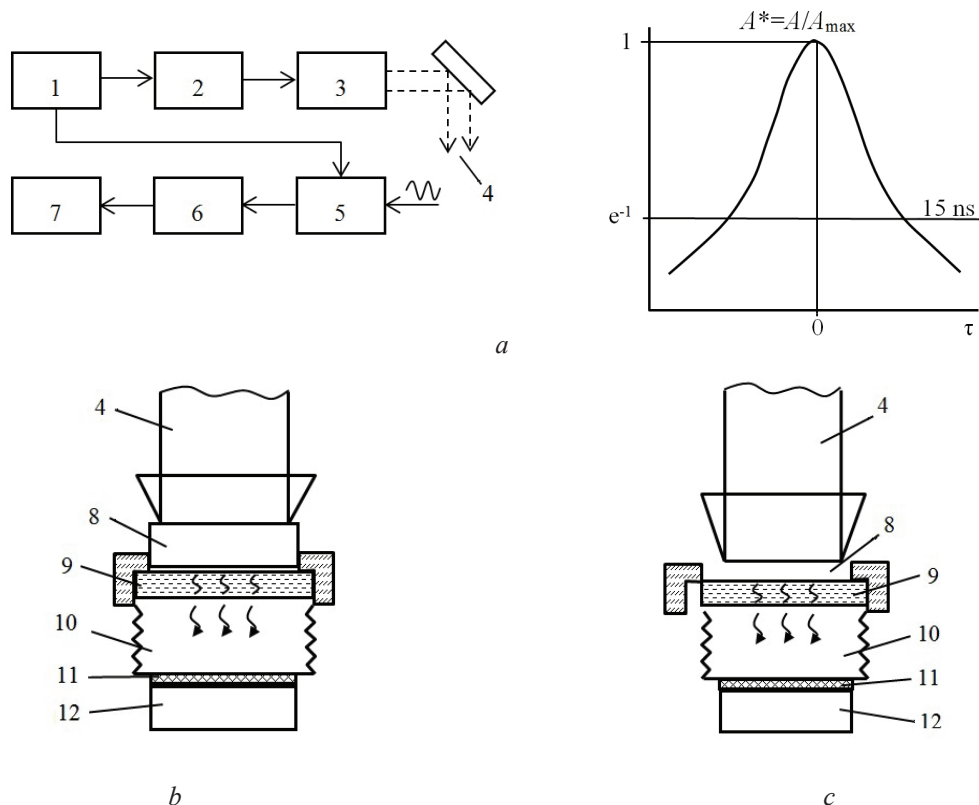


Figure 1 – Basic scheme of the electronic part of the installation with a characteristic form of a laser pulse (*a*) and ultrasonic cells (*b*, *c*) for the study of pulse-laser excitation and propagation of ultrasonic waves through magnetic fluid: 1 – generator of electrical pulses; 2 – laser; 3 – device for the correction of the laser beam; 4 – laser beam; 5 – preamp; 6 – oscilloscope BORDO 220; 7 – computer; 8 – light guide; 9 – magnetic fluid; 10 – protector; 11 – piezoplate; 12 – damper

Results of experimental studies

Below mainly the results of experimental studies devoted to the effect of OA transformation in MF are illustrated in Figure 2 and 3.

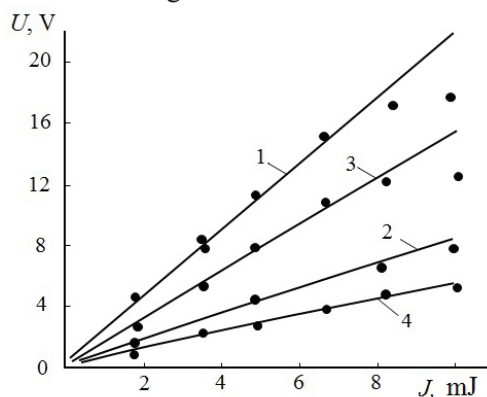


Figure 2 – Dependences of the acoustic amplitude excited by optoacoustic conversion on the energy of the laser pulse: action of the laser radiation on the air-magnetic fluid boundary (2, 4) and quartz-magnetic fluid (1, 3), where mineral oil is the dispersion base: $Q, \% = 0.3$ (1, 2); 8 (3, 4)

The qualitative analysis of the present experimental results is performed in comparison with those obtained earlier in the echo way. The characteristic dependences of the acoustic signal amplitude at OA-conversion depending on the laser pulse energy is in Figure 2 and on the dispersed phase concentration is in Figure 3 when the light flux penetrates into the MF sample through the quartz and air light guides are shown in Figure 1*b* and *c*.

As seen from the obtained in the present work and comparative data, the character of changes in the studied dependences of the informative signal is significantly influenced not only by the colloid concentration and dispersion base, but also by the boundary conditions of contact of the light guide with the MF.

We draw attention to the available qualitative similarity and difference between the behavior of normalized amplitudes of the function of the optoacoustic transformation when implementing the shadow (Figure 3*a*) and the previously studied echo measurement way (Figure 3*b*). The likeness lies in

the fact that the curves $A^*(Q) = A/A_{max}$ regardless of the boundary conditions have a maximum of characteristic and different values $Q = Q^*$. So, when contacting a quartz glass with MF and $Q > Q_{max}$, then dependence $A^*(Q)$ decreases monotonically by only less than 10 % achieved at $Q \rightarrow 8$ %. If the shadow mode is used then A^* decreases by ≈ 3 times. Note that the maxima of $A^*(Q)$ take place when a quartz glass contacts with MF in our experiment (shadow mode) and in [13] (echo mode) that is observed at different values of Q .

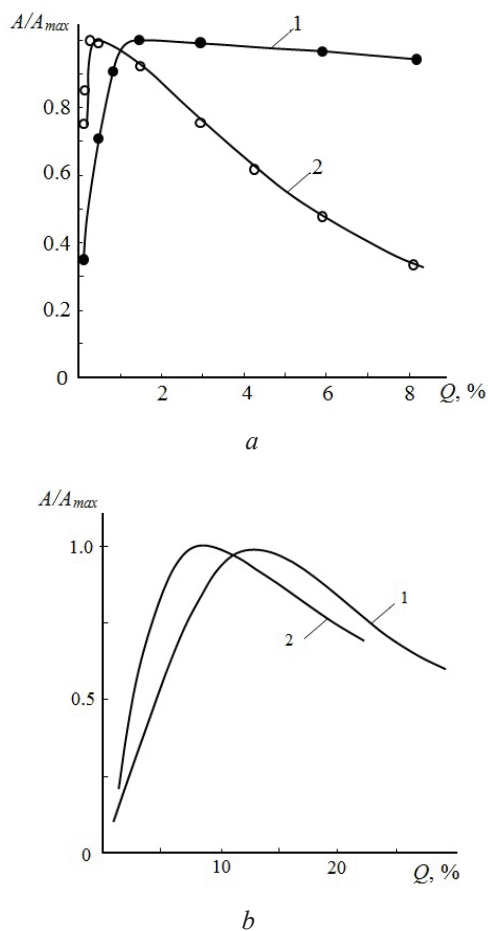


Figure 3 – Normalized amplitude of the acoustic waves at the receiving PEP excited by pulsed laser radiation, depending on the concentration of the dispersed phase in the magnetic fluid: *a* – shadow and *b* – echo mode of probing samples of magnetic fluid; light guide medium is quartz (1) and air (2); the base of the magnetic fluid is oil; *b* – light guide medium is quartz; the base of the magnetic fluid is transformer oil (1) and kerosene (2) [13]

Those, the content of the colloid in the solution of Q_B corresponds to the mode of OA conversion of a long pulse, and the Q_N – a short pulse. Interestingly, in the latter case, when $Q > Q_N$, then there is a sharp

drop of the dependence $A^*(Q)$. So in the vicinity of the extreme boundary of the variable range of concentrations of colloid $(A^*)_1/(A^*)_2 \rightarrow 4$.

To explain the dependency obtained above, we use expressions (1) and (2) as well as the calculated data, which have a significant effect on the parameters of the optoacoustic transformation function, which relate to changes in the thermophysical and acoustic properties of samples of MF and the light transparent material when varying the dispersed concentration phases in MF.

Attention is also drawn to the experimental dependences of the function $A^*(Q)$ obtained in [13–14], where the reception of acoustic oscillations was produced by a broad band receiver, as well as the results of a study of the depth of light penetration into the colloid in both echoes and the shadow modes.

First of all, we will pay attention to the difference between the characteristics of the excitation and the propagation of the informative signal on the OA path. When the shadow method is realized after the transformation of laser radiation into acoustic oscillations, the latter applies to the MF sound guide pass through the PEP piezoplate.

According to the spectral theory, in relation to the present problem, the amplitude of the probing signal will, first of all, depend on the operating frequency of the receiver and the length of the absorption zone of the light energy l , determined as $l \sim \alpha_l^{-1}$, where $\alpha \approx 1-3$.

As can be seen from Figure 3*a*, at the concentration of the colloid $Q \approx 0.43$, the value of this zone reaches to $l \approx 150-200 \mu\text{m}$, which corresponds to the time interval $\Delta t \sim l/2C_{MF}$, close to the PEP oscillation in pulse period $(f_p)^{-1}$ and determines mainly the position of the maximum of the amplitude of the signal.

A more detailed analysis of the phenomenon under study shows the necessity of taking into the influence of the effect of the wave phase inversion on the boundary of the light guide. Thus, on the boundary MF-air a phase shift $\Delta\beta \rightarrow \pi$ will be observed. I. e. this boundary is a kind of second source with oscillation vectors of the particles of the medium directed oppositely. And in this case at $Q > Q_{max}$ there will be a continuous decrease in the dimensionless distance $h_\lambda = h/\lambda_l$ or a phase shift between the sources mentioned, where k is some correction factor:

$$\Delta\psi \approx -\pi(1-2kh_\lambda), \quad (3)$$

where $h_\lambda \sim (\lambda\alpha_l)^{-1}$.

As for the excitation of elastic waves in the “long pulse” mode, then as is seen, with the growth of Q and, of course, the absorption light coefficient α_l , the effect of addition of amplitudes of the two sources will appear. Here part of the energy of the source localized at the division boundary of the MF-quartz will be emitted into a solid medium with an coefficient of transparency on energy:

$$D_{MF,qu} = 4R_{MF}R_{qu}(R_{MF} + R_{qu})^{-2},$$

which will lead (as calculations show) to a slight decrease in signal amplitude and what is observed in the experiment, where R_{MF} and R_{qu} – are specific acoustic resistance of MF and quartz.

It is necessary to pay attention to the fact that the efficiency of the operation of MF as an OA element in specialized devices depends on the stability of the OA conversion process. As shown by numerical estimates, made using tabular data, as well as experimental studies with a frequency of 10 Hz and power in a pulse ≈ 3 mJ, the greatest temporal stability of the probing signal is observed in the case when quartz glass is used as a light guide coefficient.

Some directions for using magnetic fluid as an optoacoustic converter

As mentioned above, the MF is a kind of nanomaterials with a form varying under the influence of magnetic fields, which has previously been used for both manual control and in some cases – mechanized and automated in ultrasonic flaw detection [8]. On the other hand, as shown [13], MF is a medium with a absorption coefficient, practically close to what is achieved in modern devices based on specially synthesized solid substrates with limited use. The following is a brief analysis of the possibilities of using MF for acoustic diagnostics and non-destructive testing of objects, including living (in vivo), as well as such colloids as a sensitive element for measuring the intensity of laser radiation, which is explained in Figures 4 and 5.

Figure 4 shows the constructions of OA-transducers designed to solve various practical problem. In particular, in Figure 4a, a MF thin layer performs a function of a purely flat “lining” on the probe prism converting whether in longitudinal waves transmitted to the prism for excitation in objects surface waves at the velocity of C_R , subsurface longitudinal (C_{SL}) and transverse (C_{ST}), as well as Lamb modes (C_{La}). At the same time, the

relationship between the speed of the corresponding acoustic modes, excited in the object $C_{R,SL,ST,L}$ in the OA-converter prism C_1 is $\beta = \arcsin(C_1/C_{R,SL,ST,La})$.

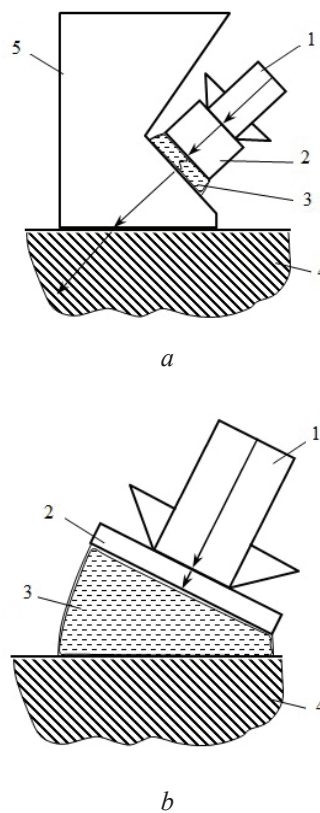


Figure 4 – Some types of optoacoustic transducers with magnetic fluid for acoustic spectroscopy and evaluation of the physico-mechanical properties of materials: 1 – laser beam; 2 – light guide; 3 – magnetic fluid; 4 – an object to test; 5 – prism of PEP

In such OA-transducers it is possible to easily change the MF free surface form under action of magnetic field, the light absorbing ability to carry out the focusing of the acoustic beam, rotate its acoustical axis in the liquid and solid materials to test them and also control the sensitivity of its arrangement when measuring the intensity of laser pulsed radiation.

In Figure 4b, the MF layer performs a function not only of the OA-transducer, but also a sound line to create acoustical contact with objects of a complex surface relief, located in difficult places, in conditions of weightlessness. Figure 4 demonstrates a method of ultrasonic testing by using of above modes the materials with an unknown or changing speed. So, it is possible to find the velocity of the corresponding mode correlating with various informative parameters and to determine the mechanical stresses

in materials, depth and distribution of hardness in hardening inhomogeneous surface layers of solids, thickness of thin coatings and walls of products of complex profile. To optimize the input of ultrasonic mode to the objects of a high-frequency pulse with minimal distortion, it is necessary to take the optimal concentration Q^* of the nanomagnetic particles, the dispersion base for magnetic fluid and its thickness. It is necessary to study influence of the MF thermal heating which affects the thermophysical and acoustic properties of colloid and measurement stability. As it was also experimentally shown earlier, a quartz with high thermal conductivity and heat capacity should be used for these purposes. It should also be noted that the further MF using as an optoacoustic material requires the study of the peculiarities of the absorption of whether in a wide range of wavelength $\lambda_l \sim 0.1\text{--}10 \mu\text{m}$ and the pulse duration $t_l \sim 0.001\text{--}1 \mu\text{s}$, and action of stationary and nonstationary magnetic fields on the generation of UW with an OA transformation.

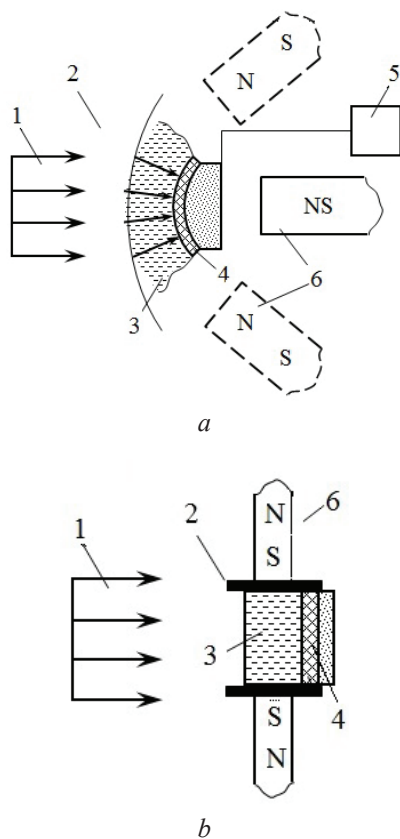


Figure 5 – Laser radiation measurement schemes, when the surface of the magnetic fluid is of quasi-spherical or quasi-cylindrical (a) or flat (b) form: 1 – laser beam; 2 – diaphragm; 3 – magnetic fluid; 4 – receiving piezoelectric element; 5 – electrical receiver; 6 – magnetic system for MF formation

One of the directions arising from the experimental studies and theoretical analysis is primarily due to the use of MF as an OA element for measuring the intensity of the laser radiation. Figure 5 shows the possible schemes that implement the method of measuring the intensity J or the laser radiation flow $\Phi(S_0)$ by placing of the MF between the PEP and hold it using the field of the magnetic source or light transparent material, and then determining of the response signal amplitude.

The advantage of the proposed method of measuring the intensity or flows of laser radiation before traditional methods lies in the simplicities of a substantial expansion of the wave length range of the laser radiation – from infrared to ultraviolet.

Conclusion

A brief analysis was carried out and the optoacoustic path was examined for the pulse-laser excitation and the propagation of longitudinal waves in the samples of magnetic fluids based on synthetic oil. The possibilities of using magnetic fluid as an object combining the function of the optoacoustic transducer and sound guide are considered.

The technique and installation that implement the shadow measurement way to study effect of the optoacoustic transformation in magnetic fluid are developed, where the Lotis-220 laser is used as a source of the laser radiation with a wavelength of $0.54 \mu\text{m}$, and the ultrasonic piezoelectric probe at a working frequency of 5 MHz to receive longitudinal waves propagating in the magnetic fluids. Amplitude dependences of the acoustic wave excited by the pulse-laser radiation are obtained v. s. the concentration of magnetic nanoparticles ($Q = 0\text{--}8 \%$) and the light pulse energy (0–10 MJ), as well as the method of transmitting the light flow in magnetic fluid through a quartz light guide and air.

The quasilinear dependence of the amplitude A^* of the OA transformation in the samples of the magnetic fluid on the pulse energy in the range from zero to $\approx 8 \text{ mJ}$ had been got. But dependences of $A^*(Q)$ have a maximum, the value and the position of which on Q -axes are determined by the boundary conditions for input the light beam in the colloid through the quartz light guide. Moreover, the value of the maximum of A^* , obtained by using a quartz guide by $\approx 40 \%$ more than in the absence of it. The interpretation of data obtained on the basis of the analysis of the thermophysical and elastic properties of magnetic fluids and light guides of contacting media.

It was shown that here are some ways for using the effect of OA transformation in magnetic fluids, including excitation of high-intensity broadband acoustic pulses of bulk, transverse, surface, etc. in solids for testing of their structure and flaw detection and to measure the power of laser radiation in a wide range of the length of the light wave.

References

1. Jean-Pierre Minchalin, Laser ultrasonics: from the laboratory to industry. *Rev. of Progress in Quantitative NDE*, 2003, no. 23A, pp. 3–31.
2. Gusev V.E., Karabutov A.A. Laser optoacaby. Moscow: Science Publ., 1991, 304 p.
3. Gurevich S.Yu., Petrov V.Yu., Golubev A.A., Shulginov A. Ema-registration of Lamb ultrasonic waves, excited by laser nano-views. *Russian Journal of Nondestructive Testing*, 2013, vol. 49, iss. 8, pp. 431–435. DOI: 10.1134/S1061830913080056
4. Khokhlova T.D., Pelivanov I.M., Karabutov A.A. Methods of optical-acoustic diagnostics of biotcaken. *Akust. journal*, 2009, vol. 55, no. 4–5, pp. 672–683.
5. Filimonova T.A., Volkov D.S., Proskurnin M.A., Pelivanov I.M. Optoacoustic spectroscopy for real-time monitoring of strongly light-absorbing solutions in applications to analytical chemistry. *Photoacoustics*, 2013, vol. 1, iss. 3–4, pp. 54–61. DOI: 10.1016/j.pacs.2013.08.002
6. Spirou G.M., Oraevsky A.A., Vitkin I.A., Whelan W.M. Optical and acoustic properties at 1064 nm of polyvinyl chloride-plastisol for use as a tissue phantom in biomedical optoacoustics. *Phys. Med. Biol.*, 2005, vol. 50, no. 14, pp. 141–153. DOI: 10.1088/0031-9155/50/14/N01
7. Blum E.Ya., Maiorov M.M., Cebers A.O. *Magnitnie jidkosti* [Magnetic fluids], Riga: Zinatne Publ., 1989, 389 p.
8. Baev A.R., Kononov G.E., Maiorov A.L. *Magnitnie jidkosti v tehnicheckoi akustike i nerazru-*
shayuschem kontrole pod red. P.P. Prohorenko [Magnetic fluids in technical acoustics and non-destructive testing ed. P.P. Prohorenko], Minsk: Tehnologiya Publ., 1999, 300 p.
9. Yong Zhao, Riqing Lv, Yuyan Zhang, Qi Wang. Novel optical devices based on the transmission properties of magnetic fluid and their characteristics. *Optics and lasers in engineering*, 2012, vol. 50, iss. 9, pp. 1177–1184. DOI: 10.1016/j.optlaseng.2012.03.012
10. Yang X., Liu Y., Zheng Y., Li S., Yuan L., Yuan T., Tong C. A capillary optical fiber modulator derivates from magnetic fields. *Optics Communications*, 2013, vol. 304, pp. 83–86. DOI: 10.1016/j.optcom.2013.04.038
11. Yong Zhao, Yuyan Zhang, Riqing Lv, Qi Wang. Novel optical devices based on the tunable refractive index of magnetic fluid and their characteristics. *J. Mag. Mater.*, 2011, vol. 323, iss. 23, pp. 2987–2996. DOI: 10.1016/j.jmmm.2011.06.025
12. Li Y., Zhang H., Yang Z., Yuan B., Yuan Z., Xue H. Incident-power-dependent optical transmission properties of magnetic fluid films. *Optik.*, 2018, vol. 172, pp. 730–735. DOI: 10.1016/j.ijleo.2018.07.042
13. Baev A.R., Karabutov A. A., Podimova N.B., Prohorenko P.P. *Osobennosti vozbuždeniya uprugih voln v magnitnih jidkostyah lazernim izlucheniem* [Features of excitation of elastic waves in magnetic liquids by laser radiation]. *Magnitnaya gidrodinamika* [Magnetic gtdrodynamics], 1996, no. 3, pp. 23–30 (in Russian).
14. Sokolovskaya Yu. G., Podimova N.B., Karabutov A.A. *Issledovanie strukturnoj neodnorodnosti magnitnoj zhidkosti posredstvom vosstanovleniya prostranstvennogo raspredeleniya koefficienta ekstinkcii sveta s ispol'zovaniem lazernogo optiko-akusticheskogo metoda* [Investigation of the structural inhomogeneity of a magnetic fluid by reconstructing the spatial distribution of the extinction coefficient of light using a laser optical-acoustic method]. *Akusticheskij zhurnal* [Acoustic], 2020, vol. 66, no. 3, pp. 284–293. DOI: 10.31857/S0320791920030065

Digital Spectral Analysis by means of the Method of Averag Modified Periodograms Using Binary-Sign Stochastic Quantization of Signals

V.N. Yakimov

Samara State Technical University,
Molodogvardeyskaya str., 244, Samara 443100, Russia

Received 24.06.2021

Accepted for publication 10.09.2021

Abstract

The method of averaging modified periodograms is one of the main methods for estimating the power spectral density (PSD). The aim of this work was the development of mathematical and algorithmic support, which can increase the computational efficiency of signals digital spectral analysis by this method.

The solution to this problem is based on the use of binary-sign stochastic quantization for converting the analyzed signal into a digital code. A special feature of this quantization is the use of a randomizing uniformly distributed auxiliary signal as a stochastic continuous quantization threshold (threshold function). Taking into account the theory of discrete-event modeling the result of binary-sign quantization is interpreted as a chronological sequence of instantaneous events in which its values change. In accordance with this we have a set of time samples that uniquely determine the result of binary-sign quantization in discrete-time form. Discrete-event modeling made it possible to discretize the process of calculating PSD estimates. As a result, the calculation of PSD estimates was reduced to discrete processing of the cosine and sine Fourier transforms for window functions. These Fourier transforms are calculated analytically based on the applied window functions. The obtained mathematical equations for calculating the PSD estimates practically do not require multiplication operations. The main operations of these equations are addition and subtraction. As a consequence, the time spent on digital spectral analysis of signals is reduced.

Numerical experiments have shown that the developed mathematical and algorithmic support allows us to calculate the PSD estimates by the method of averaging modified periodograms with a high frequency resolution and accuracy even for a sufficiently low signal-to-noise ratio. This result is especially important for spectral analysis of broadband signals.

The developed software module is a problem-oriented component that can be used as part of metrologically significant software for the operational analysis of complex signals.

Keywords: spectral analysis, Fourier transform, modified periodogram method, binary stochastic quantization, fast algorithms.

DOI: 10.21122/2220-9506-2021-12-3-220-229

Адрес для переписки:

Якимов В.Н.
Самарский государственный технический университет,
ул. Молодогвардейская, 244, г. Самара 443100, Россия
e-mail: yvnr@hotmail.com

Address for correspondence:

Yakimov V.N.
Samara State Technical University,
Molodogvardeyskaya str., 244, Samara 443100, Russia
e-mail: yvnr@hotmail.com

Для цитирования:

V.N. Yakimov.
Digital Spectral Analysis by means of the Method of Averag Modified Periodograms Using Binary-Sign Stochastic Quantization of Signals.
Приборы и методы измерений.
2021. – Т. 12, № 3. – С. 220–229.
DOI: 10.21122/2220-9506-2021-12-3-220-229

For citation:

V.N. Yakimov.
Digital Spectral Analysis by means of the Method of Averag Modified Periodograms Using Binary-Sign Stochastic Quantization of Signals.
Devices and Methods of Measurements.
2021, vol. 12, no. 3, pp. 220–229.
DOI: 10.21122/2220-9506-2021-12-3-220-229

Цифровой спектральный анализ методом усреднённых модифицированных периодограмм с применением бинарно-знакового стохастического квантования сигналов

В.Н. Якимов

Самарский государственный технический университет,
ул. Молодогвардейская, 244, г. Самара 443100, Россия

Поступила 24.06.2021

Принята к печати 10.09.2021

Метод усреднённых модифицированных периодограмм является одним из основных методов оценивания спектральной плотности мощности (СПМ). Целью работы являлась разработка математического и алгоритмического обеспечения, которые позволяют повысить вычислительную эффективность цифрового спектрального анализа сигналов этим методом.

Решение поставленной задачи основано на использовании бинарно-знакового стохастического квантования для преобразования анализируемого сигнала в цифровой код. Особенностью такого квантования является применение рандомизирующего равномерно распределённого вспомогательного сигнала в качестве стохастического непрерывного порога квантования (пороговой функции). С учётом теории дискретно-событийного моделирования результат бинарно-знакового квантования интерпретируется как хронологическая последовательность мгновенных событий, в которые происходит смена его значений. В соответствии с этим, имеем множество отсчётов времени, которые однозначно определяют результат бинарно-знакового квантования в дискретном виде. Дискретно-событийное моделирование позволило осуществить дискретизацию процесса вычисления оценок СПМ. В итоге вычисление оценок СПМ свелось к дискретной обработке косинус и синус преобразований Фурье для оконных функций. Эти преобразования Фурье вычисляются аналитически с учётом применяемых оконных функций. Полученные математические соотношения для вычисления оценок СПМ практически не требуют выполнения операций умножения. Основными операциями этих соотношений являются операции сложения и вычитания. Следствием этого является уменьшение временных затрат на цифровой спектральный анализ сигналов.

Численные эксперименты показали, что разработанное математическое и алгоритмическое обеспечение позволяет вычислять оценки СПМ методом усреднённых модифицированных периодограмм с высоким частотным разрешением и точностью даже для достаточно низкого отношения сигнал/шум. Такой результат особенно важен для спектрального анализа широкополосных сигналов.

Разработанный программный модуль представляет собой проблемно-ориентированный компонент, который может использоваться в составе метрологически значимого программного обеспечения для оперативного анализа сложных сигналов.

Ключевые слова: спектральный анализ, преобразование Фурье, метод модифицированных периодограмм, бинарное стохастическое квантование, быстрые алгоритмы.

DOI: 10.21122/2220-9506-2021-12-3-220-229

Адрес для переписки:

Якимов В.Н.
Самарский государственный технический университет,
ул. Молодогвардейская, 244, г. Самара 443100, Россия
e-mail: yvnr@hotmail.com

Address for correspondence:

Yakimov V.N.
Samara State Technical University,
Molodogvardeyskaya str., 244, Samara 443100, Russia
e-mail: yvnr@hotmail.com

Для цитирования:

V.N. Yakimov.
Digital Spectral Analysis by means of the Method of Averag Modified Periodograms Using Binary-Sign Stochastic Quantization of Signals. Приборы и методы измерений. 2021. – Т. 12, № 3. – С. 220–229.
DOI: 10.21122/2220-9506-2021-12-3-220-229

For citation:

V.N. Yakimov.
Digital Spectral Analysis by means of the Method of Averag Modified Periodograms Using Binary-Sign Stochastic Quantization of Signals. *Devices and Methods of Measurements*. 2021, vol. 12, no. 3, pp. 220–229.
DOI: 10.21122/2220-9506-2021-12-3-220-229

Introduction

Spectral analysis is one of the most significant and applied methods for signal investigation. It is used in many areas of engineering and physical sciences. In particular, the spectral estimation of the frequency composition of signals is of practical interest in the process of non-destructive testing and functional diagnostics of technical systems used for various purposes.

In real life signals are exposed to random disturbances and noise interference which leads to their statistical uncertainty. Statistical analysis methods are used to investigate such noisy signals. In this case, the spectral analysis of signals will be associated with the need to obtain a robust estimate of the power spectral density (PSD).

PSD is a continuous function of frequency and determines the average power per unit frequency interval. Estimation of PSD allows us to get an idea of the distribution of the average signal power in the monitored frequency range and to identify within this range the dominant (resonant) frequency components present in its composition. In practice, the PSD is estimated based on the calculation of the direct Fourier transform. Currently, the discrete Fourier transform is used. This is due to the advantages of digital signal processing. First of all, such advantages are the repeatability and reproducibility of digital measuring procedures [1].

With the advent of powerful computer technology and as a result of the development of fast Fourier transform algorithms the periodogram method for estimating the PSD is widely used. According to this method, if the signal is stationary and ergodic in time, then the PSD estimate is calculated by processing single of its centered realization using the finite Fourier transform [2, 3]. Centering the signal realization implies preliminary removal of the constant component, if any. However, it was shown in [3] that such a periodogram estimate of the PSD will yield statistically unstable results of spectral analysis. At the same time, an increase in the duration of the processed signal realization does not improve the quality of the PSD estimate. This only leads to an increase in the number of frequencies for which the PSD estimate can be calculated. The smoothing of the PSD estimate can be obtained by averaging the periodogram estimates calculated for individual segments of the signal realization under the assumption that it is stationary. In this case, the observed realization of

the signal is divided into segments of finite duration, which form a pseudo-ensemble. Local periodogram estimates are calculated for these segments. Finally, the PSD estimate is calculated by averaging the local periodograms. If the duration of the signal realization is limited in time, then the formation of a pseudo-ensemble with partial overlapping of segments is allowed. This allows you to get more periodogram local estimates for averaging. In order to reduce spectral leakage and reduce distortion of periodogram estimates by strong harmonics, each segment is processed using windowed weighting operations. This reduces the level of side lobes in the spectrum estimate. In addition, the use of windowing functions gives less weight to the values at the ends of the segments. As a result, the overlapping segments are less correlated with each other, which make it possible to obtain a more effective variance reduction for averaged periodogram estimates. This approach to estimating the PSD is known as the method of averaging modified periodograms [2–5].

The method of averaging modified periodograms leads to a decrease in the variance of the calculated PSD estimates. It also allows you to control the level of the side lobes, which is especially important when the amplitudes of the harmonics in the signal vary greatly. However, this method is a complex signal processing procedure. The need to carry out such complex signal processing leads to the fact that classical algorithms implementing this method in digital form assume the organization of computational processes that require performing a significant number of digital multiplication operations. It is known that it is the multiplication operations that are the most computationally laborious among all arithmetic operations [6, 7]. The execution of such algorithms can lead to significant time costs and reduce the efficiency of signal processing, even if the fast Fourier transform is used. The development and use of increasingly powerful computer technology cannot solve this problem completely. This is due to the constant complication of technological processes for monitoring and diagnosing complex systems and objects, which leads to the need to analyze large amounts of data sets. In accordance with the above, the aim of this work was the development of mathematical and algorithmic support, which can increase the computational efficiency of signals digital spectral analysis by the method of averaging modified periodograms. It is necessary to note, that a positive solution to this problem can be obtained

by reducing the number of digital multiplication operations.

Estimation of the power spectral density based on binary-sign stochastic quantization

Currently widely used digital algorithms for calculating periodogram estimates of PSD are traditionally developed on the basis of the classical approach to the discrete-time representation of signals. According to this approach, analog-to-digital signal conversion is the result of performing uniform time sampling, multi-level quantization, and encoding of the digitized samples. Such analog-to-digital conversion leads to the necessity of processing multi-bit samples of digital signals in the process of spectral analysis. In practice, in order to reduce time costs, it is necessary to make trade-offs between the quality of analog-to-digital conversion and the computational complexity of processing digital samples. In the extreme case, binary quantization methods are used to convert signals into a digital code [8–14].

Randomization (deliberate introduction of randomness) of binary quantization makes it possible to obtain a rational relationship between an extremely low number of quantization levels equal to two and the accuracy characteristics of computational algorithms in digital signal processing. In the case of using randomization, we have binary stochastic quantization. A special case of such quantization is binary-sign stochastic quantization. The use of binary-sign stochastic quantization for the statistical analysis of signals is substantiated in [15]. In the process of performing such quantization, a continuous auxiliary random signal is used as a variable quantization threshold (threshold function). The auxiliary signal takes on values within the values range of the analyzed signal and has a uniform distribution. The result of the binary-sign stochastic quantization is:

$$z(t) = +1, \text{ if } \overset{o}{x}(t) \geq \xi(t); \quad z(t) = -1, \text{ if } \overset{o}{x}(t) < \xi(t), \quad (1)$$

where $\overset{o}{x}(t)$ is a centered signal realization; $\xi(t)$ auxiliary random signal.

The result of binary-sign stochastic quantization can only take on the value “-1” or “+1”. The change of these values occurs sequentially at the moments of time t_i^Z . At the same time, the probability of simultaneous occurrence of two or more events at the same time is excluded. Taking this into account, a

mathematical model was obtained for representing $z(t)$ in discrete form [16]. It is developed based on the theory of discrete-event modeling. According to this model, it is enough for us to know only the initial value of the binary-sign quantization result $z(t_0)$ and the set of time samples t_i^Z within the time interval of signal analysis. Based on this model, the calculation of the periodogram estimate of the PSD using binary-sign stochastic quantization is considered in [17, 18]. However, the mathematical equations obtained in [17] do not provide for the use of window functions. In [18], the periodogram estimate of the PSD is calculated using window functions, but its calculation is carried out indirectly through the calculation of the correlation function estimate. This approach to the estimation of PSD requires the formation of initial data using two independent procedures of binary-sign stochastic quantization, which complicates the procedure of spectral analysis.

Taking into account the results obtained by the author in [16–18], we consider the application of binary-sign stochastic quantization for estimating PSD by the method of averaging modified periodograms. According to this method, the result of binary-sign stochastic quantization should be represented as a pseudo-ensemble of signal segments. For these segments, local periodogram estimates are calculated, which are averaged to obtain the desired PSD estimate.

Figure 1 shows a pseudo-ensemble consisting of M segments for the result of a binary-sign stochastic quantization. The duration of each segment is $T = L\Delta T$, where L is the number of overlapping pieces of the segment, and ΔT is the segment shift. For the pseudo-ensemble shown in Figure 1 $L = 2$. If we assume that $t_0 = 0$, then mathematically in time, the segments can be represented as follows:

$$z(m, t) = z(t + (m-1)\Delta T), \quad (2)$$

where $0 \leq t \leq T$ and $1 \leq m \leq M$.

The periodogram estimate for the each weighted segment we will calculate with a frequency resolution $f_0 = T^{-1}$ at frequencies $f_k = kf_0$:

$$\hat{S}_{XX}(m, f_k) = \frac{\xi_{\max}^2}{TW} \left| \int_0^T z(t + (m-1)\Delta T) w(t) \exp(-j2\pi k f_0 t) dt \right|^2, \quad (3)$$

where $w(t)$ is a window function; W characterizes the average power of the window function and is a normalizing factor.

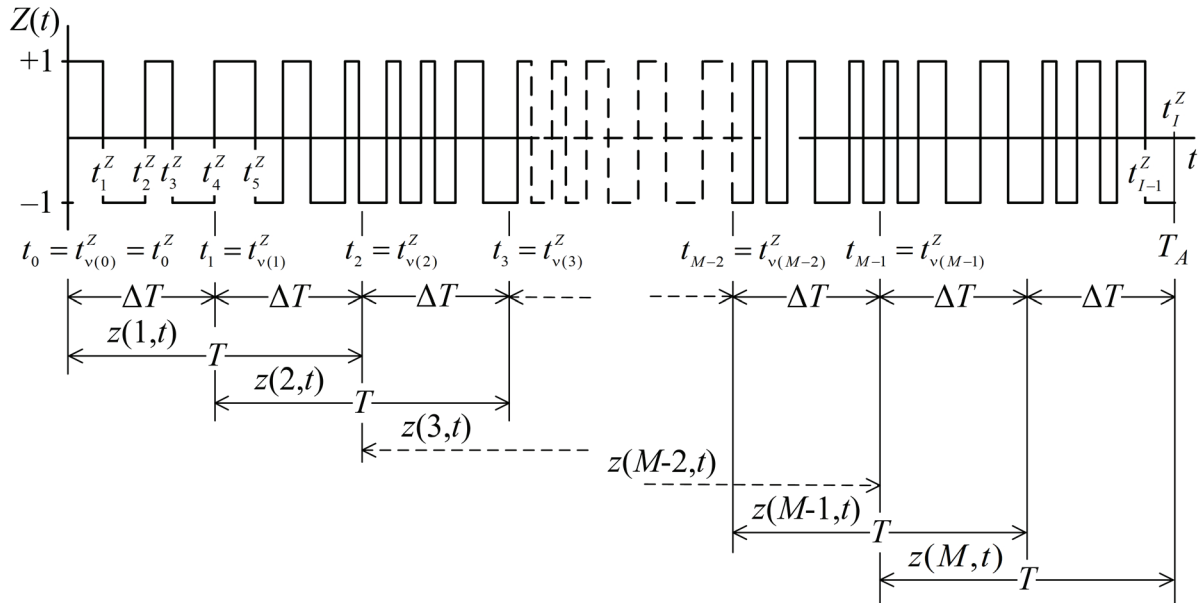


Figure 1 – Segments pseudo-ensemble of the binary-sign stochastic quantization result

The averaged periodogram estimate of the PSD will be equal to:

$$\hat{S}_{XX}(f_k) = \frac{1}{M} \sum_{m=1}^M \hat{S}_{XX}(m, f_k). \quad (4)$$

We represent (3) in the following form:

$$\hat{S}_{XX}(m, f_k) = \frac{\xi_{\max}^2}{TW} (\hat{a}_{k,m}^2 + \hat{b}_{k,m}^2), \quad (5)$$

where

$$\hat{a}_{k,m} = \int_0^T z(t + (m-1)\Delta T) w(t) \cos 2\pi k f_0 t dt; \quad (6)$$

$$\hat{b}_{k,m} = \int_0^T z(t + (m-1)\Delta T) w(t) \sin 2\pi k f_0 t dt. \quad (7)$$

Let's introduce the functions:

$$h_{\cos}(f, t) = w(t) \cos 2\pi f t; \quad (8)$$

$$h_{\sin}(f, t) = w(t) \sin 2\pi f t. \quad (9)$$

Then for (6) and (7) we get:

$$\hat{a}_{k,m} = \int_{t_{m-1}}^{t_{m-1}+T} z(t) h_{\cos}(f_k, t - t_m) dt; \quad (10)$$

$$\hat{b}_{k,m} = \int_{t_{m-1}}^{t_{m-1}+T} z(t) h_{\sin}(f_k, t - t_m) dt, \quad (11)$$

where $t_0 = 0$; $t_m = m\Delta T$; $1 \leq m \leq M$.

Taking into account the discrete-event model developed in [16], any segment $z(m, t)$ can be represented in a discrete-time form. As a result of performing binary-sign quantization, we have the initial value $z(t_0)$ and a set of time samples t_i^Z , in which its values change during the analysis time interval T_A , where $1 \leq i \leq I-1$, $t_0^Z = t_0 = 0$ and $t_I^Z = T_A$. To uniquely identify a segment $z(m, t)$ in time, it is enough to know the set of time samples t_i^Z on the time interval $t_{m-1} \leq t \leq (t_{m-1} + T)$ within

which this segment is defined, and you also need to know its initial value $z(t_{m-1})$. The result of binary-sign quantization $z(t)$ sequentially takes on the values “-1” and “+1”. Therefore, if its initial value $z(t_0)$ is known, then the initial value $z(t_{m-1})$ for the segment $z(m, t)$ can be easily determined. Based on this, we introduce the notation $t_{v(m)}^Z = t_{m-1}$ and $t_{v(m)+r(m)+1}^Z = t_{m-1} + T$. The subscripts $v(m)$ and $r(m)$ are integers. Such designations of these indices show their dependence on the segment number. Then for the segment $z(m, t)$ we will have the set of time samples:

$$\{t_{v(m)+1}^Z, t_{v(m)+2}^Z, \dots, t_{v(m)+j}^Z, \dots, t_{v(m)+r(m)}^Z\} \in [t_{m-1}; t_{m-1} + T]. \quad (12)$$

At time intervals, the boundaries of which are determined by the counts (12), the values for $z(t)$ are equal to “-1” or “+1”. Therefore, the integrals in (10) and (11) can be represented as a sum of integrals:

$$\hat{a}_{k,m} = z(t_{m-1}) \sum_{j=0}^{r(m)} (-1)^j \int_{t_{v(m)+j}^Z}^{t_{v(m)+j+1}^Z} h_{\cos}(f_k, t - t_{m-1}) dt; \quad (13)$$

$$\hat{b}_{k,m} = z(t_{m-1}) \sum_{j=0}^{r(m)} (-1)^j \int_{t_{v(m)+j}^Z}^{t_{v(m)+j+1}^Z} h_{\sin}(f_k, t - t_{m-1}) dt. \quad (14)$$

A window $w(t)$ function is a continuous and integrable function. Therefore, the functions $h_{\cos}(f, t)$ and $h_{\sin}(f, t)$ will also be continuous and integrable with respect to the time variable. Consequently, there are functions for $H_{\cos}(f, t)$ and $H_{\sin}(f, t)$ which the differentiability conditions are satisfied:

$$dH_{\cos}(t, f) = h_{\cos}(t, f) dt; \quad (15)$$

$$dH_{\sin}(t, f) = h_{\sin}(t, f) dt. \quad (16)$$

Taking into account (15) and (16), the integrals in (13) and (14) are calculated analytically:

$$\hat{a}_{k,m} = z(t_{m-1}) \left(\alpha_{k,m} + 2 \sum_{j=1}^{r(m)} (-1)^j H_{\cos}(f_k, t_{v(m)+j}^Z - t_{m-1}) \right); \quad (17)$$

$$\hat{b}_{k,m} = z(t_{m-1}) \left(\beta_{k,m} + 2 \sum_{j=1}^{r(m)} (-1)^j H_{\sin}(f_k, t_{v(m)+j}^Z - t_{m-1}) \right). \quad (18)$$

where

$$\alpha_{k,m} = H_{\cos}(f_k, 0) - (-1)^{r(m)} H_{\cos}(f_k, T); \quad (19)$$

$$\beta_{k,m} = H_{\sin}(f_k, 0) - (-1)^{r(m)} H_{\sin}(f_k, T). \quad (20)$$

According to (5), when calculating the periodogram estimate of the PSD for the segment $z(m, t)$, the coefficients estimates (17) and (18) must be squared. In this case, we get $z^2_{(t-1)} = 1$. It follows that there is no need to know the initial values $z_{(t-1)}$ of the segments. It is enough to have only a set of time samples t_i^Z in which the result of binary-sign stochastic quantization changes its values in the time interval of spectral analysis. This greatly simplifies the computational procedures for estimating the PSD. With this in mind, it is sufficient to calculate the estimates of the following form:

$$\hat{A}_{k,m} = \alpha_{k,m} + 2 \sum_{j=1}^{r(m)} (-1)^j H_{\cos}(f_k, t_{v(m)+j}^Z - t_{m-1}); \quad (21)$$

$$\hat{B}_{k,m} = \beta_{k,m} + 2 \sum_{j=1}^{r(m)} (-1)^j H_{\sin}(f_k, t_{v(m)+j}^Z - t_{m-1}). \quad (22)$$

Then we get:

$$\hat{S}_{XX}(m, f_k) = \frac{\xi_{\max}^2}{TW} (\hat{A}_{k,m}^2 + \hat{B}_{k,m}^2). \quad (23)$$

Equations (4) and (19)–(23) define a set of computational procedures and the order of their execution for calculating PSD estimates $\hat{S}_{XX}(f_k)$ in digital form at discrete frequencies $fk = kf_0$. It follows from (21) and (22) that the basis of these procedures are logical operations for organizing the execution of a sequence of actions and operations for adding and subtracting function values $H_{\cos}(f, t)$ and $H_{\sin}(f, t)$ for $f = kf_0$ and $t = t_i^Z$.

Numerical experiments

Based on (4) and (19)–(23), the author has developed algorithmic support and software for calculating the PSD estimate by the method of averaging modified periodograms. The software is made in the form of a specialized software module that can be used as part of a metrologically significant part of the application software for complex signal analysis [19]. When conducting spectral analysis of signals, it should be borne in mind that none of the existing window functions is universal in its purpose. The choice of a specific window function is due to the task and conditions in which the spectral analysis of signals is carried out. Analysis of frequency and metrological characteristics of window functions and recommendations for their application are presented in [20–22]. In our case, for the selected window function, it is necessary to have the functions $H_{\cos}(f, t)$ and $H_{\sin}(f, t)$. By definition, these functions are calculated analytically. Therefore, depending on which window functions are supposed to be used, a set of corresponding functions $H_{\cos}(f, t)$ and $H_{\sin}(f, t)$ can be pre-formed and arranged in the form of special collections or libraries of application routines. As an example, we will consider three widely used window functions in practice: rectangular (box car) window, triangular window (Bartlett's) and cosine window. Below for these window functions are the functions $H_{\cos}(f, t)$ and $H_{\sin}(f, t)$, the values of which for $t = 0$ and $t = T$ are shown in Table 1.

1) Rectangular window (box car):

$$w(t) = \begin{cases} 1, & |t| \leq T; \\ 0, & |t| > T. \end{cases}$$

$$H_{\cos}(f, t) = \frac{\sin 2\pi ft}{2\pi f}; \quad H_{\sin}(f, t) = -\frac{\cos 2\pi ft}{2\pi f}.$$

2) Triangular window (Bartlett's):

$$w(t) = \begin{cases} 1 - \frac{|t|}{T}, & |t| \leq T; \\ 0, & |t| > T. \end{cases}$$

$$H_{\cos}(f, t) = \left(1 - \frac{t}{T}\right) \frac{\sin 2\pi ft}{2\pi f} - \frac{1}{T} \frac{\cos 2\pi ft}{(2\pi f)^2};$$

$$H_{\sin}(f, t) = -\left(1 - \frac{t}{T}\right) \frac{\cos 2\pi ft}{2\pi f} - \frac{1}{T} \frac{\sin 2\pi ft}{(2\pi f)^2}.$$

3) Cosine window:

$$w(t) = \begin{cases} \cos \frac{\pi t}{2T}, & |t| \leq T; \\ 0, & |t| > T. \end{cases}$$

$$H_{\cos}(f, t) = \frac{\sin 0.5\pi(4f - f_0)t}{\pi(4f - f_0)} + \frac{\sin 0.5\pi(4f + f_0)t}{\pi(4f + f_0)};$$

$$H_{\sin}(f, t) = -\left(\frac{\cos 0.5\pi(4f - f_0)t}{\pi(4f - f_0)} + \frac{\cos 0.5\pi(4f + f_0)t}{\pi(4f + f_0)}\right).$$

Table 1

The values of the functions $H_{\cos}(f, t)$ and $H_{\sin}(f, t)$ for the rectangular (box car), triangular (Bartlett's) and cosine windows at $t = 0$ and $t = T$, when $fk = kf_0$ and $f_0 = T^{-1}$

Window	$H_{\cos}(f_k, 0)$	$H_{\cos}(f_k, T)$	$H_{\sin}(f_k, 0)$	$H_{\sin}(f_k, T)$
Rectangular (box car)	0	0	$-\frac{T}{2\pi k}$	$-\frac{T}{2\pi k}$
Triangular (Bartlett's)	$-\frac{T}{(2\pi k)^2}$	$-\frac{T}{(2\pi k)^2}$	$-\frac{T}{2\pi k}$	0
Cosine	0	$-\frac{2T}{\pi(16k^2 - 1)}$	$-\frac{8kT}{\pi(16k^2 - 1)}$	0

Investigations of the computational properties of the developed algorithm for estimating the PSD were carried out on the basis of planning and carrying out numerical experiments. For this purpose, sets of test signal models were used. Each of these models simulated a noisy implementation of a centered signal $x(t)$ with a given frequency spectrum structure. The structural composition of the frequency spectrum of the signal model was specified using a combination of summed harmonic components included in its composition. The frequency values of the harmonic components were set in relative units and varied in the range from zero to 0.5. Taking into account the Nyquist–Shannon theorem, they were interpreted as normalized with respect to the doubled value of the upper limit of the frequency band that the spectrum is supposed to occupy. The amplitudes of the harmonic components A_n were set in the range from zero to one. Random initial phases φ_n were set in the range from $-\pi$ to $+\pi$ using a generator of evenly distributed numbers. The sum of the harmonic components was subject to noise. This was achieved by generating white noise that had a zero mean value. The dispersion σ_e^2 of white noise was set during the experiment. We considered

the signal-to-noise ratio as the ratio of the power of each harmonic component to the noise power. This simulation approach allowed us to investigate the ability to detect harmonic components in noise.

As an example, let's consider the case when the signal model contained nine harmonic components. The numerical values of the frequencies and amplitudes of these harmonic components are presented in Table 2.

Table 2

Parameters for harmonic components of the signal realization model

n	A_n	f_n	$A_n^2 / A_{\max}^2, \text{dB}$
1	0.1	0.1	-20.00
2	0.15	0.12	-16.48
3	0.7	0.15	-3.10
4	1.0	0.2	0.00
5	0.5	0.22	-6.02
6	0.35	0.25	-9.12
7	0.25	0.27	-12.04
8	0.2	0.3	-13.98
9	0.05	0.35	-26.02

The variance σ_e^2 of the additive noise was equal to unity. The procedure for obtaining time samples t_i^Z of the result of binary-sign stochastic quantization for the signal model $x(t)$ and the formation of a

segments pseudo-ensemble based on them was carried out using discrete-event simulation. The normalized PSD estimates calculated for this signal model are shown in Figures 2–4.

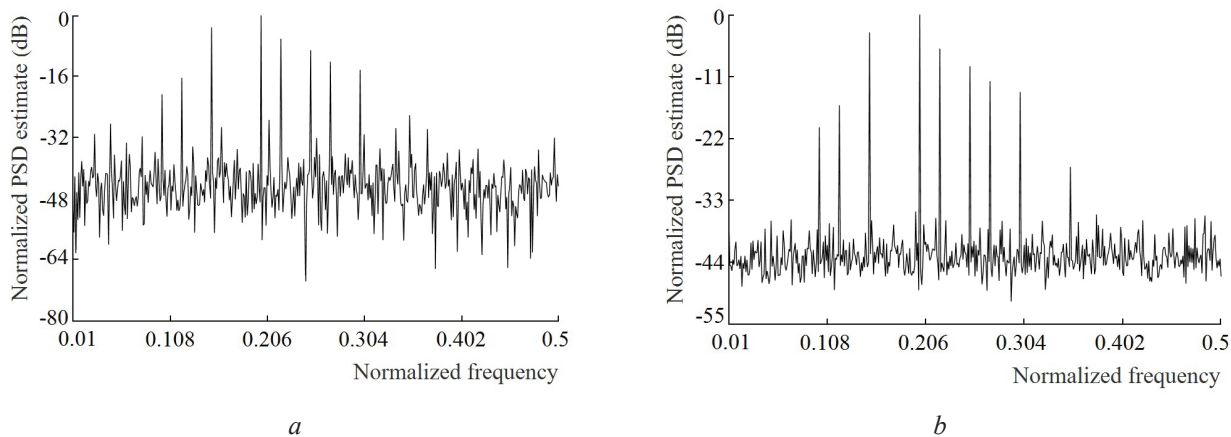


Figure 2 – Normalized power spectral density estimate, rectangular window (box car): *a* – one segment; *b* – ten segments

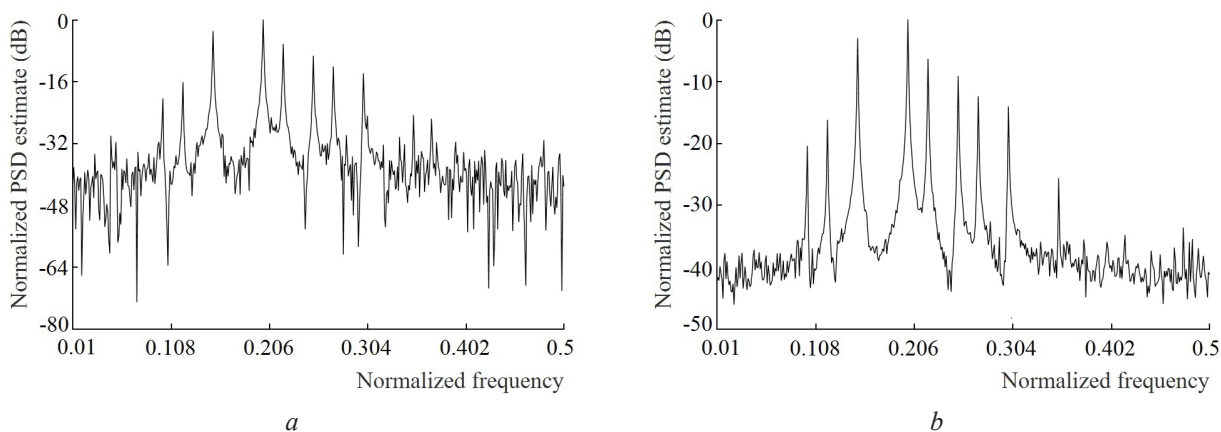


Figure 3 – Normalized power spectral density estimate, triangular window (Bartlett's): *a* – one segment; *b* – ten segments

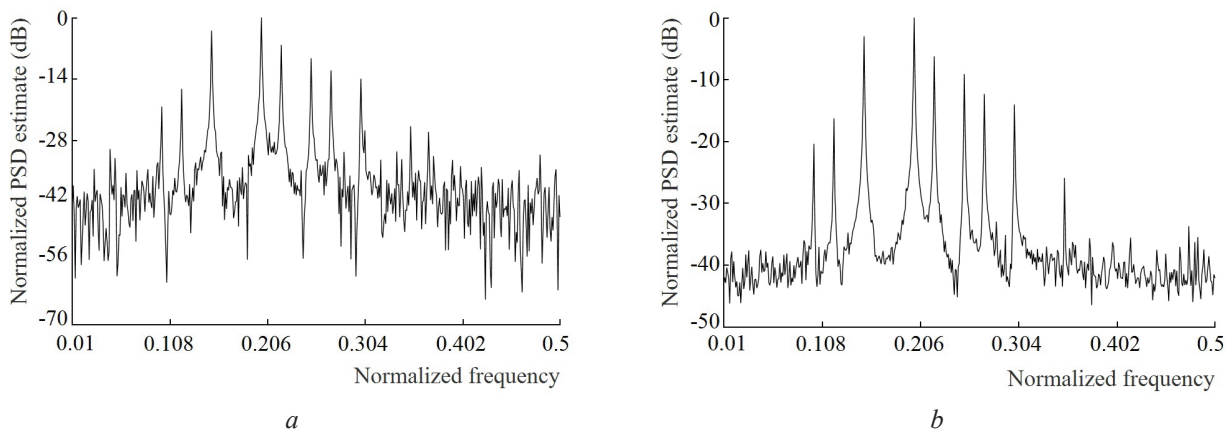


Figure 4 – Normalized power spectral density estimate, cosine window: *a* – one segment; *b* – ten segments

They were calculated with a resolution of 0.0005 conventional units of the normalized frequency within the entire analysis range from zero to 0.5. For each of the three window functions, the PSD estimates were calculated for one and ten segments. The overlap of the segments was half their length. For the PSD estimates calculated for one segment, we observe the presence of significant fluctuations relative to the true values of the frequency components. At the same time, it is difficult for us to identify the presence of weak harmonic components in the spectrum, for which the signal-to-noise ratio is rather low. In particular, the harmonic component with a frequency of 0.35 and amplitude of 0.05 is masked by noise. It is clearly seen that an increase in the number of processed segments leads to an improvement in the quality of PSD estimates and a decrease in the level of additive noise. All nine frequency components are present on the graphs of PSD estimates calculated for ten segments. The weaker harmonic components are clearly visible and their position in the spectrum corresponds to the tabular data. There are no false spectral lines.

Conclusion

The paper considers the development of mathematical and algorithmic support that allows increasing the computational efficiency of estimating the PSD by the method of averaging modified periodograms in discrete form. This development was carried out on the basis of the use of binary-sign stochastic quantization to obtain the digital code of the analyzed signal. A discrete-event model is used to represent the result of binary-sign stochastic quantization in time. This model allowed us to reduce the calculation of PSD estimates to discrete processing of functions that are the result of cosine and sine Fourier transforms for window functions. A set of such functions can be formed beforehand, depending on the window functions used. As a result, we obtained mathematical equations for calculating PSD estimates in discrete form, which do not require performing numerous multiplication operations. These equations became the basis for the development of computational algorithms for estimating the PSD. The main computational operations of the algorithms are the operations of algebraic addition and subtraction. The practical implementation of these algorithms leads to a decrease in computational and time costs in the process of estimating the PSD.

Numerical experiments were carried out on the basis of simulation modeling. They showed that the developed approach to solving the problem posed provides the estimation of PSD by averaging modified periodograms with high frequency resolution. Reliable identification of spectral components is ensured even in additive noise when the signal-to-noise ratio is sufficiently low. This result is especially important for the analysis of broadband signals.

The practical result was the development of a problem-oriented software module for spectral analysis. This module can be used as part of metrologically significant software for the operational analysis of complex signals.

Acknowledgments

This work was supported by the Russian Foundation for Basic Research (RFBR) under initiative research project No. 19-08-00228-A.

References

1. Oppenheim A.V., Schaffer R.W. Discrete-time signal processing: Third edition. Pearson Higher Education, 2010, 1108 p.
2. Alessio S.M. Digital signal processing and spectral analysis for scientists: Concepts and applications. Springer, 2016, 900 p.
3. Marple Jr.S.L. Digital spectral analysis with applications: Second edition. Dover Publications Inc., 2019, 432 p.
4. Welch P. The Use of Fast Fourier Transform for the Estimation of Power Spectra: A Method Based on Time Averaging Over Short, Modified Periodograms. *IEEE Transactions on Audio and Electroacoustics*, 1967, vol. 15, no. 2, pp. 70–73.
DOI: 10.1109/TAU.1967.1161901
5. Manolakis D.G., Ingle V.K. Applied Digital Signal Processing: Theory and Practice. Cambridge University Press, 2011, 1009 p.
6. Britanak V., Rao K.R. Cosine-/Sine-Modulated Filter Banks. General Properties, Fast Algorithms and Integer Approximations. *Springer International Publishing*, 2018, XXVI, 645 p.
DOI: 10.1007/978-3-319-61080-1
7. Chu E. Discrete and Continuous Fourier Transforms: Analysis, Applications and Fast Algorithms. CRC Press, 2008, XXIII, 400 p.
8. Papadopoulos H.C., Wornell G.W., Oppenheim A.V. Sequential signal encoding from noisy measurements using quantizers with dynamic bias control.

IEEE Transactions on information theory, 2001, vol. 47, no. 3, pp. 978–1002. **DOI:** 10.1109/18.915654

9. Fang J., Shen Y., Yang L., Li H. Adaptive one-bit quantization for compressed sensing. *Signal Processing*, 2016, vol. 125, pp. 145–155.

DOI: 10.1016/j.sigpro.2016.01.020

10. Isla J., Celga F. The use of binary quantization for the acquisition of low SNR ultrasonic signals: a study of the input dynamic range. *IEEE Transactions on Ultrasonics, Ferroelectrics, and Frequency Control*, 2016, vol. 63, no. 9, pp. 1474–1482.

DOI: 10.1109/TUFFC.2016.2571843

11. Zhai Q., Wang Y. Noise effect on signal quantization in an array of binary quantizers. *Signal Processing*, 2018, vol. 152, pp. 265–272.

DOI: 10.1016/j.sigpro.2018.06.010

12. Diao J.-D., Guo J., Sun C.-Y. Event-triggered identification of fir systems with binary-valued output observations. *Automatica*, 2018, vol. 98, pp. 95–102.

DOI: 10.1016/j.automatica.2018.09.024

13. Wang G., Zhu J., Xu Z. Asymptotically optimal one-bit quantizer design for weak-signal detection in generalized Gaussian noise and lossy binary communication channel. *Signal Processing*, 2019, vol. 154, pp. 207–216. **DOI:** 10.1016/j.sigpro.2018.09.005

14. Mei H., Wang L.Y., Yin G. Almost sure convergence rates for system identification using binary, quantized, and regular sensors. *Automatica*, 2014, vol. 50, no. 8, pp. 2120–2127.

DOI: 10.1016/j.automatica.2014.05.036

15. Max J. Methodes et techniques de traitement du signal et applications aux mesures physiques. Tome 1: Principes generaux et methodes classiques. Paris, Masson, 1996, 354 p.

16. Yakimov V.N. [Digital complex statistical analysis based on the sign-function representation of random processes]. *Izvestija samarskogo nauchnogo centra Rossijskoj akademii nauk* [Izvestia of Samara scientific center of the Russian academy of sciences], 2016, vol. 18, no. 4(7), pp. 1346–1353 (in Russian).

17. Yakimov V.N. Direct spectral power density estimation from a discrete-time representation of stochastic analog quantization for an analog random process. *Measurement Techniques*, 2009, vol. 52, no. 3, pp. 223–230.

DOI: 10.1007/s11018-009-9262-y

18. Yakimov V.N., Mashkov A.V. [Algorithm to compute estimate of a power spectral density based on sign signal processing using time-weighting functions]. *Tsifrovaya obrabotka signalov* [Digital Signal Processing], 2016, no. 4, pp. 3–8 (in Russian).

19. Yakimov V.N., Gorbachev O.V. Firmware of the amplitude spectrum evaluating system for multi-component processes. *Instruments and Experimental Techniques*, 2013, vol. 56, no. 5, pp. 540–545.

DOI: 10.1134/S0020441213040222

20. Prabhu K.M.M. Window functions and their applications in signal processing. CRC Press, Taylor and Francis Group, 2014, 382 p.

21. Desbiens R., Tremblay P. A new efficient approach to the design of parametric windows with arbitrary sidelobe profiles. *Signal Processing*, 2006, vol. 86, no. 11, pp. 3226–3239.

DOI: 10.1016/j.sigpro.2006.01.011

22. Dvorkovich V.P., Dvorkovich A.V. *Okonnye funkcii dlya garmonicheskogo analiza signalov* [Windows functions for harmonic analysis of signals]. Ed. 2nd. Moscow, Tekhnosfera Publ., 2016, 208 p.

Evaluation of the Magnet Breakaway Force Measurement Accuracy of the NT-800 Sensors for Early Detection of Defects of Their Manufacturing

A. Kutsepau, A. Kren, Y. Hnutschenka

*Institute of Applied Physics of the National Academy of Science of Belarus,
Akademicheskaya str., 16, Minsk 220072, Belarus*

Received 30.07.2021

Accepted for publication 02.09.2021

Abstract

Control of mechanical stresses formed with the deposition of nickel coatings plays an important role in the diagnosis of coatings' technical condition. Large internal stresses can lead to cracking or flaking of coatings which is completely unacceptable for critical parts and assembly units used, for example, in space technology for which reliability is of paramount importance. An important aspect of internal stresses monitoring is the measurement error of the instruments used. The purpose of this work was to determine the characteristics of the device sensors, which make the assessment of their manufacturing possible at the preliminary stage of the measuring equipment assembling in order to maintain the required accuracy of subsequent measurements.

In most cases the measurement error assessment is possible only after the equipment manufacture and calibration. In this paper it is proposed to evaluate the accuracy characteristics of device sensors based on the precision (repeatability and reproducibility) of the primary informative parameter recording. In the case of the NT-800 device that was developed at the Institute of Applied Physics of the National Academy of Sciences of Belarus the effect of precision characteristics deterioration on the eventual measurement error is demonstrated. Determining the precision parameters before establishing correlation dependences between the primary informative parameter and the measured characteristic is proposed in order to reject poorly manufactured sensors and reduce labor costs.

In particular, measurements of the magnitude proportional to the magnetic breakaway force were carried out using the NT-800 device with nickel specimens simulating coatings with a thickness of 200 to 700 μm and a rolling value from 0 to 40 %. It was established that in the case of well-made sensors the variation coefficient calculated from the dispersion of repeatability is in the range 0.2–0.6 %, and the variation coefficient calculated from the dispersion of reproducibility does not exceed 0.9 %. In the case of a sensor with the sensitive element parameters worsened, the variation coefficient of repeatability and reproducibility were up by one and a half times. Deterioration of the precision characteristics resulted in significant changes in the readings of the calibrated instrument. Thus the absolute measurement error for a sensor with a poorly made sensitive element turned out to be approximately 3 times higher in the range of 200–300 MPa than that for a sensor with good precision parameters.

Keywords: accuracy, repeatability, reproducibility, internal stress, magnet breakaway force.

DOI: 10.21122/2220-9506-2021-12-3-230-238

Адрес для переписки:

Крень А.П.
Ин-т прикладной физики Национальной академии наук Беларуси,
ул. Академическая, 16, г. Минск 220072, Беларусь
e-mail: 762-33-00@gmail.com

Address for correspondence:

Kren A.P.
Institute of Applied Physics of the National Academy
of Science of Belarus,
Akademicheskaya str., 16, Minsk 220072, Belarus
e-mail: 7623300@gmail.com

Для цитирования:

A. Kutsepau, A. Kren, Y. Hnutschenka.
Evaluation of the Magnet Breakaway Force Measurement Accuracy
of the NT-800 Sensors for Early Detection of Defects
of Their Manufacturing.
Приборы и методы измерений.
2021. – Т. 12, № 3. – С. 230–238.
DOI: 10.21122/2220-9506-2021-12-3-230-238

For citation:

A. Kutsepau, A. Kren, Y. Hnutschenka.
Evaluation of the Magnet Breakaway Force Measurement Accuracy
of the NT-800 Sensors for Early Detection of Defects
of Their Manufacturing.
Devices and Methods of Measurements.
2021, vol. 12, no. 3, pp. 230–238.
DOI: 10.21122/2220-9506-2021-12-3-230-238

Оценка точности измерения магнитоотрывного усилия датчиками прибора НТ-800 для раннего выявления дефектов их изготовления

А.Ю. Кутепов, А.П. Крень, Е.В. Гнутенко

Институт прикладной физики Национальной академии наук Беларуси,
ул. Академическая, 16, г. Минск 220072, Беларусь

Поступила 30.07.2021

Принята к печати 02.09.2021

Контроль механических напряжений, возникающих при нанесении никелевых покрытий, играет важную роль при диагностике их технического состояния. Большие внутренние напряжения могут приводить к растрескиванию или отслаиванию покрытий, что совершенно недопустимо для ответственных деталей и сборочных единиц, используемых, например, в космической технике, для которых надёжность имеет первостепенное значение. Важным аспектом контроля внутренних напряжений является погрешность измерений используемых приборов. Целью настоящей работы являлось определение характеристик датчиков приборов, позволяющих оценить качество их изготовления на предварительной стадии сборки измерительной техники, для соблюдения необходимой точности последующих измерений.

В большинстве случаев оценка погрешности измерений возможна только после изготовления оборудования и проведения градуировки. В настоящей работе предложено оценивать точностные характеристики датчиков приборов исходя из прецизионности (повторяемости и воспроизводимости) регистрации первичного информативного параметра. На примере прибора «НТ-800», разработанного в Институте прикладной физики Национальной академии наук Беларуси, показано влияние ухудшения характеристик прецизионности датчиков на итоговую погрешность измерений. Предложено определять параметры прецизионности до установления корреляционных зависимостей между первичным информативным параметром и измеряемой характеристикой с целью отбраковки некачественно изготовленных датчиков и снижения трудозатрат.

В частности, проведены измерения величины, пропорциональной магнитоотрывному усилию (имеющей корреляционную связь с остаточными напряжениями), прибором НТ-800 на никелевых образцах, имитирующих покрытия, толщиной от 200 до 700 мкм и величиной прокатки от 0 до 40 %. Установлено, что в случае качественно изготовленного первичного преобразователя коэффициент вариации дисперсии повторяемости находится в диапазоне 0,2–0,6 %, а коэффициент вариации, рассчитанный по значениям дисперсии воспроизводимости, не превышает 0,9 %. В случае датчика с ухудшенными параметрами чувствительного элемента коэффициенты вариации повторяемости и воспроизводимости были в 1,5 раза выше. Ухудшение характеристик прецизионности привело к значительному увеличению погрешности измерения остаточных напряжений. Так, абсолютная погрешность измерений напряжений у некачественно изготовленного датчика в диапазоне 200–300 МПа была приблизительно в 3 раза выше, чем у датчика с высокими показателями прецизионности.

Ключевые слова: точность, повторяемость, воспроизводимость, внутренние напряжения, магнитоотрывное усилие.

DOI: 10.21122/2220-9506-2021-12-3-230-238

Адрес для переписки:

Крень А.П.
Ин-т прикладной физики Национальной академии наук Беларуси,
ул. Академическая, 16, г. Минск 220072, Беларусь
e-mail: 762-33-00@gmail.com

Address for correspondence:

Kren A.P.
Institute of Applied Physics of the National Academy
of Science of Belarus,
Akademicheskaya str., 16, Minsk 220072, Belarus
e-mail: 7623300@gmail.com

Для цитирования:

A. Kutsepau, A. Kren, Y. Hnutschenka.
Evaluation of the Magnet Breakaway Force Measurement Accuracy
of the NT-800 Sensors for Early Detection of Defects
of Their Manufacturing.
Приборы и методы измерений.
2021. – Т. 12, № 3. – С. 230–238.
DOI: 10.21122/2220-9506-2021-12-3-230-238

For citation:

A. Kutsepau, A. Kren, Y. Hnutschenka.
Evaluation of the Magnet Breakaway Force Measurement Accuracy
of the NT-800 Sensors for Early Detection of Defects
of Their Manufacturing.
Devices and Methods of Measurements.
2021, vol. 12, no. 3, pp. 230–238.
DOI: 10.21122/2220-9506-2021-12-3-230-238

Introduction

Nickel coatings are most often used for thermal protection of mechanical engineering products, as well as space and aviation industry products. One of the main durability and reliability conditions of such products is compliance with the technological process of coating, the violation of which can lead to the appearance of unevenly distributed or high mechanical stresses. If the magnitude of stresses exceeds the adhesion force it may lead to delamination, and uneven distribution can lead to cracking. Thus the control of residual stresses plays an important role in diagnosing the state of both individual products and various elements of load-bearing structures in general, and the development of new reliable testing methods is a paramount task to improve the quality and reliability of products.

At present a number of devices have been developed for internal stresses monitoring using various measurement principles: X-ray, ultrasonic, magnetic, and others [1–5]. The calibration of each of them is a unique procedure. For example standard samples with certain crystal lattice parameters can be used for diffractometers. However these samples cannot be used to calibrate instruments using other physical measurement principles. This is because their readings will be influenced by the different characteristics of the samples such as the presence of plastic deformation, residual magnetization, etc.

This fully applies to the NT-800 device developed at the Institute of Applied Physics of the National Academy of Sciences of Belarus. This fully applies to the NT-800 device developed at the Institute of Applied Physics of the National Academy of Sciences of Belarus. The principle of operation of this device is based on recording the magnitude of the magneto-detachable (ponderomotive) force when a permanent magnet interacts with a ferromagnetic base. The value of the force as shown in [6] depends on two factors: the thickness of the coating and the level of internal stresses. And the sensitivity of measurements to operating voltages is much higher in weak magnetic fields. However, this leads to an increase in the requirements for the magnet breakaway force recording accuracy, the value of which also decreases and is in the range of 80–300 mN. Calibration of the NT-800 device presupposes the use of additional equipment – a testing machine and specially prepared nickel samples. The work requires tests on stepwise tension-compression of samples with simultaneous fixation of the magnitude

of the magnet breakaway force and the stresses created by the tensile machine. To remove residual stresses, the samples must first undergo vacuum annealing. Thus the calibration procedure itself is rather complicated, labor-intensive and expensive.

The fact that the metrological characteristics of sensors: the error (or uncertainty) of measurements – are evaluated only after the end of the calibration is an even greater problem. This often leads to the fact that a poorly manufactured sensor is rejected only after the entire test cycle, when the samples are already unusable and the repetition of the calibration procedure requires new costs.

The aim of the work was to determine the characteristics of the sensors which make it possible to assess the quality of their manufacture at the preliminary stage, in order to reduce labor costs and maintain the required accuracy of subsequent measurements.

Equipment and materials

The NT-800 is designed to assess the level of effective stresses build a map of stress distribution over the surface area as well as measure the thickness of nickel coatings in the range from 200 to 800 μm .

One of the main elements of the device are primary measuring transducers (sensors), which can be one of two types: 1) for use on flat surfaces and 2) for testing in hard-to-reach places of products. The formation of the measuring signal and the direct registration of the magnet breakaway force are carried out using them.

The level of internal stresses is estimated by the K_f value, which is proportional to the magnet breakaway force and is used to construct the calibration curves. Figure 1 shows the calibration dependence $K_f = f(\sigma)$ (ABC line). Here σ – applied stress, formed in nickel specimen using universal testing machine.

It is also shown in the Figure 1 that the change of K_f value is influenced by type I stress (ABC line) as well as by residual stresses, formed by plastic deformation. If the sample is unloaded at an intermediate time (at point B), then after complete removal of the load ($\sigma = 0$) points A and D don't match. This discrepancy is caused by the appearance of plastic deformations in the sample which affect K_f . Figure 1 illustrates the complex nature of the graduation, which is also discussed in [7]. Therefore a thorough experiment is required and in the absence of standards a different algorithm is required for determining the metrological characteristics and

assessing the sensor manufacturing quality at the preliminary stage.

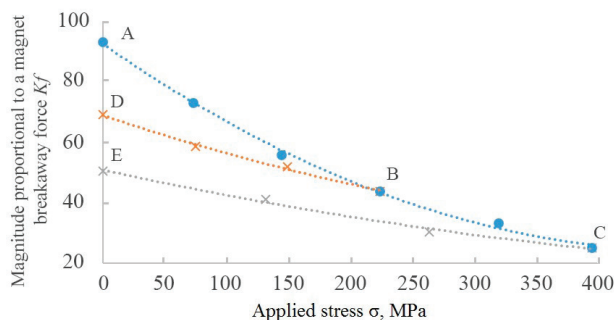


Figure 1 – K_f change depending on applied stresses for an annealed sample with a thickness of 400 μm (with removed stresses) using a sensor for flat surfaces during load (ABC) and unload (BD and CE)

To carry out work on the evaluation of the metrological characteristics of the NT-800 device sensors, that are proposed below we used special nickel samples imitating coatings with various thicknesses and internal stresses. The characteristics of these samples are presented in the Table. The cold rolling of the nickel samples ratio of which is indicated in the table, allowed to form internal stresses values of which cover the real range of stress variation (0–200 MPa) in nickel coatings using galvanic plating technology. The zero level of internal stresses in nickel samples imitating coatings was set up by heat treating: annealing the samples.

Table

Description of the nickel samples

Sample number	Thickness, μm	Rolling reduction ratio, %
1	200	0
2	215	14
3	240	0
4	300	0
5	330	34
6	400	0
7	400	10
8	400	40
9	500	0
10	500	30
11	580	13
12	700	0

Determined metrological characteristics

As mentioned in ISO/IEC Guide 98-3:2008¹ and ISO 5725-2:2002² a range of characteristics can be presented as accuracy rate indicators: uncertainty, error, trueness and precision. All the formulae used herein are taken from ISO 5725-2:2002.

In the absence of a standard for the measured quantity correctness means the closeness of the average value obtained from a large series of measurement results (or test results) to the accepted reference value. The systematic error (bias) is usually the trueness indicator. And precision refers to the degree to which independent measurement results obtained under specific specified conditions are close to each other. This characteristic depends only on random factors and is not related to the value of the measured quantity. A measure of precision is usually calculated as the standard deviation of measurements made under specified conditions. The extremes of precision measure are repeatability and reproducibility.

That is from the metrology point of view such characteristics as repeatability and reproducibility do not require reference to the true value of the measured value and can be used for preliminary assessment of the sensor manufacturing quality.

Experimental research

It is important to understand such important concepts as level of the test and cell in a precision experiment (Figure 2).

A level of the test in a precision experiment is a mean value of the measurements, from every lab for one specific tested material or specimen (in our case these are nickels specimen with different rolling reduction ratios as in Table). A set of cells related to one specimen can also be named as the level of the test.

A cell in a precision experiment is a set of measurement values for one specimen acquired in one lab. There were 72 cells in this work in total.

¹ ISO/IEC Guide 98-3:2008 Uncertainty of measurement – Part 3: Guide to the expression of uncertainty in measurement (GUM: 1995)

² ISO 5725-2:2019 Accuracy (trueness and precision) of measurement methods and results – Part 2: Basic method for the determination of repeatability and reproducibility of a standard measurement method

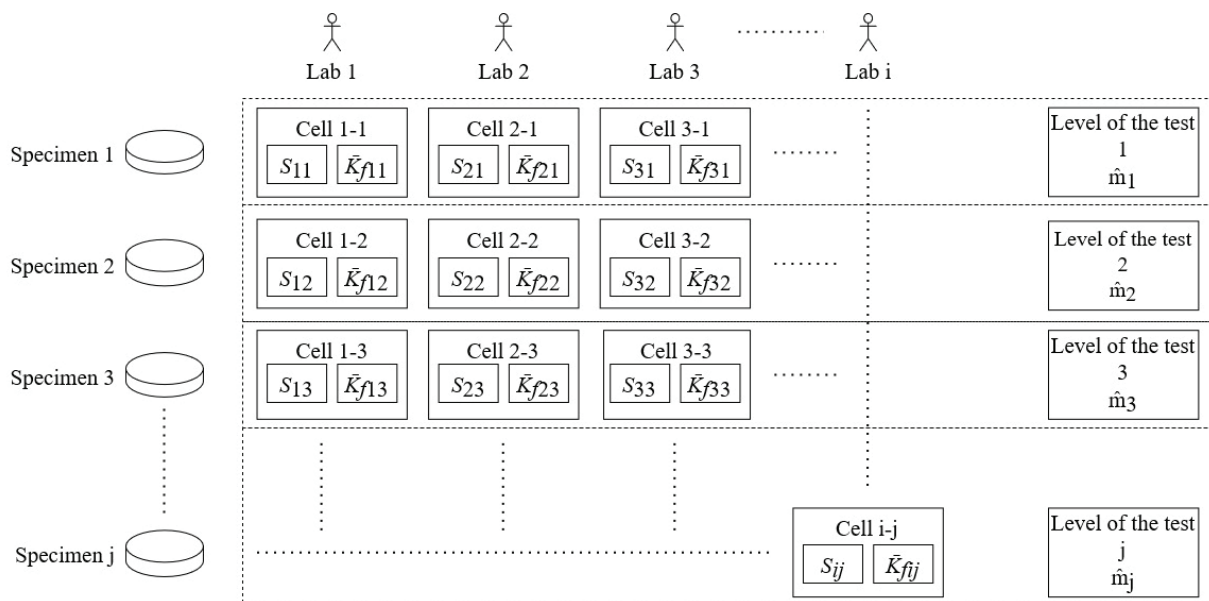


Figure 2 – General test scheme for the precision assessment

Every lab has conducted 10 measurements at every level for the repeatability evaluation. And 6 labs were involved for the reproducibility evaluation.

Arithmetic mean for the K_f values were calculated for every level for every lab as well as cell standard deviation. After that mean values for each level were calculated (averaged measurement results between labs).

Cell standard deviation was calculated using a formula:

$$s_{ij} = \sqrt{\frac{1}{n_{ij} - 1} \sum_{z=1}^{n_{ij}} (y_{ijz} - \bar{y}_{ij})^2},$$

where i – lab number; j – level; z – measurement number; y – cell; n – number of measurements in one cell.

Since the presence of laboratories or values incompatible with other laboratories or values can change the repeatability and reproducibility estimates, a decision should be made to exclude data after careful analysis. There are two approaches for such decisions: graphical compatibility analysis and statistical testing. In order to simplify the calculations and to present a visual interpretation of the results, herein we began with the first option, in which two measures are used, called Mandel's statistics h and k . It should be noted that they help to assess not only the variability of the results of the measurement

method, but also the quality of measurements of individual laboratories. The general procedure for calculating Mandel's statistics processing outliers and then estimating variances of precision is shown in Figure 3.

Statistic k is used to determine stability of measurement results and their repeatability for one laboratory by comparing the repeatability of the standard deviation of the laboratory data with the repeatability of the standard deviation of other laboratories.

Statistic h is used to determine stability of measurement results between laboratories, indicating whether the overall measurement results of an individual laboratory are not reliable.

Statistic h was calculated using formula:

$$h_{ij} = \frac{\bar{y}_{ij} - \hat{m}_j}{\sqrt{\frac{1}{(p_j - 1)} \sum_{i=1}^{p_j} (\bar{y}_{ij} - \hat{m}_j)^2}},$$

where \hat{m} – common mean value for every specimen (every level); p – number of labs.

The results of calculating statistics k and h for two types of sensors are presented in Figures 4–7.

To determine which of the calculated h_{ij} values are outliers, critical values lines were added to the diagram (Figure 4), that were determined for levels of significance of $\alpha = 1\%$ and 5% (for $p = 6$ these are 1.87 and 1.66 for 1% and 5% accordingly) [8].

If the value of statistic h exceeds the line for $h = 1.66$, corresponding to 5 % significance level, then the according cell is marked as a possible outlier, and if

the value of statistic h exceeds the line for $h = 1.87$, corresponding 1 % significance level, then the according cell is marked as an outlier.

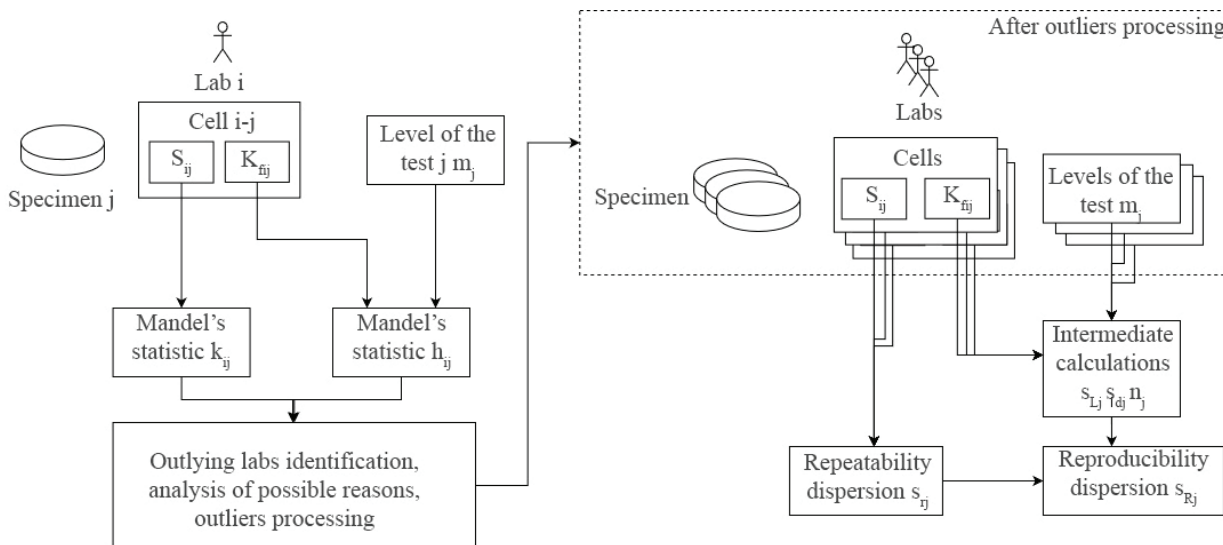


Figure 3 – General precision dispersions evaluation procedure

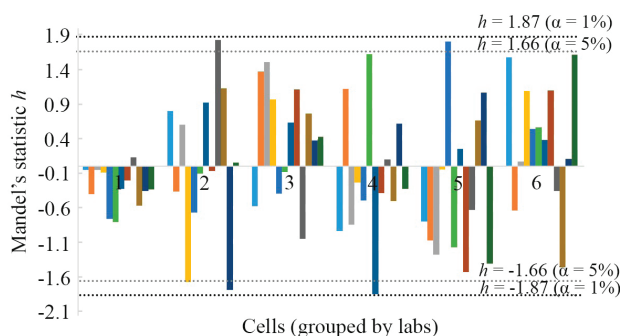


Figure 4 – Mandel's h statistics for the measurements using sensor for flat surfaces

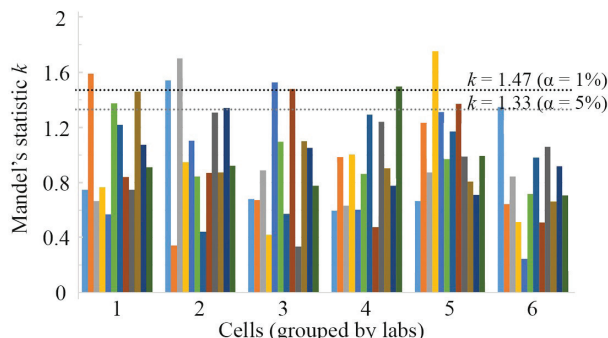


Figure 6 – Mandel's k statistics for the measurements using sensor for flat surfaces

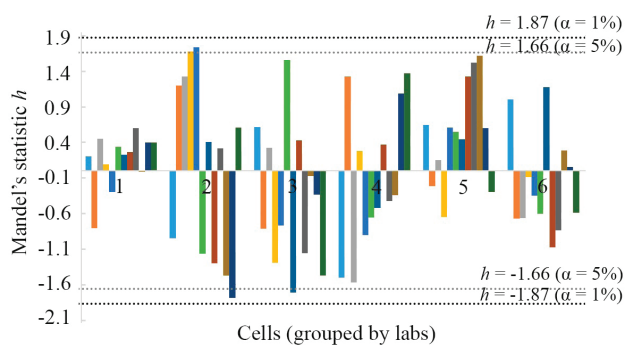


Figure 5 – Mandel's h statistics for the measurements using sensor for hard-to-reach places

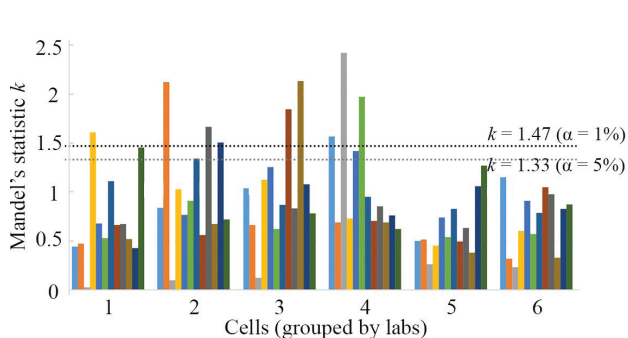


Figure 7 – Mandel's k statistics for the measurements using sensor for hard-to-reach places

Statistic k was calculated using formula:

$$k_{ij} = \frac{s_{ij} \sqrt{p_j}}{\sqrt{\sum s_{ij}^2}}$$

In turn to determine which of the calculated k_{ij} values are outliers or possible outliers, a procedure was carried out similar to outlier analysis for statistic h . For $p = 6$ and the number of measurements in the cell equal to 10, critical values equal to 1.47 and 1.3 for 1 % and 5 % accordingly.

The outliers and possible outliers were determined among cells using diagrams presented on Figures 4–7 these are all the values, exceeding significance levels $\alpha = 1\%$ и 5% accordingly. For example, for lab 1, test results on level 2 were marked as outliers, levels 6 and 10 as possible outliers (Figure 7). The calculation of Mandel's statistics and graphical analysis is necessary to determine the reason of a worse repeatability in individual labs and to eliminate those reasons, and for subsequent statistical outliers testing. Since the outliers and possible outliers are singular and do not have a common underlying cause, we consider outliers as true outliers and cells, that were marked as outliers were deleted from calculations.

After statistical outliers testing, we've calculated the repeatability and reproducibility characteristics. Repeatability variance was determined for each level using formula:

$$s_{rj}^2 = \frac{1}{\sum_{i=1}^p (n_{ij} - 1)} \sum_{i=1}^p s_{ij}^2 (n_{ij} - 1).$$

Lab variance was determined for each level using formula:

$$s_{Lj}^2 = \frac{s_{dj}^2 - s_{rj}^2}{\bar{n}_j},$$

where

$$s_{dj}^2 = \frac{1}{p-1} \sum_{i=1}^p n_{ij} (\bar{y}_{ij} - \hat{m}_j)^2;$$

$$\bar{n}_j = \frac{1}{p-1} \left[\sum_{i=1}^p n_{ij} - \frac{\sum_{i=1}^p n_{ij}^2}{\sum_{i=1}^p n_{ij}} \right].$$

Reproducibility variances were calculated after the lab variances was determined using formula:

$$s_{Rj}^2 = s_{rj}^2 + s_{Lj}^2.$$

For a better presentation, reproducibility and repeatability variances were calculated into variance coefficients (VC) and displayed as a function of K_f (Figures 8 and 9).

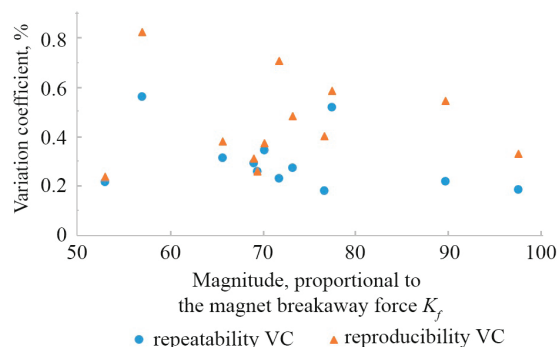


Figure 8 – Repeatability and reproducibility variation coefficient using sensors for flat surfaces

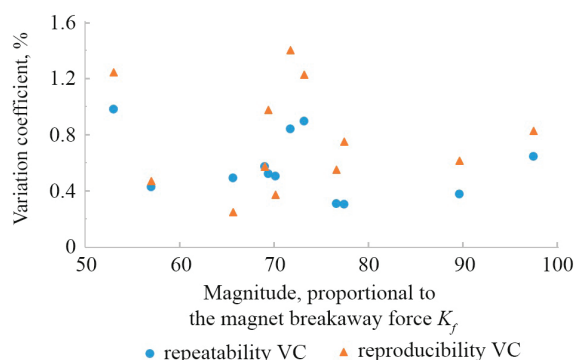


Figure 9 – Repeatability and reproducibility variation coefficient using sensors for hard-to-reach places

Figure 8 shows, that repeatability VC is concentrated between 0.2–0.4 %, and reproducibility VC is concentrated between 0.2–0.6 %. Both characteristics are not dependent on the magnet breakaway force, and the maximum value of reproducibility VC does not exceed 0.9 %, while repeatability VC does not exceed 0.6 %. Figure 9 shows a similar picture, but all VC values are ≈ 1.7 higher, which means that the sensor for hard-to-reach places had worse accuracy characteristics.

Indeed, after the close inspection of the sensor for hard-to-reach places it was determined that the surface of the magnet had accumulated metallic dust the presence of which worsened the sensor accuracy. Several sensors were graduated with the goal of evaluating their measurement accuracy then stress measurement of these sensors was compared

with the stresses induced by testing machine. Wherein the surface of the sensitive element of a sensor with worse precision characteristic was not cleared.

As it can be seen in the Figure 10 worsening the precision characteristics leads to significant deviation of sensor measurements when directly measuring stress in nickel specimen.

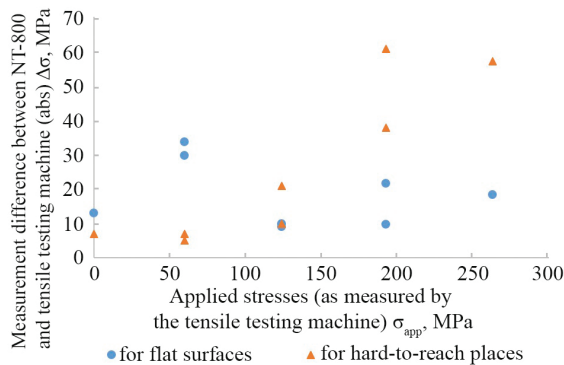


Figure 10 – Scatter plot of the difference between the readings of the NT-800 and the tensile machine against the applied stresses according to the readings of the tensile machine

From the data shown in Figure 10, it can be seen that degradation in precision performance leads to significant changes in device readings. Thus, the absolute measurement error of the sensor for hard-to-reach places was ≈ 3 times higher than that of the sensor for flat surfaces in the range of 200–300 MPa. Taking into account that the dependence of the magnet breakaway force on stresses is inverse (Figure 1) then the measurement errors of sensors at high voltages should decrease. In the case of a sensor for hard-to-reach places, this pattern is not present. This confirms the importance of defining the characteristics of precision: repeatability and reproducibility and the possibility of their use for rejection of sensors in the preliminary stage. Extensive research carried out later yielded similar results. Sensors which had an unstable operation of spring elements, friction in the bearing units of motors, also had an increased repeatability and reproducibility VC (by more than 1.5 %) which ultimately affected the absolute measurement error. These studies also helped to establish that with the repeatability and reproducibility VC not exceeding 1 %, the absolute error in the stress range of 1–300 MPa does not exceed 35 MPa, which meets the requirements of most consumers.

Conclusion

The repeatability and reproducibility variation coefficients allow you to get an idea of the accuracy characteristics of the device, and compare different devices and sensors with each other at the preliminary stage of their manufacture. This makes it possible to identify sensors with insufficient quality in time and avoid additional labor costs.

The mean values and variances of the K_f value were determined for all cells (combinations of laboratory and test level). The repeatability variances s_r^2 and reproducibility variances s_R^2 were calculated, on their basis the corresponding variation coefficients were calculated. In case of the sensor for flat surfaces, repeatability variation coefficients were concentrated in the 0.2–0.4 % range and did not exceed 0.6 %, and reproducibility variation coefficients were concentrated in the 0.2–0.6 % range and did not exceed 0.9 %. Repeatability and reproducibility variation coefficients of the sensor with worsened accuracy characteristics were 1.7 higher due to impurity of the sensitive element.

It was determined that the values of variances s_r^2 and s_R^2 practically do not depend on the thickness of the tested specimen or on its internal stresses and can be used as an objective characteristic to make decision on sensors rejection.

References

1. Practical residual stress measurement methods / edited by Gary S. Schajer: John Wiley & Sons Ltd, 2013, 310 p.
2. Rasilo P., Aydin U., Martin F., Belahcen A., Kouhia R., Daniel L. Equivalent strain and stress models for the effect of mechanical loading on the permeability of ferromagnetic materials. *IEEE Transactions on Magnetics*, 2019, vol. 55, iss. 6, pp. 1–4. DOI: 10.1109/TMAG.2018.2890407
3. Weisensel N., Liang C. Magnetotagging, A New method for active and passive nondestructive evaluation of stresses and defects in composite structures. *Materials Technology*, 2016, vol. 10, iss. 7–8, pp. 142–144. DOI: 10.1080/10667857.1995.11752613
4. Ivanova Y., Partalin T. Comparative measurements of the stress state in a rolled carbon steel using magnetic Barkhausen noise and ultrasonic method. *Russian Journal of Nondestructive Testing*, 2012, no. 48, pp. 137–146. DOI: 10.1134/S1061830912020040
5. Filinov V.V., Kuznetsov A.N., Arakelov P.G. Monitoring stressed state of pipelines by magnetic

parameters of metal. *Russian Journal of Nondestructive Testing*, 2017, no. 53, pp. 51–61.

DOI: 10.1134/S1061830917010065

6. Rudnitskiy V.A., Hnutsenka E.V., Kren A.P. *Opredelenie tolshchiny dvuslojnyh nikel'-hromovyh pokrytij magnitnym metodom* [Determination of the thickness of double-layered nickel-chrome platings using magnetic method]. *Metrologiya i priborostroyeniye* [Metrology and Instrumentation], 2015, no. 4, pp. 24–29 (in Russian).

7. Gorkunov E.S., Povolotskaya A.M., Zadvor-kin S.M., Putilova E.A. Comparative analysis of the magnetic characteristics of plastically deformed metal in different zones of a welded pipe under elastic deformation. *Russian Journal of Nondestructive Testing*, 2017, vol. 53, pp. 636–643. **DOI:** 10.1134/S1061830917090066

8. Wilrich P.-T. Critical values of Mandel's h and k , the Grubbs and the Cochran test statistic. *Advances in Statistical Analysis*, 2013, no. 97(1), pp. 1–10.

DOI: 10.1007/s10182-011-0185-y

Calculation of the Effective Energy Release Center's Position of Inorganic Scintillation Detectors for Calibration at Small "Source–Detector" Distances

R. Lukashевич, G. Fokov

SPE "ATOMTEX",
Gikalo str., 5, Minsk 220005, Belarus

Received 15.07.2021

Accepted for publication 17.08.2021

Abstract

Inorganic scintillation detectors are widely used to measure of dose rate in the environment due to their high sensitivity to photon radiation. A distinctive feature when using such detectors is the need to take into account of the position of the effective energy release center. This peculiarity is actual when using measuring instruments with inorganic scintillation detectors as working standards during calibration at short "source–detector" distances in conditions of low-background shield or using a facility with protection from external gamma radiation background in the dose rate range from 0.03 to 0.3 $\mu\text{Sv/h}$ ($\mu\text{Gy/h}$). The purpose of this work was to calculate the position of the effective energy release center of NaI(Tl) scintillation detectors and to take it into account when working at short "source–detector" distances.

An original method of determining the position of the effective energy release center when irradiating the side and end surfaces of inorganic scintillation detector with parallel gamma radiation flux and point gamma radiation sources at small "source–detector" distances using Monte Carlo methods is proposed. The results of calculations of the position of the effective energy release center of NaI(Tl) based detectors of "popular" sizes for the cases of parallel gamma radiation flux and point sources of gamma radiation at small "source–detector" distances are presented. The functional dependences of the position of the effective energy release center of NaI(Tl) based detectors on the distance to the point gamma radiation sources and the energy of gamma radiation sources are presented.

As a result of the study it was found that for scintillation NaI(Tl) detectors of medium size (for example, $\text{Ø}25 \times 40$ mm or $\text{Ø}40 \times 40$ mm) the point gamma radiation source located at a distance of 1 m or more, creates a radiation field which does not differ in characteristics from the radiation field created by a parallel flux of gamma radiation. It is shown that approaching the point gamma radiation source to the surface of scintillation detector leads to displacement of the position of the effective energy release center to the surface of the detector.

Keywords: effective energy release center, inorganic scintillation detector, near background radiation, Monte Carlo method.

DOI: 10.21122/2220-9506-2021-12-3-239-248

Адрес для переписки:

Лукашевич Р.В.
УП «АТОМТЕХ»,
ул. Гикало, 5, г. Минск 220005, Беларусь
e-mail: rimlianin@gmail.com

Address for correspondence:

Lukashевич R.
SPE "ATOMTEX",
Gikalo str., 5, Minsk 220005, Belarus
e-mail: rimlianin@gmail.com

Для цитирования:

R. Lukashевич, G. Fokov.
Calculation of the Effective Energy Release Center's Position of Inorganic Scintillation Detectors for Calibration at Small "Source–Detector" Distances.
Приборы и методы измерений.
2021. – Т. 12, № 3. – С. 239–248.
DOI: 10.21122/2220-9506-2021-12-3-239-248

For citation:

R. Lukashевич, G. Fokov.
Calculation of the Effective Energy Release Center's Position of Inorganic Scintillation Detectors for Calibration at Small "Source–Detector" Distances.
Devices and Methods of Measurements.
2021, vol. 12, no. 3, pp. 239–248.
DOI: 10.21122/2220-9506-2021-12-3-239-248

Расчёт положения эффективного центра энергосвечения сцинтилляционных детекторов для задач калибровки при малых расстояниях «источник–детектор»

Р.В. Лукашевич, Г.А. Фоков

УП «АТОМТЕХ»,
ул. Гикало, 5, г. Минск 220005, Беларусь

Поступила 15.07.2021

Принята к печати 17.08.2021

Неорганические сцинтилляционные детекторы широко используются для измерения мощности дозы в окружающей среде благодаря их высокой чувствительности к фотонному излучению. Отличительной особенностью при использовании таких детекторов является необходимость учёта положения эффективного центра энергосвечения. Эта особенность актуальна при использовании средств измерений с неорганическими сцинтилляционными детекторами в качестве рабочих эталонов при калибровке на малых расстояниях «источник–детектор» в условиях низкофоновой камеры или установки с защитой от внешнего фона гамма-излучения в диапазоне мощностей доз от 0,03 до 0,3 мкЗв/ч (мкГр/ч). Целью данной работы являлся расчёт положения эффективного центра энергосвечения сцинтилляционных NaI(Tl) детекторов и его учёт при работе на малых расстояниях «источник–детектор».

Предложен оригинальный метод определения положения эффективного центра энергосвечения при облучении боковых и торцевых поверхностей неорганического сцинтилляционного детектора параллельным потоком гамма-излучения и точечными источниками гамма-излучения на малых расстояниях «источник–детектор» с использованием методов Монте-Карло. Представлены результаты расчёта положения эффективного центра энергосвечения детекторов на основе NaI(Tl) «популярных» размеров для случаев параллельного потока гамма-излучения и точечных источников гамма-излучения на малых расстояниях «источник–детектор». Приведены функциональные зависимости положения эффективного центра энергосвечения детекторов на основе NaI(Tl) кристаллов от расстояния до точечных источников гамма-излучения и энергии источников гамма-излучения.

В результате исследования установлено, что для сцинтилляционных NaI(Tl) детекторов небольших размеров (например, $\varnothing 25 \times 40$ мм или $\varnothing 40 \times 40$ мм) точечный источник гамма-излучения, находящийся на расстоянии 1 м и более, создаёт поле излучения, не отличающееся по характеристикам от поля излучения, которое создаёт параллельный поток гамма-излучения. Показано, что приближение точечного источника гамма-излучения к поверхности сцинтилляционного детектора приводит к смещению положения эффективного центра энергосвечения к поверхности детектора.

Ключевые слова: эффективный центр энергосвечения, неорганический сцинтилляционный детектор, околорезонансное гамма-излучение, метод Монте-Карло.

DOI: 10.21122/2220-9506-2021-12-3-239-248

Адрес для переписки:
Лукашевич Р.В.
УП «АТОМТЕХ»,
ул. Гикало, 5, г. Минск 220005, Беларусь
e-mail: rimlianin@gmail.com

Address for correspondence:
Lukashевич R.
SPE "ATOMTEH",
Gikalo str., 5, Minsk 220005, Belarus
e-mail: rimlianin@gmail.com

Для цитирования:
R. Lukashевич, G. Fokov.
Calculation of the Effective Energy Release Center's Position of Inorganic Scintillation Detectors for Calibration at Small "Source–Detector" Distances.
Приборы и методы измерений.
2021. – Т. 12, № 3. – С. 239–248.
DOI: 10.21122/2220-9506-2021-12-3-239-248

For citation:
R. Lukashевич, G. Fokov.
Calculation of the Effective Energy Release Center's Position of Inorganic Scintillation Detectors for Calibration at Small "Source–Detector" Distances.
Devices and Methods of Measurements.
2021, vol. 12, no. 3, pp. 239–248.
DOI: 10.21122/2220-9506-2021-12-3-239-248

Introduction

An important task in radiation monitoring is the correct measurement of dose rate at the level of natural radiation background. For this purpose it is necessary to use measuring instruments with high sensitivity, low level of own background and high temporal stability. In this case, an important problem to be solved during calibration of dosimetric measuring instruments is to provide the lower limit of measuring range at the level of the background radiation of the environment. According to the recommendations of the International Electrotechnical Commission (IEC) [1–3] and technical requirements for ARMS of nuclear power plants¹, the lower limit of the measurement range of dose rate of radiation protection instruments when controlling the radiation situation in the environment should be at 0.03 $\mu\text{Sv/h}$ ($\mu\text{Gy/h}$). The use of highly sensitive dosimetry devices based on scintillation spectrometric detection units becomes possible to measure dose rates below 0.1 $\mu\text{Sv/h}$ ($\mu\text{Gy/h}$), and the ability of such devices to measure dose rates below 0.1 $\mu\text{Sv/h}$ ($\mu\text{Gy/h}$) should be confirmed by special studies². In addition, in the calibration scheme³ requirements to working standards having protection from external gamma radiation background for metrological support of photon radiation fields of near background levels for dose rate (0.03–0.3 $\mu\text{Gy/h}$ ($\mu\text{Sv/h}$)) are given. This dose rate range is easily achievable for inorganic scintillation detector units with NaI(Tl) crystals, even of medium size.

A significant contribution to the dose rate for measurements below 0.3 $\mu\text{Sv/h}$ ($\mu\text{Gy/h}$) is the natural background radiation. In this case the calibration or verification of measuring instruments

under normal laboratory conditions is practically impossible, because the radiation background in the laboratory can change during the measurements due to many factors, which can significantly affect the measurement results of gamma radiation fields of the near background level on the dose rate.

To create the reference near background photon radiation fields it is necessary metrologically to provide the dose rate values at the level of 0.03–0.3 $\mu\text{Sv/h}$ ($\mu\text{Gy/h}$), i. e. to creation of reference near-background photon radiation fields with minimal influence of natural radiation background, e. g. in a low-background shield or on a facility with protection from external gamma radiation background by a reference measuring instruments. For this purpose it is necessary to use highly sensitive measuring instruments and ensure their calibration in similar reference photon radiation fields with dose rate of 0.03–0.3 $\mu\text{Sv/h}$ ($\mu\text{Gy/h}$).

Dose rate calibrations and measurements in near-background photon radiation fields in low-background laboratories are limited by the location of such laboratories (e. g. UDO II in Germany or IFIN-HH in Romania) [4–5], which implies certain difficulties for periodic calibrations and verifications of measuring instruments. To solve this problem it is optimal to use low-background shield and facility which are smaller in physical size than installations in low-background laboratories. The limitation of the size of low-background shield and facility is related to the compromise between the cost of protective materials for such a unit and sufficient source-detector distance to provide the necessary characteristics of the radiation field. The use of a low-background shield or facility with a small range of distances for calibration of measuring instruments also requires ensuring the accuracy of positioning of the measuring instrument relative to the radiation source. This is especially relevant when using measuring instruments based on inorganic scintillation detectors as reference instruments for transmitting dose rate units. Since we apply the method of substitution when calibrating measuring instruments, it is necessary to ensure with good accuracy the same distance from the radiation source to the center of the detectors of measuring instruments.

The purpose of this work was to calculate the position of centers of inorganic scintillation detectors from the energy of radiation and to take it into account when working at short “source-

¹STO 1.1.1.01.001.0875–2017. Automated system for monitoring the radiation environment of a nuclear power plant. Technical requirements. – Introduced 10.12.2018. – Rosenergoatom Concern OJSC, 2018.

²MU 2.6.5.008–2016. Nuclear power and industry. Control of radiation situation. General requirements. Methodical instructions. – Introduced 22.04.16; with amendments 05.05.17. – M., 2016. – P. 82.

³State calibration scheme for measuring instruments of kerma in the air, kerma power in the air, exposure dose, exposure dose rate, ambient, directed and individual dose equivalents, powers of ambient, directed and individual dose equivalents and energy flow of X-ray and gamma radiation. – Introduced on 31.12.20 by the Federal Agency for Technical Regulation and Metrology. – Rosstandart, Moscow, 2020. – P. 13.

detector” distances within the project on creation of a facility with protection from external gamma radiation background for calibration and verification of dosimetric measuring instruments.

Calibration method

Calibration of an instrument for environmental radiation monitoring is accomplished by placing its detectors in a radiation field with a known dose rate and comparing the instrument readings to this dose rate. The dose rate can be determined in two ways: either by using an instrument whose calibration is traceable to national standards or by using a radioactive source whose activity is known and using the kerma constant to calculate the kerma rate in the air in the point of measurement, taking into account attenuation in air and the influence of scattered radiation. The second approach causes some difficulties because of the necessity to take into account the attenuation of radiation in the air and the influence of scattered radiation, therefore at the calculated distances dose rates are usually measured with a reference measuring instrument, which are taken as values of dose rate in the point of measurement. After that the calibration or dose characteristic of dosimetric measuring instruments at these points is carried out by the method of substitution.

The advantage of the first approach is that both measurements are made under the same conditions, so the method of substitution eliminates systematic measurement errors caused by errors of the reference measuring instrument serving for comparison of the measured quantity with the investigated or calibrated measuring instrument. In addition, the response of the instrument being calibrated and the reference instrument to scattered radiation can be corrected. To do this, dose rate measurements with and without an individually shaped lead shield for the reference and calibrated instruments should be performed. Using this approach, the distance from the source to the detector must be large enough to provide an almost parallel and homogeneous gamma radiation flux over the entire volume of the detector. This requirement is readily achievable on dosimetric facilities in laboratories.

But the main disadvantage of making measurements in a low-background shield or on a facility with protection from external gamma radiation background lies in the limited space of the shield or facility itself, which imposes restrictions

on the application of this approach. In addition, the short distances between the radiation source and the measuring instrument in a low-background shield or on a facility with protection from external gamma radiation background require accurate positioning of the measuring instrument relative to the radiation source, taking into account the effective or geometric center of the detector.

If we consider measuring instruments based on Geiger-Mueller counters, semiconductor detectors or organic scintillators, it is sufficient to use the geometric center of the detector for positioning. In inorganic scintillation detectors, the position of the energy release center depends on the energy of the radiation, so it is necessary to speak of the effective energy release center as the averaged center of energy loss of charged secondary particles as they pass through the scintillator substance. Therefore, the effective center corresponds to a conditional point of the detector's sensitive volume, in relation to which the absolute efficiency of registration when moving the radiation source changes according to the law of inverse squares [6].

To determine the metrological characteristics of the gamma radiation field of near-background levels at the facility having protection from external gamma radiation background, using point gamma radiation sources and reference measuring instruments based on inorganic scintillation detectors, it is necessary to evaluate the influence of the geometry of irradiation of the measuring instrument on the position of the effective energy release center in the detector.

The problem of the effective energy release center

Failure to take into account the distance from the surface of the detection unit to the position of the effective center may affect the accuracy of determining the distance between the radiation source and the detector and, consequently, the determination of the dose rate, especially when measurements are made at short distances from the radiation source, as in the case we are considering in the conditions of a low-background shield or on a facility with protection from external gamma radiation background.

In case of point sources the dose rate changes proportionally to the inverse square of the distance R . Displacement of the dosimeter reference point in the beam by ΔR in the beam direction leads to a relative error in the calibration coefficient of $2\Delta R/R$ at distance R [7].

In [8–9] you can find several formulas to calculate the effective energy release center of scintillation detectors:

$$d(E) = \frac{1}{\mu(E)} \ln \frac{1 + e^{-\mu(E)l}}{2}; \quad [8] \quad (1)$$

$$d(E) = \frac{1}{\mu(E)} \ln \frac{\mu(E)l}{1 - e^{-\mu(E)l}}, \quad [9] \quad (2)$$

where $\mu(E)$ is the linear attenuation coefficient of gamma radiation with energy E for the NaI(Tl) detector, cm^{-1} ; l is the thickness of the NaI(Tl) detector, cm.

It is important to note that there are no reservations in the publications [8, 9] about the location of scintillation detector (radiation falls on the face or side surface of the detector), so, based on these formulas, we can assume that the position of effective detector center depends only on detector length and gamma radiation energy. Table 1 presents the results of calculating the position of the effective center of the detector based on NaI(Tl) using the formulas from [8, 9] and the Monte Carlo method. The SNEGMONT software package, which was developed and successfully used at ATOMTEX enterprise, was used for the calculations [10].

Table 1

Comparison of the results of calculation of the effective center of the NaI(Tl) detector Ø40×40 mm when the radiation falls on the end surface using formulas from various sources and the Monte Carlo method

Gamma radiation energy, keV	Results of calculations of the effective center of the NaI(Tl) detector Ø40×40 mm, mm		
	Monte Carlo method	according to the formula from [8]	according to the formula from [9]
20	0.09	0.07	0.09
59.5	0.32	1.92	0.30
100	1.19	5.40	1.20
165.9	4.60	11.5	4.21
391.7	14.1	17.3	12.6
661.6	16.2	18.2	14.8
1250	17.3	18.8	16.4
2614	17.9	19.1	17.3
5000	17.9	19.2	17.5
10000	18.7	19.2	19.1

As can be seen from Table 1, calculations of the position of the effective center of the NaI(Tl) Ø40×40 mm detector using the Monte Carlo method and the formula from [9] give comparable results. The calculated values of the detector effective center position using the formula from [8] in the 60 keV–3 MeV range are larger than those obtained by the Monte Carlo method and the formula from [9], while in the 60–200 keV range they are significantly overestimated (up to 600 %) relative to the values obtained by the Monte Carlo method and the formula from [9].

However, there is no information about the position of the effective center when the source is located at a short distance from the detector, because in this case, the smaller the distance between the radiation source and the detector, the more heterogeneous the dose profile.

Since point sources are used for calibration, and the distance between the radiation source and the detector in a low-background shield or on a facility with protection from external gamma radiation background is small, the dose profile is determined according to the law of squares of distance. In such a case, the location of the effective center of the detector will be significantly affected by the distance between the radiation source and the detector itself – the smaller the distance, the steeper the dose profile in the detector.

Thus, errors in determining the distance from the center of a point gamma radiation source to the effective energy release center of the detector can lead to incorrect determination of the dose rate, which in turn will lead to errors in the calibration of dosimetric measuring instruments by the method of substitution.

Results and discussion

To account for the position of the effective center of the detector depending on the detector irradiation geometry and on the distance to the radiation source, calculations were performed for NaI(Tl) based scintillation detectors of “popular” sizes using the Monte Carlo method. The distances between the radiation source and detector were chosen based on the operating distances that could be achieved in a low-background shield or on a facility with protection from external gamma radiation background. In addition, we compared the position of the effective energy release center for scintillation detectors based on NaI(Tl) “popular”

sizes for the case with a point source and a parallel flux of gamma radiation.

To solve this problem, an original method was applied, which we will consider using the examples when the uniform gamma radiation flux is normal to the side surface of the detector and when a point source of radiation is applied to the end face of a cylindrical detector.

When calculating the position of the effective energy release center for a uniform gamma ray flux, we imposed on the cylinder a virtual grid consisting of tightly spaced cells. The virtual grid itself as a whole is a parallelepiped with a height equal to the height H of the cylindrical detector. The cross

section of this parallelepiped is a square with a side equal to the diameter of the detector D . This parallelepiped is sliced along the height into narrow extended cells. The length of each cell is equal to the height of the cylinder H . The cross section is square with side D/N , where N is the number of cells.

In the process of modeling the impact of gamma ray flux on the detector, we accumulate the energy release in each cell separately. As a result we obtain for each cell some value averaged over its volume. I. e. at the output we have a two-dimensional table of energy release. And then we find the position of the effective center for this detector by a certain technique (Figures 1 and 2).

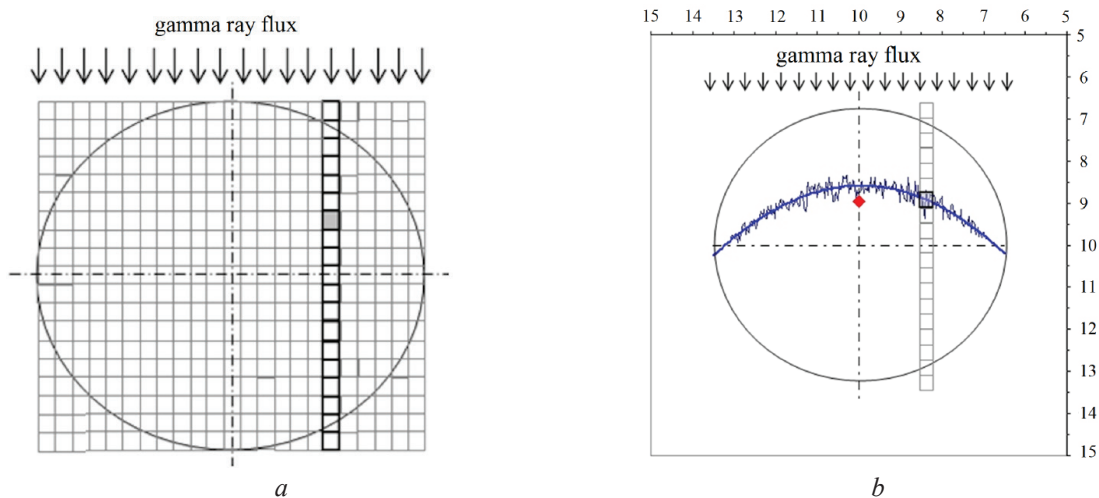


Figure 1 – Visual representation of the effective center calculation: the process of overlaying the grid on the detector side projection (a) and energy accumulation in each grid cell (b)

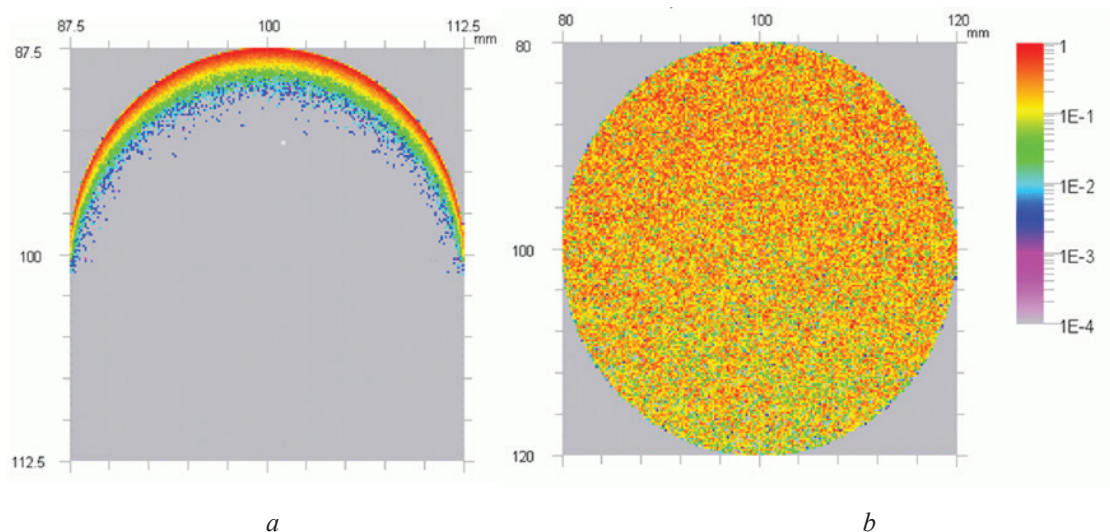


Figure 2 – Energy distribution of gamma radiation flux with energy 59.5 keV (a) in NaI(Tl) scintillation detector $\text{Ø}25 \times 40$ mm and 662 keV (b) in NaI(Tl) scintillation detector $\text{Ø}40 \times 40$ mm. In the palette on the right, one represents the maximum, and the other numbers represent its fractions

In the case of a point source, it was above the detector on its symmetry axis, so the problem was solved in the axial symmetry approximation.

The elementary cell of the virtual grid of accumulation of allocated energy was a ring with a rectangular cross section. The figure is simplified, because in reality the partitions are not 8 in radius and not 32 in height, but an order of magnitude more. For example, for NaI(Tl) $\text{Ø}40 \times 40$ mm, 662 keV point source on the surface of the entrance window (i. e., 50 mm from the crystal), 50 radial partitions and 100 in height were made. Thus, 5.000 ring-

shaped elementary cells were set (although the cells “strung” on the symmetry axis are not rings, but disks, conditionally they can be called rings with zero internal radius).

At the end of the simulation, the energy accumulated in each ring was divided by its volume (or mass, depending on the desired units). The result was a two-dimensional distribution of the specific energy allocated in the detector crystal. The grid of partitioning the cylindrical crystal into energy release cells in the simulation had the form shown in Figure 3.

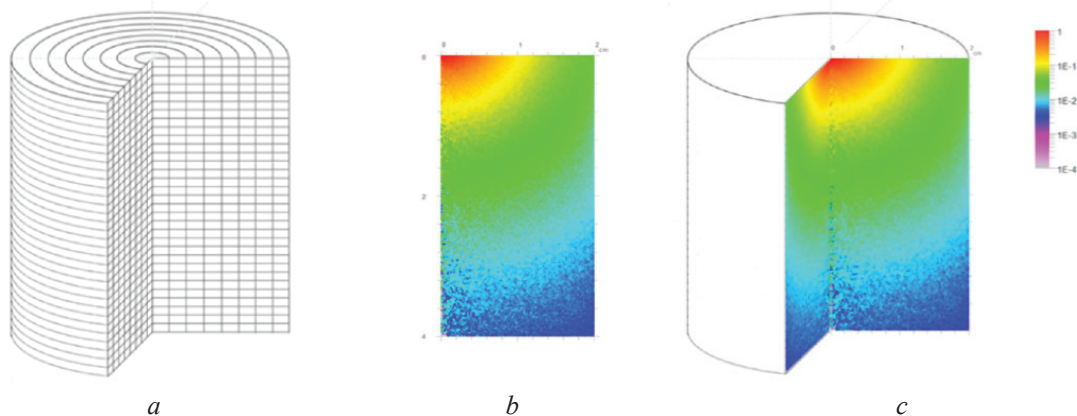


Figure 3 – Simplified example of dividing the crystal volume into 8 elementary rings by radius and 32 layers by height (a); example of a two-dimensional energy release pattern (b); example of a three-dimensional energy release pattern (c). In the palette on the right, one represents the maximum, and the other numbers represent its fractions

Next, the extracted energy was summed over the radial cells for each layer. As a result, a one-dimensional depth distribution of the extracted energy was obtained. The effective center was found provided that the areas under the curve to the right and left of it were equal.

Tables 2, 3 present the results of Monte Carlo calculations of the position of the effective energy release center of NaI(Tl) $\text{Ø}40 \times 40$ mm and NaI(Tl) $\text{Ø}25 \times 40$ mm detectors for a point gamma radiation source at different distances from the detector and for a parallel flux of gamma radiation in the case when the radiation falls on the end and on the side surface of the detector, respectively.

As can be seen from tables 2, 3: as the distance between the detector and the point gamma radiation source increases, the effective center shifts deep into the detector and for a distance of 1 meter practically coincides with the case when the radiation field is created by a parallel flux of gamma radiation. This suggests that at distances of more than 1 meter between the source and the detector, the dose profile in the detector is similar to the dose profile when

the radiation falls on the detector as a parallel flux. So, for distances less than 1 m between the source and the detector, the displacement of the position of the effective energy release center must be taken into account.

Consider the NaI(Tl) detector $\text{Ø}40 \times 40$ mm. For the 12.5 cm “point source–detector” distance, the displacement of the position of the effective energy release center of the detector in the example of the source with the radionuclide ^{137}Cs is 2.2 mm for the end-exposed geometry and 2.3 mm for the side-exposed geometry relative to the parallel gamma radiation flux. This offset will lead to relative errors in dose rate determination of 3.5 % and 3.7 % for the detector end and side irradiation geometries, respectively. When using a source with radionuclide ^{241}Am , the displacement of the position of the effective energy release center for the end geometry at any distance according to our calculations is not observed, and in the lateral irradiation geometry the displacement will be 1.04 mm at 12.5 cm “point source–detector” relative to the parallel flux of gamma radiation.

Table 2

Results of calculating the position of the effective energy release of the NaI(Tl) Ø40×40 mm detector for a point gamma radiation source at different distances from the end and side surfaces of the detector, for a parallel flux of gamma radiation

Distance from source to end surface, mm	Distance from the end surface of NaI(Tl) scintillator to the effective center, mm					
	59.5 keV	100 keV	200 keV	392 keV	662 keV	2.614 keV
50	0.29	1.10	5.13	10.4	12.1	13.0
125	0.32	1.15	5.90	12.2	14.1	15.5
250	0.32	1.19	6.30	13.0	15.1	16.6
500	0.32	1.21	6.51	13.5	15.7	17.3
1000	0.32	1.22	6.61	13.8	15.9	17.6
Parallel flux	0.32	1.23	6.65	14.1	16.3	18.2
Distance from the source to the side surface, mm	Distance from side surface of NaI(Tl) scintillator to the effective center, mm					
	59.5 keV	100 keV	200 keV	392 keV	662 keV	2.614 keV
50	1.95	2.80	6.75	11.12	12.4	13.1
125	3.25	4.16	8.56	13.7	15.2	16.2
250	3.76	4.72	9.29	14.7	16.2	17.2
500	4.02	4.99	9.64	15.1	16.7	17.8
1000	4.17	5.14	9.83	15.4	17.0	18.1
Parallel flux	4.29	5.19	9.97	15.7	17.5	19.9

Table 3

Results of calculating the position of the effective energy release of the NaI(Tl) detector Ø25×40 mm for a point gamma radiation source at different distances from the end and side surfaces of the detector, for a parallel flux of gamma radiation

Distance from source to end surface, mm	Distance from the end surface of NaI(Tl) scintillator to the effective center, mm					
	59.5 keV	100 keV	200 keV	392 keV	662 keV	2.614 keV
50	0.28	1.10	5.12	10.1	11.6	12.8
125	0.29	1.19	6.00	11.9	13.7	15.3
250	0.30	1.23	6.34	12.8	14.7	16.4
500	0.30	1.25	6.52	13.2	15.3	17.1
1000	0.30	1.26	6.63	13.5	15.6	17.5
Parallel flux	0.30	1.27	6.67	13.6	15.8	18.1
Distance from the source to the side surface, mm	Distance from side surface of NaI(Tl) scintillator to the effective center, mm					
	59.5 keV	100 keV	200 keV	392 keV	662 keV	2.614 keV
50	1.77	2.61	6.08	8.78	9.30	9.57
125	2.34	3.23	6.99	9.86	10.5	10.8
250	2.55	3.44	7.34	10.3	10.9	11.3
500	2.66	3.56	7.52	10.5	11.1	11.5
1000	2.71	3.62	7.60	10.6	11.2	11.6
Parallel flux	2.80	3.70	7.80	10.7	11.4	12.0

In this case, the relative error in determining the dose rate for the lateral geometry will be 1.7 %. Obviously, when the distance “point source–detector” increases, the relative error in measuring the dose rate will decrease. In addition, it should be noted that using the geometric center of the detector instead of the effective energy release center of the detector, will lead to an even larger relative error in determining the dose rate.

When making measurements or calibrations under conditions of small distances between the point radiation source and scintillation inorganic detector of NaI(Tl) type for working distance “source–detector” from 10 to 50 cm it is necessary to calculate the position of effective energy release center of during calibration of measuring instruments on dose rate taking into account the distance between gamma radiation source and detector. This is relevant when working on calibration under conditions of the facility that has protection from external gamma-radiation background, using point gamma-radiation sources. For working “source–detector” distances greater than 50 cm, it is possible to use calculations of the position of the effective detector energy release center for parallel uniform gamma radiation flux without taking into account the influence of the distance between the radiation

source and the detector. In this case, the relative error in determining the dose rate will not exceed 0.3 %.

Since the issue of taking into account the displacement of position of the effective energy release center when working at short distances using point gamma radiation sources has been resolved, it was decided to find functional dependences to determine the position of the effective center of energy release for calibration in conditions of low-background shield or at a facility with protection from external gamma radiation background when using sources with radionuclides ^{241}Am and ^{137}Cs . The choice of these sources is justified by their application during calibration and verification of measuring instruments, including in accordance with the verification scheme for facilities with protection against external gamma radiation background. The range from 10 to 100 cm was chosen as the working distance “source–detector” based on practical considerations.

Table 4 presents the calculated functional dependences of the position of the effective energy release center for two types of NaI(Tl) detector sizes $\text{Ø}40 \times 40$ mm and $\text{Ø}25 \times 40$ mm as a function of the distance from the point source of radiation to the detector.

Table 4

Functional dependences of the position of the effective energy release center depending on the distance to the point radiation source in the range of operating distances from 10 to 100 cm

Type of detector size	Gamma radiation source	Geometry of detector irradiation	Function $f(x)$, mm
$\text{Ø}25 \times 40$ mm	^{241}Am	End	$8.387 \times 10^{-5} \cdot x - 6.056 \times 10^{-8} \cdot x^2 + 0.277$
		Side	$1.409 \times 10^{-3} \cdot x - 9.086 \times 10^{-7} \cdot x^2 + 2.202$
	^{137}Cs	End	$6.819 \times 10^{-3} \cdot x - 4.301 \times 10^{-6} \cdot x^2 + 13.074$
		Side	$2.718 \times 10^{-3} \cdot x - 1.734 \times 10^{-6} \cdot x^2 + 10.209$
$\text{Ø}40 \times 40$ mm	^{241}Am	End	$9.527 \times 10^{-5} \cdot x - 7.084 \times 10^{-8} \cdot x^2 + 0.295$
		Side	$3.377 \times 10^{-3} \cdot x - 2.15 \times 10^{-6} \cdot x^2 + 2.932$
	^{137}Cs	End	$6.706 \times 10^{-3} \cdot x - 4.249 \times 10^{-6} \cdot x^2 + 13.461$
		Side	$6.745 \times 10^{-3} \cdot x - 4.334 \times 10^{-6} \cdot x^2 + 14.542$

The above functional dependences allow us to calculate the distance of the detector surface to the effective center, taking into account the detector's packing and reflector. Detectors with MgO reflectors with a density of 0.6 g/cm^2 and aluminum packaging with a thickness of 1.5 mm were used in the calculations. For detectors within detector units, the distance from the surface of the detector unit to the surface of the detector must also be taken into account.

Conclusion

An original method of determining the position of the effective energy release center of scintillation detector when irradiated by a point source of radiation on the side and end surface of the crystal using Monte Carlo methods is proposed. Calculations are made and functional dependences of the position of the effective energy release center of the NaI(Tl) scintillation detector of “popular” sizes are obtained.

The study confirmed that for inorganic scintillation detectors of medium sizes (e. g., $\text{Ø}25 \times 40$ mm or $\text{Ø}40 \times 40$ mm) the point source of gamma radiation, located at a distance of 1 m or more, produces a radiation field, which does not differ in characteristics from the field of radiation produced by parallel flux of gamma radiation.

It is shown that approaching the point source of gamma radiation to the surface of inorganic scintillation detector leads to displacement of the effective energy release center to the surface of the detector. This is most likely due to large photon dispersion due to close location of the point gamma radiation source to the detector surface, as a result most of the photons after one or more interactions leave the detector working volume, and it is also related to the dose profile according to the inverse law of distance squares.

Based on the calculated data obtained, the functional dependences of the position of the effective energy release center of NaI(Tl) crystal-based detector units on the distance to the point gamma radiation sources and the energy of gamma radiation sources for calibration problems in conditions of small “source–detector” distances were constructed. For example, under conditions of calibrating the dosimeter on a low-background shield or on a facility with protection from external gamma radiation background.

The results of the study will also be relevant for detectors of larger sizes, for example, $\text{Ø}63 \times 63$ mm or larger. For such cases, the displacement of the position of the detector’s effective energy release center relative to the parallel gamma radiation flux will be larger than for the detectors given in the article. Accordingly, the relative error in determining the dose rate from point sources at small source–detector distances for such detectors will depend on the linear dimensions of the detector.

The obtained data and functional dependences of the position of the effective energy release center of scintillation detectors are planned to be used on the facility with protection against external gamma radiation background for calibration and verification of dosimetric measuring instruments at the “ATOMTEX” enterprise.

References

1. IEC 61017:2016. Radiation protection instrumentation – Transportable, mobile or installed equipment to measure photon radiation for environmental monitoring. – Introd. 10.02.16. Geneva: Intern. Electrotechnical Commiss, 2016, p. 86.
2. IEC 60846–1:2009. Radiation protection instrumentation – Ambient and/or directional dose equivalent (rate) meters and/or monitors for beta, X and gamma radiation – Part 1: Portable workplace and environmental meters and monitors. – Introd. 16.04.09. Geneva: Intern. Electrotechnical Commiss, 2009, p. 116.
3. IEC 62533:2010. Radiation protection instrumentation – Highly sensitive hand–held instruments for photon detection of radioactive material. – Introd. 21.06.10. Geneva: Intern. Electrotechnical Commiss, 2010, p. 26.
4. Dombrowski H., Neumaier S. Traceability of the PTB low-dose rate photon calibration facility. *Radiation Protection Dosimetry*, 2010, no. 140, pp. 223–233.
DOI: 10.1093/rpd/ncq120
5. Lukashovich R., Verhusha Y., Guzov V. Kozevmyakin V. Application scintillation comparators for calibration low intense gamma radiation fields by dose rate in the range of 0.03–0.1 $\mu\text{Sv/h}$. *Springer Proceedings Phys.*, vol. 227, pp. 221–235.
DOI: 10.1007/978-3-030-21970-3_16
6. Lukashovich R. Calculation of effective center of gamma-radiation scintillation detector and its consideration at dosimetric control of radiation packages. Proceedings of the 11th International Scientific Conference “Sakharov Readings 2011: Ecological Problems of the XXI Century”, Minsk, 2011, pp. 201–204.
7. ISO 4037–3:2019. Radiological protection – X and gamma reference radiation for calibrating dosimeters and doserate meters and for determining their response as a function of photon energy. – Part 3: Calibration of area and personal dosimeters and the measurement of their response as a function of energy and angle of incidence. – Introd. 30.01.19. International Organization for Standardization, 2019, p. 76.
8. Ivanov V. Dosimetry of ionizing radiation. Moscow, Atomizdat Publ., 1964.
9. Mariuchi S. A new method of dose evaluation by spectrum dose conversion operator and determination of the operator”, JAERI 1209, 1971.
10. Fokov G., Kozhemyakin V. On the calibration of the Cherenkov detector of galactic and solar cosmic protons with energies from 600 MeV. *ANRI Publ.*, 2021, no. 1 (104), pp. 53–62.

ПРАВИЛА ОФОРМЛЕНИЯ СТАТЕЙ

Статьи, направленные в редакцию журнала, должны удовлетворять требованиям «Инструкции о порядке оформления квалификационной научной работы (диссертации)...», утвержденной Постановлением ВАК РФ от 28.02.2014 г. № 3

1. Материал статьи должен соответствовать профилю журнала и излагаться предельно ясно.

2. Статья представляется на русском или английском языке и публикуется на языке представления.

3. Поступившие в редакцию статьи проходят двойное полуслепое рецензирование. Основные критерии целесообразности опубликования – актуальность тематики, информативность, научная новизна.

4. Статья представляется в распечатанном и в электронном виде в формате текстового редактора Word for Windows, набор – сплошным текстом (без деления на колонки). Объём статьи не должен превышать 14 страниц, включая текст (шрифт Times New Roman, размер 12 п., интервал 1,5), таблицы, графический материал, всю необходимую информацию на английском языке.

5. На первой странице статьи указываются: индекс УДК, название статьи, фамилии авторов (фамилия автора, с которым следует вести переписку, отмечается звёздочкой и указывается его адрес электронной почты), названия и почтовые адреса организаций (улица, номер дома, индекс, город, страна), в которых работают авторы, на русском и английском языках. Статья включает: аннотацию (в пределах 200–250 слов); ключевые слова (не более 5); введение, в котором делается краткий обзор сделанного в мире и конкретно формулируется цель работы; основную часть; заключение, в котором в сжатом виде сформулированы основные полученные результаты с указанием их новизны, преимуществ и возможностей применения; список использованных источников. Аннотация, ключевые слова, список использованных источников представляются на русском и английском языках.

6. Аннотация должна быть информативной (содержать «выжимку» из всех разделов статьи – введения с указанием цели работы, методики, основной части и заключения).

7. Графический материал должен быть контрастным и чётким. Необходимо придерживаться единообразия техники исполнения однотипных иллюстраций. Рисунок должен располагаться после абзаца, содержащего ссылку на него. Не допускается размещение рисунков в конце подраздела и статьи. Изобразительный материал вставляется в текст статьи, а также даётся в виде отдельных файлов (**формат tif, jpg, разрешение не менее 300 dpi**). Текст на рисунках набирается основной гарнитурой; размер кегля соизмерим с размером рисунка (желательно 8 пунктов). Все рисунки нумеруются и сопровождаются подрисуночными подписями. Фрагменты рисунка обозначаются

строчными курсивными латинскими буквами – «a», «b» и т. д. Надписи на рисунках и подписи к рисункам даются на русском и английском языках. Все сокращения и обозначения должны быть расшифрованы в подрисуночной подписи. Рисунки желательно предоставлять в цвете. На рисунках должны быть указаны оси с обозначением приводимых величин и масштабов. На графиках не нужно давать координатную сетку, если это не осциллограмма. Во всех случаях на рисунках должен быть приведён масштаб.

8. У графиков, имеющих числовые значения по осям, рамки должны быть открыты, а засечки направлены внутрь рамки. На рисунках, представляющих собой графики зависимостей, не следует делать размерную сетку, следует дать лишь засечки на осях, причем все засечки должны быть оцифрованы. Если оси на рисунках оцифрованы, то они завершаются на позиции очередной засечки, где засечка не ставится, а вместо числовых значений даются обозначения переменной и единица измерения. Если оси не оцифровываются, то они завершаются стрелками, рядом с которыми даются обозначения переменных без единиц измерения.

9. Полутонные фотографии приборов или их частей представляются при публикации в тех случаях, когда они несут существенную информацию, которую нельзя выразить иным способом. Фотографии должны быть высококачественными, контрастными, с хорошо различимыми деталями.

10. Иллюстрации (графики, диаграммы, схемы, чертежи), рисованные средствами MS Office, должны быть контрастными и чёткими. Недопустимо нанесение средствами MS Word каких-либо элементов поверх вставленного в файл рукописи рисунка (стрелки, подписи) ввиду большого риска их потери на этапах редактирования и вёрстки. Иллюстрации должны иметь размеры, соответствующие их информативности: 8–8,5 см (на одну колонку), 17–17,5 см (на две колонки) или 23 см (во весь лист). Поэтому желательно изображать отдельные элементы и надписи на рисунке так, чтобы при уменьшении масштаба рисунка до одного из указанных размеров буквы и цифры приобрели высоту 2–2,5 мм, элементы схем 3–5 мм, отдельные точки 1 мм, а линии должны быть при этом разнесены на расстояние не менее 0,5–1 мм.

11. Надписи и обозначения на иллюстрациях следует располагать так, чтобы они не соприкасались ни с какими её частями. На задний план иллюстрации желательно не добавлять серый (цветной) фон или сетки.

12. Таблицы не должны дублировать графики. Каждая таблица имеет заголовок. На все таблицы

ПРАВИЛА ОФОРМЛЕНИЯ СТАТЕЙ

и рисунки следует давать ссылки в тексте. Таблицы не должны содержать вертикальные линии, делящие таблицу на столбцы. Название и содержание таблиц представляется на русском и английском языках.

13. Обозначения и сокращения, принятые в статье, расшифровываются непосредственно в тексте.

14. Размерность всех величин, принятых в статье, должна соответствовать Международной системе единиц измерений (СИ).

15. Набор формул должен проводиться в редакторе MathType целиком. Набор формул из составных элементов не допускается, номера формул – по правому краю. Нумеруются лишь формулы, на которые есть ссылки в тексте.

16. Необходимо использовать следующие установки редактора формул. Размеры: полный – 10 пт, подстрочный – 9 пт, под-подстрочный – 7 пт, символ – 14,5 пт, подсимвол – 12,5 пт. Стили: текст, функция, число, кириллица – шрифт «Times New Roman», вектор-матрица – шрифт «Times New Roman», жирный; греческий малый, греческий большой, символ – шрифт «Symbol», прямой; переменная – шрифт «Times New Roman», курсив.

17. Отдельные строчные буквы и специальные символы набираются в тексте гарнитурой Symbol **без использования редактора формул**. При наборе формул и буквенных обозначений необходимо учитывать следующие правила: **русский алфавит не используется**; греческие буквы, математические символы (grad , div , \ln , min , max и др.), единицы измерения (Вт, Дж, В, кг и др.), кириллические буквы, сокращения от русских слов (q_{cp}); обозначения химических элементов и соединений (в т. ч. в индексе) набираются **прямо**; латинские буквы – переменные и символы физических величин (в т. ч. в индексе) набираются **курсивом**; векторы – жирным шрифтом (стрелки вверх не ставятся).

18. Начертание обозначений в формулах и в основном тексте должно быть полностью идентично. В расшифровке формул, которая начинается словом

«где», символы и их порядок должны соответствовать символам и их порядку следования в формулах.

19. Список использованных источников составляется в порядке упоминания ссылок по тексту, должен содержать полные библиографические данные и приводится в конце статьи. Не рекомендуется давать ссылки на материалы конференций, статьи из электронных журналов без идентификатора DOI, учебные пособия, интернет-ресурсы. Ссылки на неопубликованные работы не допускаются. Желательно, чтобы количество ссылок было не менее 10; самоцитирование – не более 20 %.

20. Авторы на отдельной странице предоставляют о себе следующие сведения: фамилия, имя, отчество, ученая степень и звание, место работы и занимаемая должность, адрес электронной связи.

21. Статьи, излагающие результаты исследований, выполненных в учреждениях, должны иметь соответствующее разрешение на опубликование в открытой печати.

22. При необходимости в конце основного текста указываются наименование фонда, оказавшего финансовую поддержку, или уровень и наименование программы, в рамках которой выполнена работа, на русском и английском языках.

23. Авторы несут ответственность за направление в редакцию статей, ранее уже опубликованных или принятых к печати другими изданиями.

24. Статьи, не соответствующие перечисленным требованиям, к рассмотрению не принимаются и возвращаются авторам. Датой поступления считается день получения редакцией первоначального варианта текста.

25. Редакция предоставляет возможность первоочередного опубликования статей лицам, осуществляющим послевузовское обучение (аспирантура, докторантура, соискательство), в год завершения обучения; не взимает плату с авторов за опубликование научных статей; оставляет за собой право производить редакторские правки, не искажающие основное содержание статьи.

AUTHOR GUIDELINES

1. Article materials should correspond to the journal profile and be clearly written.
 2. An article should be submitted in Russian or English and will be published in its original language.
 3. Articles received by the Editorial Board will be reviewed by 2 specialists. The main criteria of acceptance are theme actuality, information value, and scientific novelty.
 4. All materials should be submitted in two hard copies together with electronic file in the Word for Windows format (97/2000/2003). The paper should not exceed 14 pages of the typewritten text (Times New Roman, 12 points, 1.5-space).
 5. The article should contain UDC number, Title (printed in capitals), Authors' names (the corresponding author name should be marked with asterisk), full Address of organization(s) in which the author(s) work, Abstract (200–250 words), Keywords (not more than 5 words), Introduction, the Text of the paper with tables, diagrams and figures (if there are any), Conclusion with clearly stated inferences, List of References, List of Symbols and Abbreviations (if it is necessary). Title, Authors' names and affiliation(s), Abstract, Keywords should be presented both in English and Russian languages.
 6. The abstract should be informative (contain "squeeze" from all sections of the article – the introduction stating the purpose of the work, methods, main part and conclusion).
 7. Figures should be black-and-white, represented in graphical formats tif, attached with Excel or MS Graph and added with captions. All symbols in figures should be described.
 8. Tables should be placed directly in the article body. Diagrams and tables should not contain the same information. Each table should have the title. All tables, diagrams and figures should be referenced in the text.
 9. Symbols and abbreviations which are used in articles should be deciphered directly in the text and also (if necessary) taken out on a separate page.
 10. Dimensions of all quantities used in the article should correspond to International System of Units.
 11. Formulas should be typed in MathType.
 12. List of References is to be placed at the end of the article with full bibliographic information. Order of references should correspond to the order of their occurrence in the text. It is not recommended to refer to conference proceedings, papers from electronic journals without DOI number, textbooks, internet resources. References on unpublished works are prohibited. It is recommended to refer to not less than 10 references, self-citations – not more than 20 %.
 13. The following information about every co-author should be presented: family name, first name, patronymic (or second) name (if there are any), scientific degree and title, organization and position, full address with the postal code for correspondence, office or mobile phone numbers, fax, e-mail.
 14. Articles containing investigation results obtained in organizations should have a corresponding permission for publication.
 15. Names of Foundations or Programs financially granted the research may be acknowledged in the end of the text.
 16. Authors are responsible for submitting articles previously published or accepted by other publisher.
 17. Articles not meeting the requirements of the Editorial Board would not be accepted and may be returned to the authors. The date of receipt is considered to be the day when the Editorial Board receives the author's original paper.
 18. Authors conducting postgraduate (graduate studies, doctoral studies) have a priority in publishing their articles out of queue in the year of completion. Authors do not pay for publishing scientific articles. The Editorial Board can shorten and/or change the text if it does not strain the meaning of the article.
-

Индексы:
74835; 748352